Structure, physical properties, and applications of $SrRuO_3$ thin films

Gertjan Koster*

Faculty of Science and Technology and MESA+ Institute for Nanotechnology, University of Twente, 7500 AE Enschede, The Netherlands

Lior Klein

Department of Physics, Nano-magnetism Research Center, Institute of Nanotechnology and Advanced Materials, Bar-Ilan University, Ramat-Gan 52900, Israel

Wolter Siemons

Materials Science and Technology Division, Oak Ridge National Laboratory, Oak Ridge, Tennessee 37831, USA

Guus Rijnders

Faculty of Science and Technology and MESA+ Institute for Nanotechnology, University of Twente, 7500 AE Enschede, The Netherlands

J. Steven Dodge

Department of Physics, Simon Fraser University, Burnaby, British Columbia, V5A 1S6, Canada

Chang-Beom Eom

Department of Materials Science and Engineering, University of Wisconsin–Madison, Madison, Wisconsin 53706, USA

Dave H. A. Blank

Faculty of Science and Technology and MESA+ Institute for Nanotechnology, University of Twente, 7500 AE Enschede, The Netherlands

Malcolm R. Beasley

Department of Applied Physics and the Geballe Laboratory for Advanced Materials, Stanford University, Stanford, California 94305, USA

(published 8 March 2012)

$SrRuO_3$ is endowed with three remarkable features. First, it is a moderately correlated material that exhibits several novel physical properties; second, it permits the epitaxial growth of essentially single-crystal films; and third, because it is a good conductor, it has attracted interest as a conducting layer in epitaxial heterostructures with a variety of functional oxides. In this review, the present state of knowledge of $SrRuO_3$ thin films is summarized. Their role as a model system for studying magnetism and electron transport characterized by intermediate electron correlation and large magnetocrystalline anisotropy is demonstrated. The materials science of $SrRuO_3$ thin film growth is reviewed, and its relationship to electronic, magnetic, and other physical properties is discussed. Finally, it is argued that, despite all that has been learned, a comprehensive understanding of $SrRuO_3$ is still lacking and challenges remain.American Physical Society

DOI: 10.1103/RevModPhys.84.253 PACS numbers: 73.50.−h, 75.70.−i, 71.20.−b, 78.20.−e

CONTENTS

*g.koster@utwente.nl

I. INTRODUCTION

The complex oxide perovskite $SrRuO_3$ has fascinated researchers for over 40 years. The first property to draw attention was its surprising itinerant ferromagnetism (Randall and Ward, 1959). More recently, interest in $SrRuO_3$ has broadened to include its unusual transport properties and the degree and consequences of correlation. For example, while at low temperatures $SrRuO_3$ is a Fermi liquid (Mackenzie *et al.*, 1998), at high temperatures it exhibits bad metal behavior (Klein, Dodge, Ahn, Snyder *et al.*, 1996). In addition, while $SrRuO_3$ shares many properties with other complex oxides (including the cuprates), it has the appealing feature that the phenomena of interest are present in the undoped parent material, thereby avoiding the complications of disorder. The minimal effect of disorder in $SrRuO_3$ gives it a unique position in the study of these phenomena.

$SrRuO_3$ is a member of a larger class of interesting ruthenates. It is the infinite-layer material ($n = \infty$) in the well-known series of ruthenates $Sr_{n+1}Ru_nO_{3n+1}$. Another significant member of this series is Sr_2RuO_4, a novel superconductor for which there is strong evidence of broken time-reversal symmetry (Luke *et al.*, 1998; Mackenzie and Maeno, 2003; Xia, Maeno *et al.*, 2006). Alloys of $SrRuO_3$ in which Ca is substituted for Sr have also drawn great interest, in part because $CaRuO_3$ is only a paramagnet, despite being isoelectronic to $SrRuO_3$. In addition, at low temperatures, the resistivity of $CaRuO_3$ exhibits non-Fermi-liquid behavior (Klein *et al.*, 1999; Capogna *et al.*, 2002).

$SrRuO_3$ is also remarkable beyond its physical properties. Typically, bulk single crystals are presumed to be the most important form of a material for physical study. However, in the case of $SrRuO_3$, thin films have played that role. Building on the initial demonstration of epitaxial single-crystal films (Eom *et al.*, 1992), the processes for depositing thin films of this material have been extended and refined to such a degree that epitaxial thin films of $SrRuO_3$ on appropriate substrates have become the model system of choice for the study of its physical properties. In addition, they have permitted extensive materials science studies of structure-property relationships in $SrRuO_3$. Indeed, the research on the physical properties and materials science of $SrRuO_3$ thin films has exhibited a remarkable symbiosis. Consequently, in this review we give comparable weight to both aspects.

In addition, thin films of $SrRuO_3$ have drawn wide applied interest as a conducting layer in epitaxial multilayered structures of complex oxides, in particular, as electrodes in oxide electronics. In addition, the compound's resistance to many chemical solutions (up to temperatures as high as 1200 K) has proved beneficial in device processing.

Reflecting this broad interest, some 1000 papers spanning the physics, materials science, and applications of $SrRuO_3$ have been published over the last two decades. And interest continues to grow. It seems timely, therefore, to review this progress and at the same time provide a foundation for further work.

Although our focus is on thin films of $SrRuO_3$, in Sec. II we summarize briefly the basic properties of bulk $SrRuO_3$ from the materials and physical points of view. After this summary, beginning in Sec. III, we turn to a detailed and systematic review of the synthesis, materials characterization, electronic structure, and physical properties of thin films of this material. By way of introduction, the content of these further sections is outlined below.

Thin film growth: As noted above, thin films of $SrRuO_3$ have been the most important form of this material for scientific study and applications. They have been grown by a wide variety of approaches, including (90° off-axis) sputter deposition, pulsed laser deposition (PLD), reactive thermal evaporation, reactive molecular beam epitaxy (MBE), and metal organic chemical vapor deposition (MOCVD). In all cases, the quality of the film growth depends on the use of epitaxy and vicinal substrates with singly terminated surfaces and on precise control of stoichiometry.

In order for $SrRuO_3$ to grow coherently on a single-crystal substrate, close lattice matching between the in-plane lattice parameter of the layer and that of a substrate is required. The residual lattice mismatch introduces strain that can affect the structural and electrical properties of the $SrRuO_3$ layer.

To demonstrate the importance of the choice of substrate, we compare the structure of $SrRuO_3$ thin films when grown on different substrate materials. Bulk $SrRuO_3$ is known to

have several structural phase transitions, and the temperatures at which these occur in thin films depend on the substrate material. We review these changes, in particular, for films grown on $SrTiO_3$. From the understanding obtained, a model of the well-known twinning in $SrRuO_3$ films can be constructed. We then turn to the impact of deposition conditions on the stoichiometry of $SrRuO_3$ films.

Thin films of $SrRuO_3$ also exhibit a wide range of epitaxial growth phenomena, such as nearly perfect step-flow growth at intermediate temperatures. This renders $SrRuO_3$ a model system for the study of nucleation and growth in complex oxide thin films, akin to the role that Si and GaAs have played in the past for covalent systems and Cu for metallic systems.

Physical properties: Here we review the many studies that have been carried out to determine the magnetic, transport, and electronic properties of thin film $SrRuO_3$. It is paramagnetic at room temperature and ferromagnetic below the Curie temperature of about 150 K. In both phases, thin films of these materials exhibit a strong magnetocrystalline uniaxial anisotropy. The magnetic anisotropy leads to an Ising-like magnetic phase transition and stripe domain structure with narrow domain walls.

While the resistivity of $SrRuO_3$ shows a metallic temperature dependence ($d\rho/dT > 0$), its transport properties are far from being well understood. It exhibits so-called *bad metal* behavior at high temperatures and Fermi-liquid behavior at low temperatures. Near the ferromagnetic phase transition critical magnetic fluctuations seem to affect transport properties more strongly than expected. These results have drawn theoretical attention and led to the claim that this bad metal behavior is related to the orbital degeneracy present in $SrRuO_3$. Domain-wall-related transport phenomena have also drawn considerable attention due to the large interface resistance of the narrow walls and the efficient current-induced domain-wall motion. These observations highlight the relevance of $SrRuO_3$ to spintronics.

The optical conductivity of $SrRuO_3$ can be divided crudely into two ranges: $\hbar\omega \geq 1$ eV, where the optical properties are fairly well understood, and $\hbar\omega < 1$ eV, where they are not. The large spin-orbit coupling of the ruthenium ion also produces large magneto-optical effects that connect the optical, magnetic, and magnetotransport properties. The higher-frequency range is dominated by interband transitions that can be described quantitatively by density functional theory (DFT). However, at lower frequencies, the optical spectral weight grows with decreasing temperature to form a peak that shows an unusual non-Drude power-law dependence on frequency. Both the spectral weight shift and the frequency dependence have attracted theoretical interest because they suggest physics beyond the standard model for metallic conduction.

Other important questions in the physics of $SrRuO_3$ are its degree of electron correlation and how correlation affects its physical properties. Comparison of the electronic structure of $SrRuO_3$, as determined by photoemission studies, across a whole series of ruthenium oxides reveals that the degree of correlation is substantial, which naturally leads to the question of what factors control the degree of correlation.

The section concludes with a review of systematic investigations into the influence of strain, stoichiometry, and film thickness on the physical properties of $SrRuO_3$. For example, we shall see that the electronic structure is surprisingly sensitive to the Ru stoichiometry and that in very thin films (of the order of a few monolayers) the magnetism behaves differently.

Applications of thin film $SrRuO_3$: By far, the most dominant use of $SrRuO_3$ is as an electrode material. There are several reasons. It is one of the few complex oxides that is metallic without doping. It has a good lattice match with a wide variety of functional oxides and therefore is relatively easy to incorporate in heterostructures. And it has high chemical stability. In this section, we present an overview of these useful properties, along with a short discussion of the use of $SrRuO_3$ in magnetic tunnel junctions.

Major issues: In the final section of this review, we present a summary of the understanding of $SrRuO_3$, clarifying those aspects that are understood and those that are not.

II. BULK PROPERTIES

$SrRuO_3$ is the infinite-layer material ($n = \infty$) in the well-known series of ruthenates $Sr_{n+1}Ru_nO_{3n+1}$. As with many ABO_3 perovskite compounds, $SrRuO_3$ exhibits orthorhombic symmetry at room temperature, as depicted in Fig. 1. An orthorhombic cell is typically observed in ABO_3 perovskites when the A-O bond length is less than 2 times the B-O length, which results in rotations of the BO_6 octahedra. In $SrRuO_3$, the RuO_6 octahedral rotation produces a distorted, pseudocubic perovskite structure, isostructural with $GdFeO_3$, with lattice parameters $a = 5.5670$ Å, $b = 5.5304$ Å, and $c = 7.8446$ Å (Jones *et al.*, 1989); the pseudocubic lattice constant is $a = 3.93$ Å. The orthorhombic phase can be visualized by rotation of BO_6 (RuO_6) octahedra counterclockwise about the $[010]_{cubic}$ and $[001]_{cubic}$ directions and clockwise rotation about the $[100]_{cubic}$ direction of an ABO_3 cubic perovskite (pseudocubic with $a_{pc} = 3.93$ Å); these directions become inequivalent upon rotation.

With increasing temperature, the degree of the orthorhombic distortion decreases, and the structure transforms to

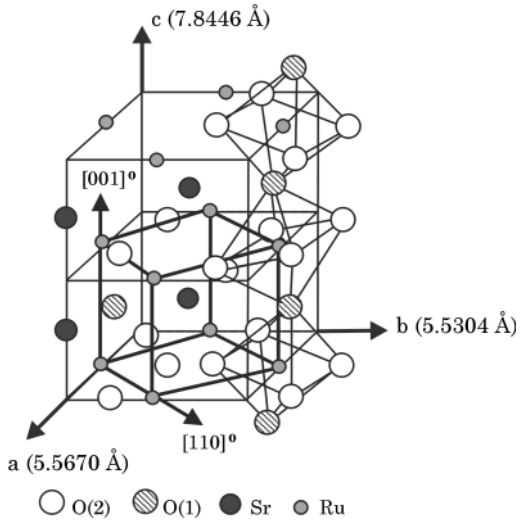

FIG. 1. Schematic view of the orthorhombic unit cell of $SrRuO_3$. From Gan *et al.*, 1999.

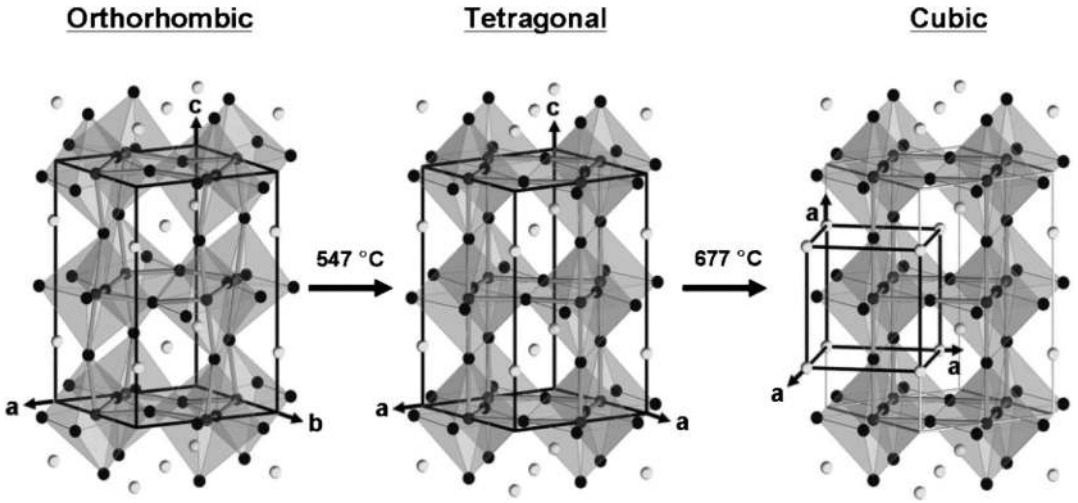

FIG. 2. A sequence of phase transitions of unstrained bulk $SrRuO_3$ from orthorhombic to tetragonal and then cubic symmetry at 547 °C and 677 °C, respectively. The unit cell of the orthorhombic $SrRuO_3$ consists of four formula units of the ideal cubic perovskite structure. The atoms of Ru occupy high-symmetry positions with respect to the orthorhombic shape of the cell. The atoms of O and Sr are displaced from their high-symmetry positions due to the octahedral tilting. The tetragonal $SrRuO_3$ is a one-tilt system, where RuO_6 octahedra are rotated only about the [001] direction. The cube corresponds to the unit cell of each $SrRuO_3$ form. Gray, black, and white balls represent Ru, O, and Sr atoms, respectively. From Choi *et al.*, 2010.

higher-symmetry perovskite structures. Around 550 °C, the orthorhombic structure transforms into a tetragonal structure with space group $I4/mcm$ (Kennedy and Hunter, 1998). In this tetragonal unit cell, the RuO_6 octahedra are rotated only about the $[001]_{cubic}$ $SrRuO_3$ direction. Going to higher temperatures around 680 °C, tetragonal $SrRuO_3$ transforms into a cubic structure with a standard perovskite space group $Pm3m$, where the RuO_6 octahedra are not rotated (Kennedy and Hunter, 1998), as illustrated in Fig. 2. As described later, these structural transition temperatures are influenced by strain, and, hence, in the case of epitaxial thin films, they depend on the substrate material.

Lattice parameters at low temperatures have been measured using neutron diffraction by Bushmeleva *et al.* (2006) and using x-ray diffraction by Kiyama *et al.* (1996) and Leitus, Reich, and Frolow (1999). Both groups report a nearly constant unit-cell volume below T_C; see Fig. 3. They conclude that the effect of the normal thermal expansion and the reduction of magnetic moment compensate each other, as in 3*d*-Invar alloys (Rancourt and Dang, 1996).

Insight into the basic electronic structure of $SrRuO_3$ can be obtained by developing its energy level structure from atomic

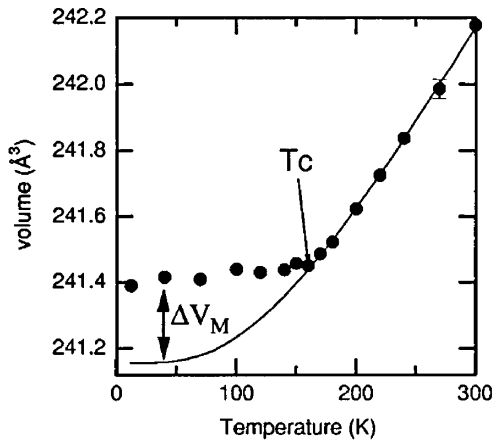

FIG. 3. Temperature dependence of the unit-cell volume of $SrRuO_3$. The solid line represents the contribution of the phonons fitted by the Debye function with Θ of 525.5 K, $V(T = 0\ \mathrm{K})$ of 240.9 Å^3, and $9\gamma Nk_B/B$ of 0.0281 Å^3/K. From Kiyama *et al.*, 1996.

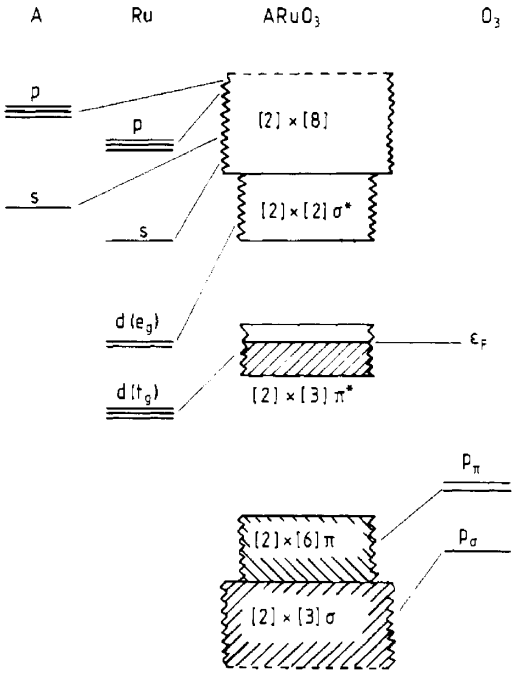

FIG. 4. Schematic low-spin one-electron energy level diagram for a perovskite ruthenate $ARuO_3$. The degeneracies of the bands indicated in square brackets are multiplied by 2 to allow for spin degeneracy. The correlation lines indicate the dominant atomic parentage of the band states. From Cox *et al.*, 1983.

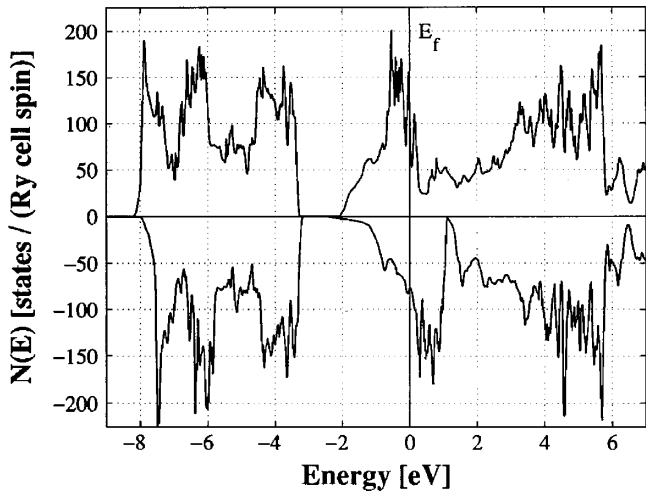

FIG. 5. Electronic density of states of ferromagnetic $SrRuO_3$. Majority spin is plotted upward, minority spin downward. The cell contains four formula units. From Allen *et al.*, 1996a.

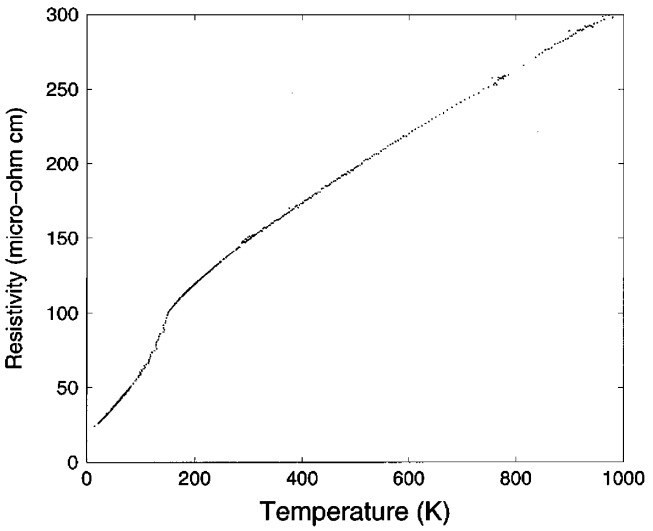

FIG. 7. Resistivity vs temperature for $SrRuO_3$. From Allen *et al.*, 1996a.

orbitals, as depicted schematically in Fig. 4. As the diagram shows, the fivefold degeneracy of the Ru($4d$) orbitals is broken into two groups by the octahedral crystal environment, raising the energy of the $4d(e_g)$ levels above the $4d(t_{2g})$ levels. When the three $4d(t_{2g})$ levels are filled with four electrons according to Hund's rules, the resulting spin state is $S = 1$. These simple arguments allow one to anticipate the band structure and set up the questions of itineracy and correlation.

Early first-principle band structure calculations for $SrRuO_3$ were published by Allen *et al.* (1996a), using the linear muffin-tin orbital method, and by Singh (1996b), who used the linearized augmented plane-wave method. Both calculations correctly predicted that $SrRuO_3$ is an itinerant ferromagnet and obtained a ground-state moment of $1.5\mu_B$–$1.6\mu_B$, close to the measured value. Figure 5 shows the spin-resolved density of states (DOS) from Allen *et al.* (1996a), which indicates a Stoner splitting of nearly 1 eV

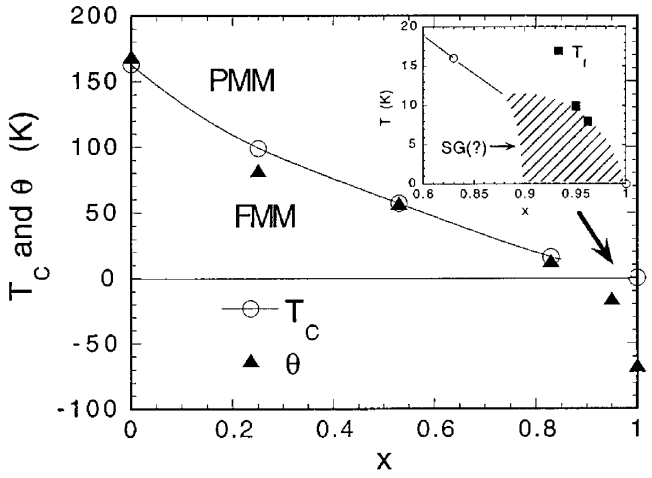

FIG. 6. Magnetic ordering temperature T_C and Curie-Weiss temperature vs Ca concentration x. The inset shows an expanded view of the presumed spin-glass-ordering regime (Vidya *et al.*, 2004). From Cao *et al.*, 1997.

between the majority and minority bands, together with a significant density of states for both at the Fermi level. As expected from the atomic picture described above, the states near the Fermi level have predominantly Ru $4d(t_{2g})$ and O $2p$ character.

Singh (1996b) noticed that the calculated ground-state moment for $SrRuO_3$ was $1.59\mu_B$ for the actual orthorhombic structure, but only $1.17\mu_B$ for the ideal cubic structure, suggesting that the crystal structure strongly influences the magnetic properties of $SrRuO_3$. Mazin and Singh (1997a) subsequently confirmed this by performing calculations of both $SrRuO_3$ and the isoelectronic $CaRuO_3$ for different crystal structures. They found that, while calculations correctly predict a nonmagnetic ground state for $CaRuO_3$, imposing the crystal structure of $SrRuO_3$ and repeating the calculation yields a ferromagnetic ground state with a moment of $1.68\mu_B$. These changes are associated with the strength of the perovskite distortion: The octahedral tilt angle in $CaRuO_3$ is about twice as large as in $SrRuO_3$, which results in a mixing between bands with e_g and t_{2g} character that reduces both the Stoner factor and the total bandwidth. Figure 6 shows the phase diagram of $Sr_{1-x}Ca_xRuO_3$ and illustrates how the ferromagnetism of $SrRuO_3$ evolves into paramagnetism in $CaRuO_3$.

Figure 7 shows the resistivity of $SrRuO_3$ as a function of temperature. The drop in resistivity at $T = 160$ K reflects the ferromagnetic transition. At higher temperatures the resistivity continues to rise beyond the Ioffe-Regel limit, which is the canonical signature of a bad metal (Emery and Kivelson, 1995; Allen *et al.*, 1996a). At low temperature, conventional metallic behavior is evident, and as discussed later, the material is a well-defined Fermi liquid; see Secs. IV.B.1.c and IV.C.1.

III. THIN FILM GROWTH

In this section, we review the three main deposition techniques used to produce thin films of $SrRuO_3$. We also review the common substrates used to grow these films, with a

special focus on $SrTiO_3$, the most commonly used substrate material for epitaxial growth of $SrRuO_3$. We look at the properties of films on the various substrates at room temperature and at elevated temperatures, where the unit cell undergoes transitions to phases of higher symmetry. The results lead naturally to the issue of twinning, which is determined by the first stage of growth and depends predominantly on the morphology and orientation of the substrate. To conclude this section, we discuss the chemistry of the films and clarify the influence of different deposition techniques on their stoichiometry.

A. Growth methods

Of the many reported approaches to thin film deposition of $SrRuO_3$, we highlight those that have been most successful in producing epitaxial films. These are (1) (90° off-axis) magnetron sputter deposition, (2) reactive electron beam coevaporation, and (3) pulsed laser deposition.

(1) The first thin films of $SrRuO_3$ were synthesized using 90° magnetron sputtering (Eom *et al.*, 1992). They used this approach based on their earlier success in depositing superconducting $YBa_2Cu_3O_{7-\delta}$ (YBCO) thin films using this method (Eom *et al.*, 1989). The sputtering atmosphere consisted of 60 mTorr Ar and 40 mTorr O_2. The radio-frequency power was 125 W and generated a self-bias of −140, −220, and −200 V, respectively, on the $SrRuO_3$, $CaRuO_3$, and $Sr_{0.5}Ca_{0.5}RuO_3$ sputter guns. The substrate block temperature was held at 680 °C. These sputtering parameters give a deposition rate of 0.2 Å s^{-1}. After deposition, the chamber was immediately vented to an O_2 pressure of 300 Torr, and the sample was then allowed to cool to room temperature.

(2) Another successful approach is reactive electron beam coevaporation, which was first reported by Ahn, Hammond *et al.* (1997). The strength of this approach is that it yields high-purity, single-crystalline thin films of $SrRuO_3$. Typically, the films are deposited in an ultrahigh vacuum using electron beam thermal evaporation of the cations, and atomic oxygen is provided using an electron cyclotron resonance source operating at a background pressure of 2×10^{-5} Torr. The individual cation deposition rates are monitored using atomic absorption, which allows the control of the cation stoichiometry to within 3%. The substrates are radiatively heated to 660 °C. Remarkably, samples grown using this method can exhibit residual resistivity ratios (RRRs) as high as 60, which historically made possible the observation of quantum oscillations in these films (Mackenzie *et al.*, 1998).

(3) By far the most widespread method for depositing thin films of complex oxides is PLD. $SrRuO_3$ is no exception, and its first successful synthesis in thin film form was reported by Wu *et al.* (1993) on $LaAlO_3$ and later by Chen *et al.* (1997) on $SrTiO_3$. Subsequently, PLD has been used by many groups, with correspondingly as many deposition conditions reported. The most commonly reported ranges of substrate temperatures, oxygen partial pressures, and laser fluency are 600–700 °C, up to several 100 mTorr of pure O_2 as well as various forms of activated oxygen (Gupta, Hussey, and Shaw, 1996) and 1–5 J cm^{-2} excimer laser power (KrF or XeCl), respectively. Also very importantly, with the development of high-pressure *in situ* reflection high-energy electron diffraction (RHEED) (Rijnders *et al.*, 1997), it has become possible to carefully study the nucleation and growth of these PLD $SrRuO_3$ films during the initial stages of film growth.

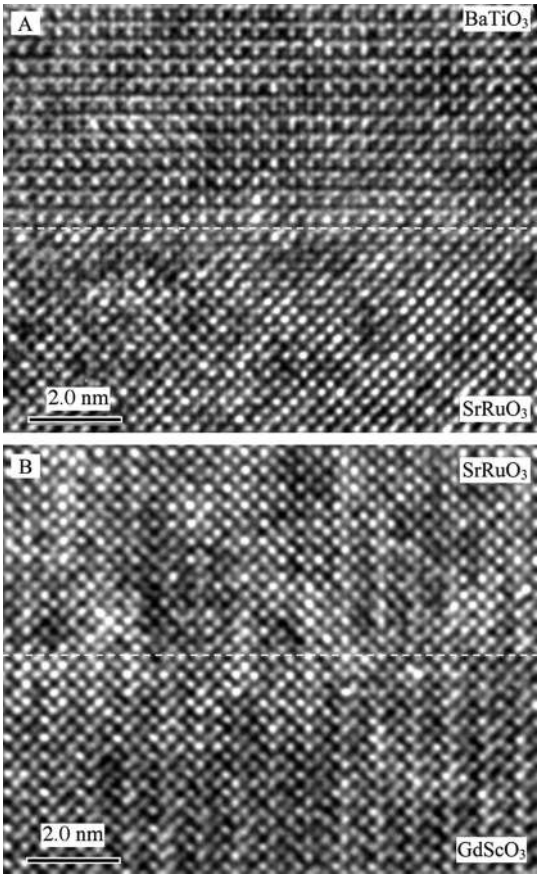

FIG. 8. High-resolution TEM images showing (a) the $BaTiO_3/SrRuO_3$ and (b) the $SrRuO_3/GdScO_3$ interfaces. Dashed lines mark the positions of the interfaces. From Choi *et al.*, 2004.

To illustrate the quality of the films possible using PLD, in Fig. 8, we show a transmission electron micrograph (TEM) cross-section image of a heterostructure formed by a $SrRuO_3$ film (used as an electrode) with a ferroelectric $BaTiO_3$ film. As the image shows, the coherent growth across the substrate-electrode and electrode-ferroelectric interfaces is outstanding.

Finally, other deposition methods have been reported [e.g., MOCVD (Okuda, Saito, and Funakubo, 2000; Funakubo *et al.*, 2002)] but these approaches are less commonly used and are not discussed in this review.

B. Growth on $SrTiO_3$

As already noted, the most common (and successful) substrate material used for the deposition of $SrRuO_3$ thin films is $SrTiO_3$. $SrTiO_3$ has a cubic perovskite unit cell with a lattice

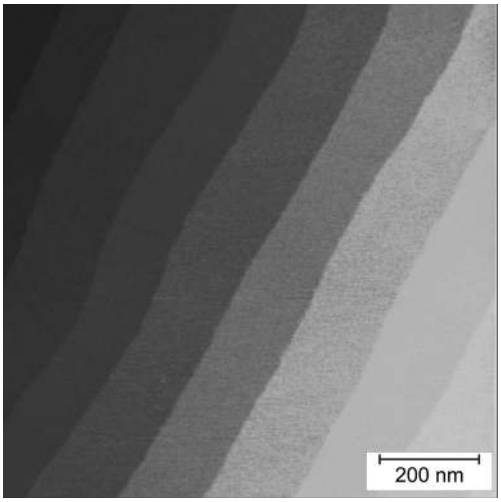

FIG. 9. A typical AFM scan of an HF-treated $SrTiO_3$ substrate. After chemical etching, the surface is TiO_2 terminated with steps edges of one unit-cell height.

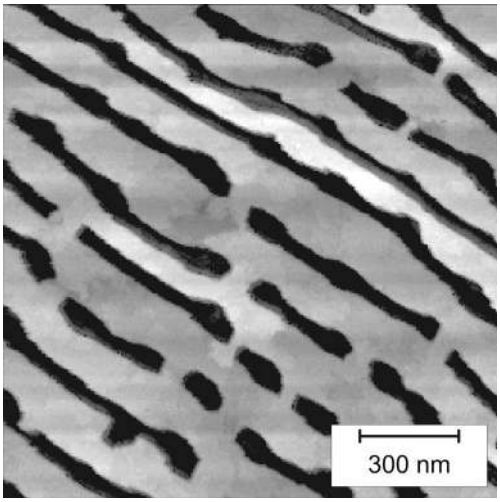

FIG. 10. A scanning tunneling microscopy scan of a 30-nm-thick $SrRuO_3$ film on $SrTiO_3$. Although the termination of the substrate was TiO_2, as shown in Fig. 9, before the sample was heated in the deposition system, Sr diffused to the surface and moved to the step edges. On the SrO-terminated areas, $SrRuO_3$ grew more slowly than on the TiO_2-terminated areas, resulting in the trenches clearly seen in the STM image. At the same time, on the flat areas, unit-cell high steps can still be observed.

parameter of 3.905 Å, which provides good lattice matching with many complex oxides. A clean and well-defined surface is important in good thin film growth of $SrRuO_3$. Typically the surface is cleaned using organic solvents (for example, acetone and ethanol) followed by annealing in oxygen at an elevated temperature. Also, the terminating layer of the substrate has a large influence on the initial growth of a deposited thin film (Choi *et al.*, 2001). In particular, having singly terminated surfaces (either SrO or TiO_2 in the case of $SrTiO_3$) has been found to be important. Fortunately, a method has been developed using an HF treatment to make the surface of $SrTiO_3$ singly terminated (Kawasaki *et al.*, 1994; Koster *et al.*, 1998). The method reliably yields a TiO_2-terminated surface with straight step edges, as illustrated in Fig. 9.

Whenever Sr diffuses to the surface, it results in double termination, which is not beneficial to the uniform growth of a $SrRuO_3$ film. $SrRuO_3$ appears to have a preference for one termination or the other and seems to grow faster on the *B*-site termination, which will become clearer in Sec. III.B. Such nonuniform growth results in many defects in the film, and for very thin films these defects can dominate the transport properties. An extreme example is given in Fig. 10 where $SrRuO_3$ has been grown on $SrTiO_3$ with some SrO at the steps. Large trenches have formed, which obviously will influence the macroscopic transport properties of the sample. In recent papers, this characteristic growth behavior of $SrRuO_3$ on mixed-termination substrates has been identified as a possible method to fabricate low-dimensional lateral structures (Bachelet *et al.*, 2009). It could also explain the growth morphologies observed earlier by Chae *et al.* (2000), Sanchez *et al.* (2003, 2004, 2005), Vasco *et al.* (2003, 2004, 2005), J. L. Li *et al.* (2005), Y. R. Li *et al.* (2005), and Sanchez, Herranz, Infante *et al.* (2006). Transport measurements on these samples show a strong dependence on such growth morphologies (Herranz *et al.*, 2003a, 2003b; Herranz, R. Sanchez *et al.*, 2004; Chopdekar, Takamura, and Suzuki, 2006).

Other kinetic effects present during growth of $SrRuO_3$ can lead to other dramatic morphological changes, compared to the two-dimensional surfaces. They have been summarized by Sanchez, Herranz, Ferrater *et al.* (2006) and Sanchez, Herranz, Fontcuberta *et al.* (2006) and more quantitatively by Hong *et al.* (2005).

Most of the work discussed here has been performed on films grown on $SrTiO_3$ substrates. However, numerous other substrate materials are available. In a recent report, a proper surface treatment for scandate substrates (e.g., $DyScO_3$) was found (Kleibeuker *et al.*, 2010). For other substrate materials, however, finding a suitable surface treatment to yield singly terminated surfaces remains a difficult task. Table I provides a summary of other substrate materials mentioned in this review, including the unit-cell parameters, the resulting $SrRuO_3$ strain, and other important physical properties. We now turn to a more detailed discussion of the growth of $SrRuO_3$ thin films.

1. Initial growth of $SrRuO_3$ thin films

The initial growth stage of $SrRuO_3$ thin films has been extensively studied by Choi *et al.* (2001) and Rijnders *et al.* (2004). Using high-pressure RHEED (Rijnders *et al.*, 1997) and atomic force microscopy (AFM), they studied the PLD growth of $SrRuO_3$ *in situ* on $SrTiO_3$ substrates with singly terminated TiO_2 surfaces. An AFM micrograph of a $SrRuO_3$ film grown in this way is shown in Fig. 11. In this particular case, the $SrRuO_3$ film was deposited on a TiO_2-terminated vicinal (0.2°) $SrTiO_3$ substrate. A clear step-terrace structure is evident. Also the surface morphology of the substrate can still be seen. The step heights, determined from AFM cross-section analysis, are approximately 4 Å.

The intensity of the specular RHEED spot (20 keV, ~1° incidence angle, 10° azimuthal angle) as recorded during growth of $SrRuO_3$ at different growth temperatures is shown in Fig. 12(a). Visibly, the initial growth, i.e., deposition of the

TABLE I. A selection of frequently used oxide substrate materials and their structural and transport properties. $SrRuO_3$ strain is defined as $(d_l - d_s)/d_l$, where d_l and d_s refer to the bulk in-plane lattice parameters of the $SrRuO_3$ layer and the substrate, respectively.

Substrate	Symmetry at 300 K	a (Å)	b (Å)	c (Å)	$SrRuO_3$ strain (%)	Transport properties
$DyScO_3$	Orthorhombic	5.44	5.71	7.89	−0.574	Insulating
$SrTiO_3$	Cubic	3.905			0.446	Insulating
Nb doped $SrTiO_3$	Cubic	3.905			0.446	Conducting
$NdGaO_3$	Orthorhombic	5.43	5.50	7.71	1.72	Insulating
$LaAlO_3$	Cubic	3.82			2.61	Insulating
Bulk $SrRuO_3$	Orthorhombic	5.567	5.530	7.845		Conducting

first unit-cell layer, is characterized by nucleation and growth of two-dimensional (2D) islands (with a persisting height of one unit cell) as shown by the cusplike intensity variations.

They noted that the first period of the RHEED oscillations was always longest at 700 °C. Moreover, the first RHEED minimum occurred after deposition of the material needed for approximately 1.5 unit-cell layers [seen as 2D islands in Fig. 13(a)], whereas the first RHEED maximum occurs after two unit-cell layers of material. After two unit-cell layers, a closed layer of $SrRuO_3$ with SrO termination was observed [see Fig. 13(b)]. When a SrO-terminated substrate was used as the starting surface, similar oscillations occurred with the notable difference that the first oscillation period was identical to the subsequent periods, as can be seen in Fig. 12(b). After completion of this $SrRuO_3$ unit-cell layer, subsequent stoichiometric deposition leads to unit-cell layer-by-layer growth, indicated by the equidistant RHEED intensity oscillations after the first maximum; see Fig. 12.

From the above observations, Rijnders and co-workers (Choi *et al.*, 2001; Rijnders *et al.*, 2004) concluded that a switch in the termination occurred from *B* site (TiO_2-terminated $SrTiO_3$) to *A* site (SrO-terminated $SrRuO_3$) during deposition of the first unit-cell layers. Preserving perovskite stacking, they expected a RuO_2 termination after stoichiometric deposition of the first unit-cell layer, accompanied with a maximum in the RHEED intensity. Since this maximum was not observed, they reasoned that RuO_2 termination is not stable at these deposition conditions.

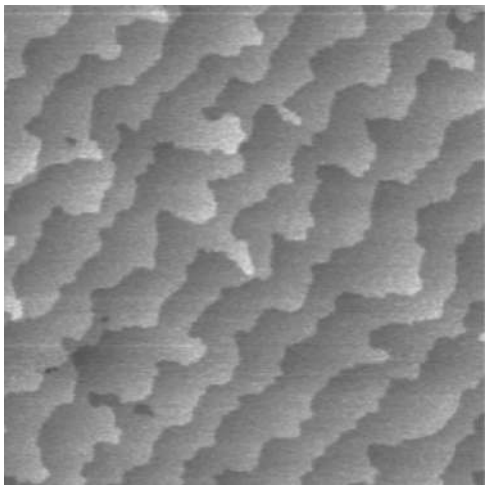

FIG. 11. Typical AFM micrograph (1×1 μm^2) of a 50-nm-thick $SrRuO_3$ film.

Apparently, during the deposition of the first unit-cell layer, $SrRuO_3$ decomposed into SrO and the highly volatile Ru_xO_y (Bell and Tagami, 1963; Nakahara *et al.*, 2001). As a result, the latter evaporated from the surface, leaving SrO as the terminating surface layer. This decomposition stopped after the terminating layer was completely switched from TiO_2 to SrO.

After deposition of approximately four unit-cell layers, the intensity oscillations damped and the average RHEED intensity remained constant during subsequent deposition. The absence of oscillations at this later stage of growth could be interpreted either as increased roughness due to three-dimensional (3D) growth or as a step-flow growth that resulted in very smooth surfaces. Because of the high RHEED intensity and the observation of a smooth surface by AFM (see Fig. 11), the latter possibility is most likely. In this regime, only intensity variations due to the pulsed nature of the deposition were visible. This feature of the RHEED intensity apparently showed a transition from growth by the formation and coalescence of two-dimensional islands to growth by step advancement (Choi *et al.*, 2001).

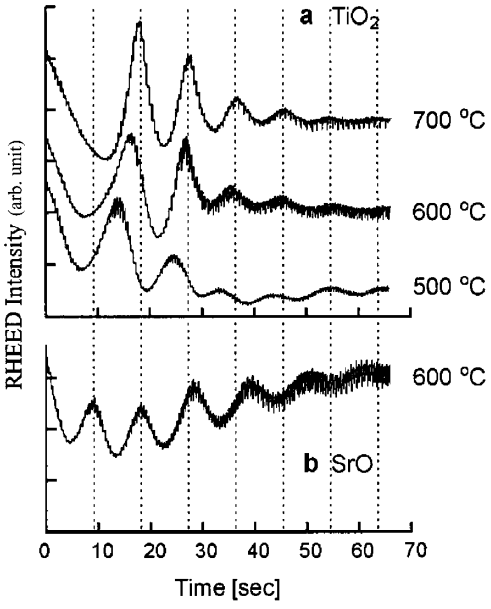

FIG. 12. RHEED intensity at different deposition temperatures on vicinal ($\alpha = 0.11°$) TiO_2-terminated $SrTiO_3$ substrates (a) The dotted lines indicate the time where completion of one unit-cell layer is expected at 700 °C and should be used as a guide for the eye. (b) RHEED intensity during the growth of $SrRuO_3$ on SrO-terminated $SrTiO_3$.

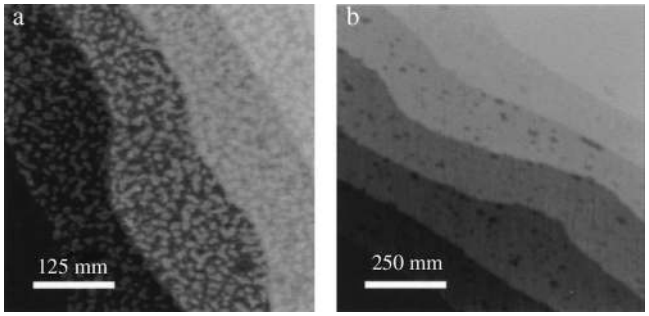

FIG. 13. AFM images of $SrRuO_3$ on TiO_2-terminated $SrTiO_3$ taken at the first minimum (a) and first maximum (b) of the RHEED intensity as presented in Fig. 12(a) at 700° C. From Rijnders *et al.*, 2004.

Choi *et al.* (2001) noted that because of the discrete nature of PLD, a modulated RHEED intensity results. During the laser pulse, a very fast deposition takes place, followed by a rearrangement (relocation) of the deposited atoms. This results in a relaxationlike behavior of the RHEED intensity. The amplitude and time constant of the RHEED intensity relaxation both increase if step-flow growth dominates, because of an increased diffusion length and a flat film surface.

The RHEED intensity variations, as recorded during initial growth of $SrRuO_3$ on $SrTiO_3$, and the RHEED patterns before and after deposition at azimuthal angles of 10° and 0° are shown in Fig. 14. Clear dots are observed belonging to a two-dimensional surface.

Depending on the average terrace length, the growth mode transitioned to a steady-state growth mode, layer by layer versus step-flow growth mode, more extensively described by Hong *et al.* (2005). Note that Yoo *et al.* (2005) studied the effect of oxygen partial pressure during PLD and observed a

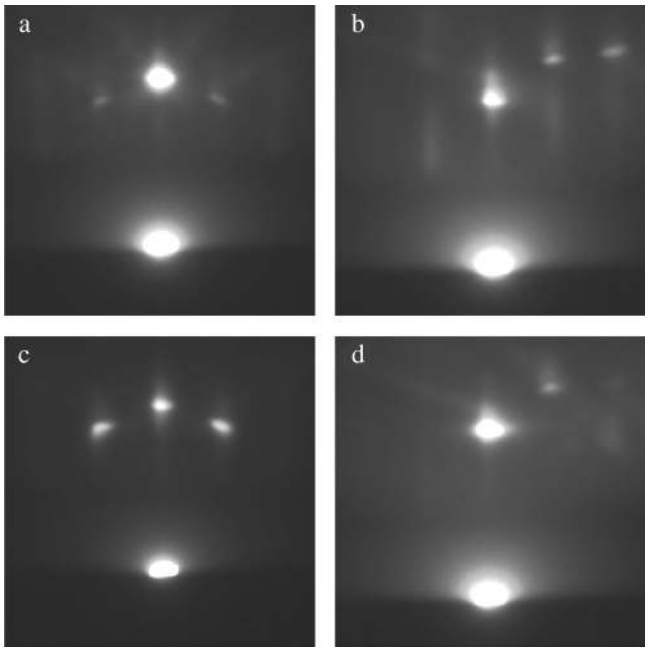

FIG. 14. RHEED patterns recorded before (a) and (b), and after (c) and (d) deposition of $SrRuO_3$. The azimuthal angle was set to 0° in (a) and (c), and to 10° in (b) and (d).

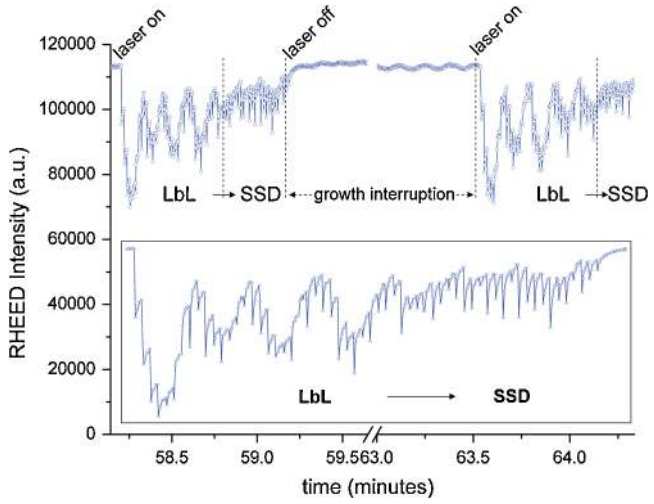

FIG. 15 (color online). RHEED specular spot intensity variation during $SrRuO_3$ growth (shown after deposition of ~60 nm) sequenced by interruptions, after 13 and 4 min of interruption (left and right parts of the graph, respectively). The inset at the bottom shows an enlargement of the former growth cycle. From Bachelet *et al.*, 2008.

3D-2D growth mode transition below 60 mTorr. Gupta, Hussey, and Shaw (1996) observed that growth at lower oxygen partial pressures using atomic oxygen resulted in a more layer-by-layer scenario as shown by 2D-intensity RHEED oscillations.

In a related study, Bachelet *et al.* (2008) observed that layer-by-layer growth recurred when deposition was interrupted, when just before the interruption step-flow-like growth was observed (see Fig. 15). This phenomenon probably results from step straightening during the time no deposition took place. For a detailed discussion of oxide growth mechanisms, see, for example, Christen and Eres (2008).

2. Monte Carlo simulations

The almost ideal growth behavior of $SrRuO_3$ makes it amenable to atomistic theoretical models. For example, in order to elucidate the transitions in thin film growth behavior, a solid-on-solid (SOS) model (Maksym, 1988) can be used. Using such a model, we can describe the crystallization process on the surface during growth in terms of the diffusion of the deposited material by means of single-particle lattice hopping. For simplicity, it is assumed that the ''particles'' are cubes of one pseudocubic unit-cell size deposited on a simple cubic lattice.

The diffusion kinetics are described by an Arrhenius hopping process (with a diffusion barrier E_D) on an $l \times l$ matrix. The diffusion barrier is comprised of two terms: $E_D = E_S + nE_N$, where E_S is the diffusion barrier of a free particle, n is the nearest-neighbor coordination ($n = 0$, 1, 2, 3, and 4) of each particle along the surface, and E_N is the energy of each bond formed with a nearest neighbor.

The hopping probability k is then given by

$$k = k_0 \exp\left(-\frac{E_S + nE_N}{k_B T}\right), \quad (1)$$

where k_0 represents the attempt frequency for atomic processes. The time scale for these simulations is determined by $1/R_{\text{total}}$ where R_{total} is the total rate of events; see also Maksym (1988).

Note that a change in E_D is expected after the deposition of one unit-cell layer, due to a different atomic termination and/or epitaxial misfit strain (Ratsch and Zangwill, 1993). The termination layer affects the diffusion barrier E_S, while the epitaxial strain affects both E_S and the detachment rate coefficient, determined by E_N. Misfit strain causes a reduction in the effective binding energy with a concomitant increase in the detachment rate (Ratsch, Nelson, and Zangwill, 1994). The latter is increased more for large islands than for small ones. As a consequence, misfit strain will hamper formation of large islands. Both decreases and enhancements of the energy barrier E_D are possible. A decrease will increase the rate of surface diffusion and favors step-flow growth because more atoms reach the terrace edge. A decrease in surface diffusion (e.g., due to an enhancement of the energy barrier) increases the nucleation probability on the terraces.

The growth of $SrRuO_3$ on the SrO termination layer (i.e., after the termination conversion described above), has been simulated using the SOS model. Figures 16(a)–16(c) show the simulated RHEED intensity variations during growth of five unit-cell layers on simulated substrates with different vicinal angles of 0.45°, 0.6°, and 1.0°. Note that the simulations show large RHEED oscillations at 2 Hz, the laser pulse rate, for reasons described in Sec. III.B.1; the observed oscillation amplitude is dramatically reduced by limited experimental time resolution. The values for E_S and E_N were 0.75 and 0.6 eV, respectively. A value of 10^{13} for the attempt frequency k_0 was used, while ϕ was set to zero. For the lowest vicinal angles, these values result in simulated growth behavior resembling that which is observed at 600 °C and a pulse repetition rate of 2 Hz; see Fig. 12(b).

Also, in the simulations, step-flow growth is observed for the highest vicinal angle of 1.0°, indicated by the steady RHEED intensity peaks. In this regime the particle diffusion length is expected to be, at a minimum, comparable to the terrace width. At the smaller vicinal angles, however, the growth is dominated by 2D nucleation and growth, as indicated by the initial intensity envelope oscillations that decay over the growth of several unit-cell layers. At a thickness that depends on the vicinal angle, the RHEED intensity peaks reach a steady value, indicating a constant step density.

Figure 17 shows the simulated surface morphology of 5 monolayers (ML) on a 0.6° miscut substrate. It shows 2D island growth on the terraces, and step advancement is clearly visible during growth of the first unit-cell layers. Nucleation on the terraces takes place, and subsequent deposition causes the islands to grow until they coalesce with the advancing steps. This process continues during the remainder of the deposition. The coalescence causes roughening of the step ledges and the transition to steady step density. After deposition of approximately four unit-cell layers, a steady-state surface step density is reached on the substrate with vicinal angle of 0.6°, and a ''constant'' surface morphology is observed.

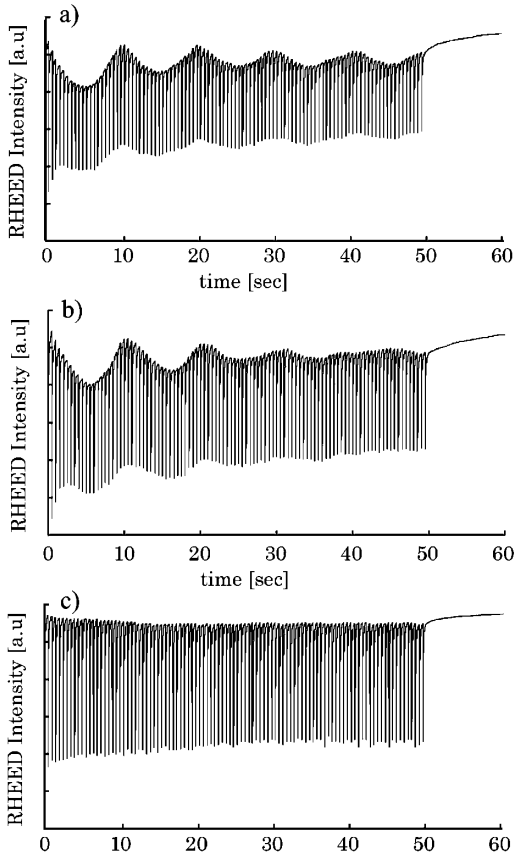

FIG. 16. Simulated RHEED intensity variations during growth of five unit-cell layers on substrates with different vicinal angles of 0.45° (a), 0.6° (b), and 1.0° (c). The deposition temperature was set to 600 °C, $E_S = 0.75$ eV, and $E_N = 0.6$ eV, the pulse repetition rate = 2 Hz, and the number of pulses needed for completion of one unit-cell layer is 20.

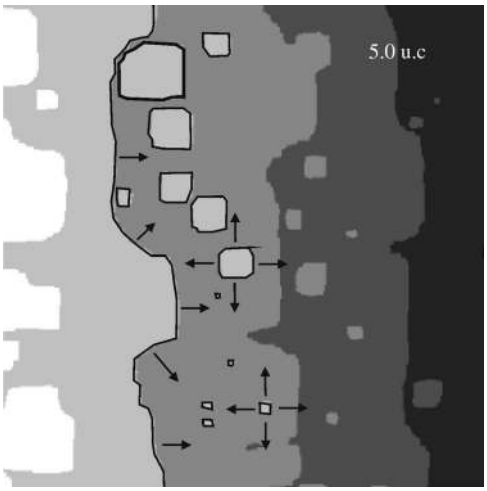

FIG. 17. Simulated surface morphology after five unit-cell layers on substrates with a vicinal angle of 0.6°. The advancing steps, indicated by the solid lines, coalesce with the growing islands on the terraces. In this simulation, the deposition temperature was set to 600 °C, $E_S = 0.75$ eV, and $E_N = 0.6$ eV, the pulse repetition rate = 2 Hz, and the number of pulses needed for completion of one unit-cell layer is 20.

In summary, based on these simulations, one can infer that the growth of $SrRuO_3$ on $SrTiO_3$ cannot be described by step-flow growth alone. On vicinal substrates with a terrace width comparable to the diffusion length of the deposit, nucleation occurs on the terraces. In another study by Yoo *et al.* (2006), different growth modes are related to magnetic anisotropy in $SrRuO_3$ films. We return to this point later in this review.

More generally, it can be said that while growing, the material behaves quite ideally, and thus represents a model

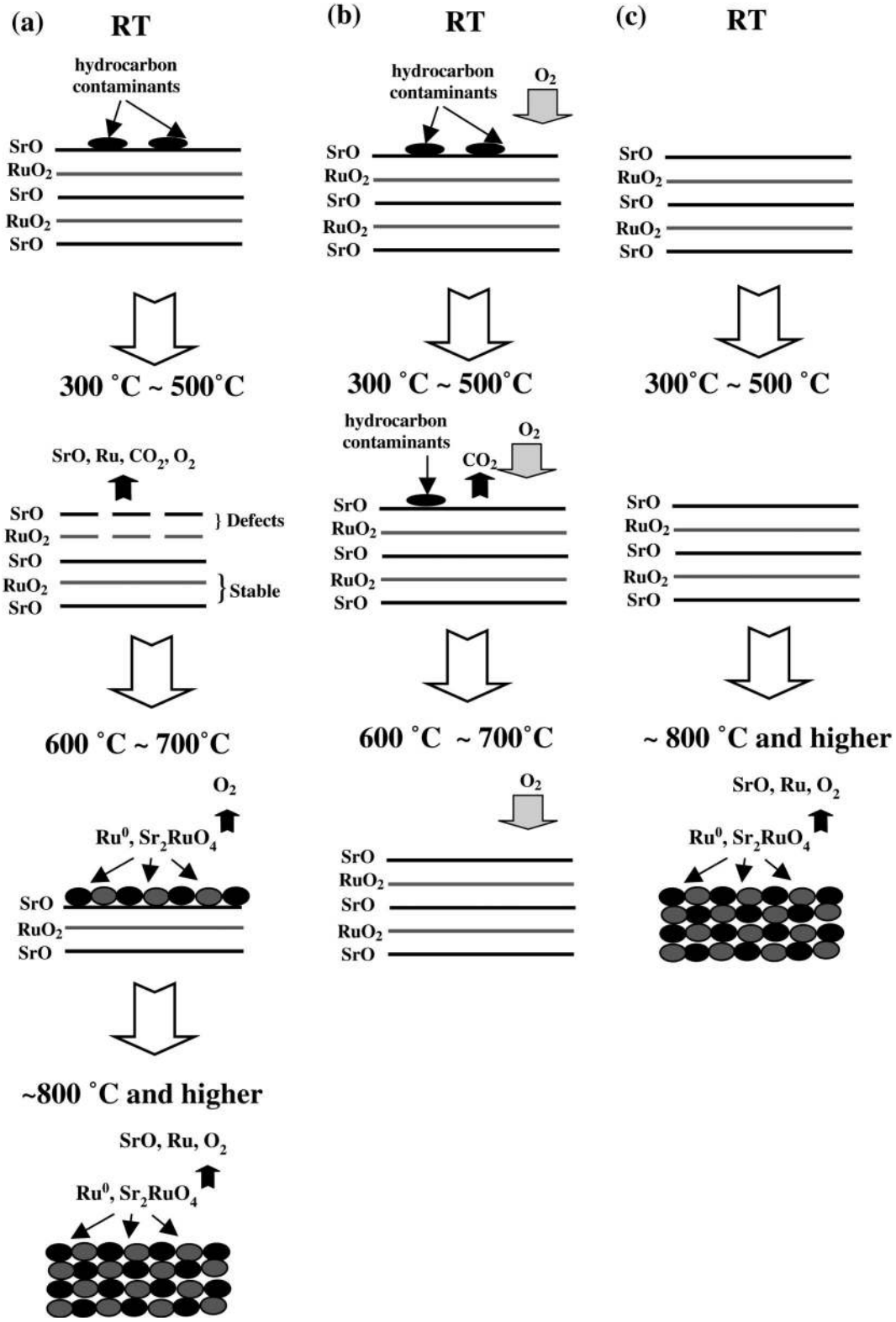

FIG. 18. Schematics of possible surface configurations at room temperature and after annealing to 300–500 °C and 600–700 °C for air-exposed $SrRuO_3$ films (a) in high vacuum (below 10^{-7} Torr), (b) in high O_2-O_3 pressure (~ 10 mTorr, ~7% ozone), and (c) in high vacuum (below 10^{-7} Torr) after annealing in O_2-O_3. From Shin *et al.*, 2005.

system for studying the growth kinetics of complex oxide materials. Looking forward, it would be desirable to develop molecular dynamics simulations that can describe the crystallization process in more depth, for example, by elucidating the role of oxygen pressure. In addition, it would be useful to study the connection between the RRR values observed in $SrRuO_3$ films deposited on higher-vicinal-angle substrates in combination with the relative low deposition rates as used in MBE growth. As will be shown in Sec. IV.E.2, this may be related to Ru vacancies.

3. Stability of $SrRuO_3$ thin film surfaces

The stability of the $SrRuO_3$ surface under various relevant conditions has been extensively studied by Shin *et al.* (2004, 2005), and Mlynarczyk *et al.* (2007). In Fig. 18 some of these results are summarized. Recently, the same authors investigated reconstructions on the $SrRuO_3$ surface by scanning tunneling microscopy (STM) and their effect on a subsequently grown ferroelectric film (Shin *et al.*, 2010). These experiments immediately show the importance of making *in situ* measurements: annealing, a standard cleaning procedure, tends to cause a previously exposed surface to react with carbohydrate contaminants. The use of *in situ* measurements is most important when carrying out photoemission experiments, or when films are very thin and the surface layer plays an important role in the overall properties of the film.

Finally, the stability of the $SrRuO_3/SrTiO_3$ interface was investigated theoretically by Albina *et al.* (2007) using DFT. In addition to the question of structural stability, band offsets and Schottky barrier heights were also estimated. This is important information when capping $SrRuO_3$ films (see also Sec. IV.D.3) or when $SrRuO_3$ is used in heterostructures (see Sec. V).

C. Structure of films on $SrTiO_3$ at room temperature

In order for $SrRuO_3$ to grow coherently on a single-crystal substrate, matching the in-plane lattice parameters to those of the substrate is required (Gan *et al.*, 1999). Any mismatch introduces strain (see Table I) that can affect the structural, magnetic, and electrical properties of the $SrRuO_3$ layer. In the case of $SrTiO_3$ substrates, the epitaxial $SrRuO_3$ films are subject to compressive strain in the plane. A schematic representation of the unit cell as it grows on $SrTiO_3$ in its distorted orthorhombic form is shown in Fig. 19. Note that the c axis is defined as the in-plane lattice parameter and that $SrRuO_3$ grows on $SrTiO_3$ with the [110] direction pointing out of plane. The effects of the induced strain are discussed in Secs. IV.A and IV.B. As mentioned, $SrRuO_3$ has an orthorhombic structure at room temperature. A pseudocubic perovskite structure, however, can be constructed with lattice parameters close to the lattice parameters of the cubic perovskite $SrTiO_3$ ($a = 3.905$ Å). The lattice mismatch at room temperature is approximately 0.45%.

Various studies have shown that untwinned, single-crystalline thin films can be grown on vicinal $SrTiO_3$ using sputter deposition (R. A. Rao *et al.*, 1997; Gan *et al.*, 1998), reactive electron beam evaporation (Marshall *et al.*, 1999), and pulsed laser deposition (Jiang, Pan, and Chen, 1998; Jiang *et al.*, 1998a; Jiang *et al.*, 1998b). Measurements on

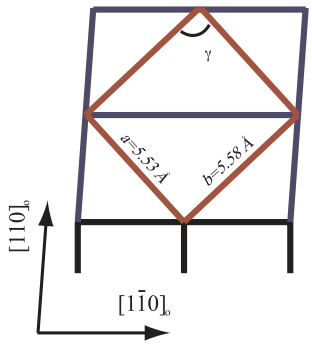

FIG. 19 (color online). A schematic of the $SrRuO_3$ distorted orthorhombic crystal structure as it grows on $SrTiO_3$ at room temperature, with a view along the [001] direction. The orthorhombic cell parameters a and b are indicated as well as the distortion angle $\gamma = 89.4°$. The in-plane c lattice parameter is strained to $SrTiO_3$ and 7.81 Å in length. Note that the [110] axis is not perfectly parallel to the surface normal.

films of $SrRuO_3$ grown on $SrTiO_3$ all show a distorted orthorhombic unit cell at room temperature, just as for the bulk material. Differences in symmetry from the bulk material arise when either the substrate (i.e., the strain) is changed or the sample is heated, as discussed later.

D. Films at elevated temperatures and twinning

From bulk studies, it is well established that the crystal symmetry of $SrRuO_3$ increases with increasing temperature (see Sec. II). Thin films behave similarly but can exhibit shifted transition temperatures. For example, Maria, McKinstry, and Trolier-McKinstry (2000) reported that thin films of $SrRuO_3$ grown on $SrTiO_3(001)$ underwent an orthorhombic-to-tetragonal (O-T) structural phase transition at a somewhat lower temperature of ~350 °C than that of the bulk. They also measured a tetragonal-to-cubic (T-C) phase transition temperature of 600 °C, but this was obtained from a bulk $SrRuO_3$ sample. Assuming that the T-C transition in a film occurs not too far from this temperature, these results imply that $SrRuO_3$ exhibits cubic symmetry during film synthesis, which is typically in the range of 600–700 °C (Maria, McKinstry, and Trolier-McKinstry, 2000).

Since the T-C transition used in the above argument was observed on a powder $SrRuO_3$ sample, it is still not completely clear what crystal symmetry an epitaxial $SrRuO_3$ layer possesses during growth that is constrained by the substrate. Obviously, to clarify the presence of one or the other symmetry, it would be necessary to measure the structure of a $SrRuO_3$ layer at high temperatures, under the conditions that it is normally deposited on single-crystal substrates.

Choi *et al.* (2010) synthesized fully commensurate, single-crystal $SrRuO_3$ thin films under both compressive and tensile strains on (001) $SrTiO_3$, (110) $DyScO_3$ (DSO), and (110) $GdScO_3$ (GSO) substrates using pulsed laser deposition. They also investigated the effects of strain on the structural phase transition temperatures using both temperature-dependent x-ray diffraction (XRD) measurements and *in situ* high-pressure RHEED. From these results, they suggested how

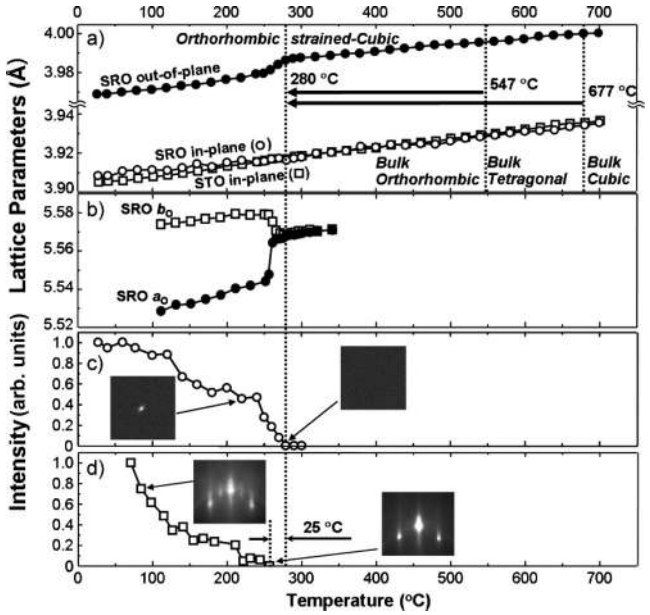

FIG. 20. (a) Temperature dependence of in-plane and out-of-plane lattice parameters of a compressively strained $SrRuO_3$ thin film grown on an $SrTiO_3$ substrate. Transition temperatures for unstrained bulk $SrRuO_3$ are displayed for comparison. (b) Temperature dependence of the orthorhombic lattice parameters a_o and b_o of an $SrRuO_3$ film grown on an $SrRuO_3$ substrate. (c) The normalized integral intensity of the $(113)_o$ XRD reflection as a function of temperature. The insets show 2D images of the $(113)_o$ peak obtained at different temperatures. (d) Normalized integral intensity of the (0 1/2) RHEED pattern as a function of temperature with insets of RHEED images obtained at different temperatures. From Choi *et al.*, 2010.

compressive and tensile strains modify the crystal symmetry of $SrRuO_3$. Biaxial compressive strain imposed by (001) $SrTiO_3$ substrates shifts the orthorhombic transition temperature of $SrRuO_3$ from 547 °C (the bulk transition temperature) to 280 °C, as summarized in Fig. 20. More interestingly, biaxial tensile strain by (110) DSO and (110) GSO substrates maintained a strained cubic phase to room temperature (see also Fig. 50). This result guides the growth and domain engineering of multifunctional oxide heterostructures on single-crystal $SrRuO_3$ bottom electrodes.

Vailionis, Siemons, and Koster (2007) also reported a study of the temperature-dependent structural transition of $SrRuO_3$ films coherently grown on $SrTiO_3$(001) substrates by means of high-resolution x-ray diffraction using laboratory as well as synchrotron radiation sources. Their main result is shown in Fig. 21. They point out that it is difficult to see the T-C transition in a thin oriented $SrRuO_3$ film because it involves only small displacements of light oxygen atoms, associated with RuO_6 octahedral rotation around the cubic [001] $SrRuO_3$ axis. Using $SrRuO_3$ powder diffraction pattern simulations, they established the fact that the $SrRuO_3$(211) diffraction peak is sensitive to oxygen rotation and is absent in the cubic phase. The $SrRuO_3$(211) peak intensity gradually decreases with increasing temperature, indicating the rotation of the oxygen atoms, but it does not vanish up to temperatures of ~730 °C. From this work they concluded that the symmetry of the $SrRuO_3$ unit cell during growth is tetragonal.

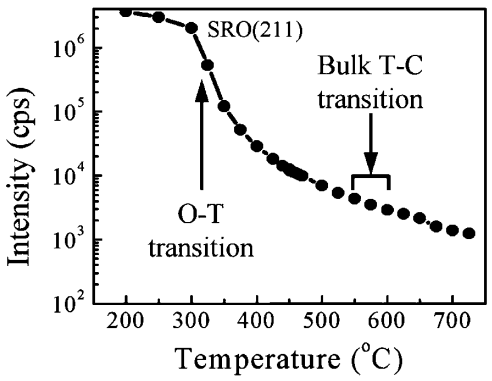

FIG. 21. Intensity of the $SrRuO_3$ (211) peak as a function of temperature. The nonzero intensity indicates that $SrRuO_3$ possesses a tetragonal symmetry up to 730 °C. From Vailionis, Siemons, and Koster, 2007.

This observation offers an elegant explanation for the influence of substrate vicinal angle α and miscut angle β on the formation of crystallographic twins during $SrRuO_3$ film growth, as studied by Gan, Rao, and Eom (1997) with $SrTiO_3$ substrates; see Fig. 22. They showed that, using substrates with large vicinal angle ($\beta > 1.9°$) and an orientation close to the [010] axis, single-domain $SrRuO_3$ with good crystalline quality could be grown. As shown in Fig. 22, the fourfold symmetry of $SrTiO_3$[001] is broken by exposing both the [010] and [100] planes at the surface steps. Two in-plane epitaxial arrangements are possible depending on the direction of step flow: $SrRuO_3[001] \parallel SrTiO_3[100]$ and $SrRuO_3[\bar{1}10] \parallel SrTiO_3[010]$, or $SrRuO_3[001] \parallel SrTiO_3[010]$ and $SrRuO_3[\bar{1}10] \parallel SrTiO_3[100]$, marked in Fig. 22 by **A** and **B**, respectively. Gan, Rao, and Eom (1997) argued that the observed single-domain film growth resulted from the alignment of the substrate steps with the $SrTiO_3$ axes, and that this promoted uniaxial step-flow growth. XRD scans of a $SrRuO_3$ film deposited on a vicinal (0.2°) $SrTiO_3$ substrate shows a single-domain structure, indicated by the twofold symmetry; see Fig. 23.

After their observation of tetragonal symmetry at high temperatures, Vailionis, Siemons, and Koster (2007)

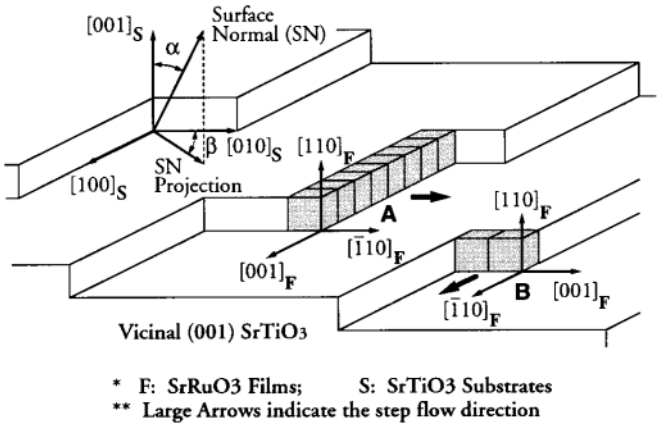

FIG. 22. Schematic diagram of a vicinal $SrTiO_3$ (001) substrate showing miscut angle α and miscut direction β, as well as the epitaxial arrangement of two types of step-flow growth of $(110)^o$ $SrRuO_3$ domains.

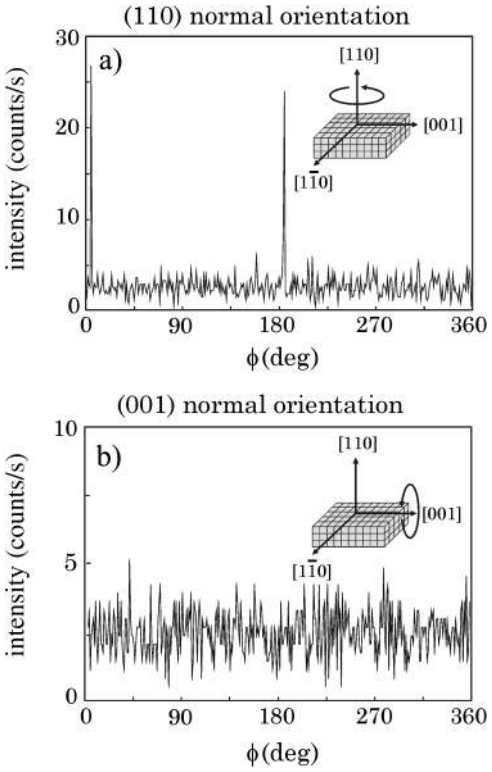

FIG. 23. Typical XRD ϕ scans indicating a single-domain structure of $SrRuO_3$ on vicinal (0.2°) $SrTiO_3$. The twofold symmetry in (a) and the absence of peaks in (b) indicate a single-domain structure.

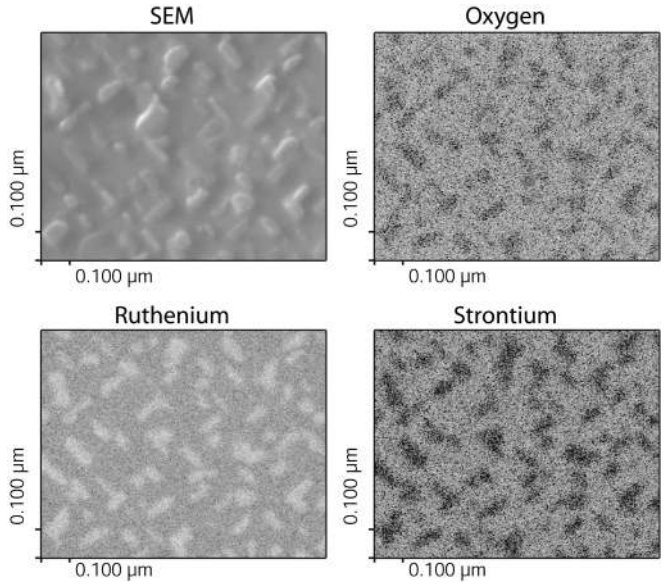

FIG. 24. A SEM picture of a ruthenium rich $SrRuO_3$ thin film with the associated elemental maps as obtained with Auger electron spectroscopy. The precipitations show up clearly in all the scans and contain no strontium, but seem ruthenium rich and oxygen poor. The precipitations are almost certainly RuO_2 and might show up as oxygen poor due to a change in the sensitivity factor between $SrRuO_3$ and RuO_2.

suggested an alternative mechanism of single-domain growth. They argued that for a tetragonal unit cell where $c > a = b$, $SrRuO_3$ will tend to align its c axis along the steps as they attach during step-flow growth. If the step edges run only along $SrTiO_3$[100] or [010] directions then a single-domain $SrRuO_3$ layer is formed. On the other hand, if the step edges run along a direction at too large an angle to [100] or [010], a twinned structure will result from the serrated nature of the step edge. This is exactly the behavior observed earlier by Gan, Rao, and Eom (1997).

E. Thin film parameters for systematic physical studies

The nearly perfect crystal structure found in the best $SrRuO_3$ thin films and its malleability make $SrRuO_3$ a unique model system for systematic study of the effects of less perfect structures. Therefore, the physical properties of $SrRuO_3$ have been studied extensively as a function of thin film parameters, such as stoichiometry, strain, and thickness. Here we review the most common techniques and conditions that allowed groups to vary these parameters in a systematic manner. In addition, the surface preparation and surface stability of the $MRuO_3$ system will be briefly addressed in this section.

1. Parameters that control stoichiometry

Siemons *et al.* (2007) pointed out that the stoichiometry of $SrRuO_3$ thin films is extremely dependent on the oxygen activity during deposition. For molecular beam epitaxy (e-beam evaporation or MBE) this can be independently varied by controlling the flux of molecular or atomic oxygen.

It appears that the oxygen plays a role in the sticking ability of the ruthenium, possibly through the formation of volatile RuO_4 (Bell and Tagami, 1963; Nakahara *et al.*, 2001). At relatively low oxygen activity the stoichiometry is mostly determined by the supplied Sr:Ru ratio. With excess Ru, RHEED, scanning electron microscopy (SEM), TEM (Oh and Park, 2003), and Auger spectra (see Fig. 24) all reveal precipitation of RuO_2, and the Ru 3d core-level spectra show strong screened peaks typical of RuO_2 (see Fig. 44). A thorough transmission electron microscopy study of excess Ru incorporation in the structure has been made by Oh and Park (2003).

At intermediate oxygen activity, conditions are most favorable to achieve optimal stoichiometry. RHEED shows 2D growth, and the best values for resistivity and residual resistivity ratios ($R_{300\,K}/R_{4\,K}$) are obtained.

Finally, at high oxygen activity, Ru vacancies are unavoidable, independent of the ratio of Sr to Ru in the supplied vapor. RHEED shows two-dimensional growth, layer by layer or even step flow (Rijnders *et al.*, 2004). Also, XRD clearly shows a modification in the unit cell, indicative of Ru vacancies (Dabrowski *et al.*, 2004). Consequently, Siemons *et al.* (2007) argued that PLD films are inherently ruthenium deficient, because a high (atomic) oxygen pressure exists within the plume, in addition to the background activity. PLD offers the advantage of making consistent-quality films, but they will be Ru poor. On the other hand, Siemons *et al.* (2007) also showed that, even when ruthenium vacancies are present, the crystallinity of the material remains the same as the stoichiometric films.

There is no indication that oxygen vacancies play a significant role as a defect, but they cannot be distinguished from the formation of ruthenium vacancies on the basis of lattice constants only. In a study of similar (bulk) ruthenium-deficient samples, oxygen vacancies were not observed (Dabrowski *et al.*, 2004). Other studies of variations in stoichiometry were reported by Takahashi *et al.* (2002), where a comparison was made between MOCVD and sputter deposition of $SrRuO_3$ on $(LaAlO_3)_{0.3}$-$(Sr_2AlTaO_6)_{0.7}$ (LSAT) and $SrTiO_3$, resulting in unit-cell volume changes that suggest variations in stoichiometry.

2. Films on different substrates and strain

Change in the applied strain is most easily achieved by changing the substrate material. On $SrTiO_3$, the applied strain is compressive in plane, but tensile strain can also be achieved, for example, with $DyScO_3$. Recently, Vailionis, Siemons, and Koster (2008) measured the structural properties of $CaRuO_3$ and $SrRuO_3$ films grown epitaxially on various substrates. Their main results are listed in Table II. As can be seen from the table, all $ARuO_3$, A = (Ca, Sr) layers under compressive stress demonstrate a γ angle (defined in Fig. 19) smaller than 90°, while layers under tensile stress exhibit γ angles larger than 90°. The γ angle variation is consistent with the sign of the strain, indicating that the $ARuO_3$ unit cell, in addition to variations of the a, b, and c lattice parameters, utilizes this additional degree of freedom to accommodate the mismatch between the substrate and the layer. In various studies, it was observed that when the negative mismatch becomes relatively large, the $ARuO_3$ layer stabilized in a tetragonal instead of an orthorhombic structure. For specific examples, see $SrRuO_3$ on $DyScO_3$ and $CaRuO_3$ on $SrTiO_3$ (Vailionis, Siemons, and Koster, 2008) or $SrRuO_3$ on $GdScO_3$ Choi *et al.* (2010). A recent article by Vailionis *et al.* (2011) gave a general description of perovskite materials under tensile or compressive strain in terms of octahedral rotations.

As discussed in Sec. III.D, the O-T transition in thin films is induced by epitaxial strain at room temperature, whereas in bulk materials it takes place at high temperatures. It is important to note that the O-T transition occurs at different mismatch values for $SrRuO_3$ and $CaRuO_3$. For ease of comparison, we can define an average lattice mismatch $m_{av} = (m_{[110]} + m_{[001]})/2$, where the [110] and [001] directions are referred to the orthorhombic coordinate system of the $ARuO_3$ film. Vailionis, Siemons, and Koster (2008) found that while tetragonal $SrRuO_3$ could be stabilized at room temperature on $DyScO_3$ with an average lattice mismatch $m_{av} = -0.538\%$, $CaRuO_3$ remained orthorhombic on $NdGaO_3$ with $m_{av} = -0.64\%$. Note that the mismatch m is defined as $[a_l(R) - a_s]/a_s$ and strain e is defined as $a[l - a_l(R)]/a_l(R)$, where the subscripts l and s stand for "layer" and "substrate," respectively. (R) denotes relaxed lattice parameters.

Tetragonal $CaRuO_3$ can be stabilized at room temperature on $SrTiO_3$ because of its much larger mismatch, $m_{av} = -1.38\%$. The large dissimilarity was explained by the orthorhombicity factor a/b of the two materials. As shown in Table II, in bulk $CaRuO_3$ $a/b = 1.0318$, much larger than in $SrRuO_3$, where $a/b = 1.0066$. Consequently, $CaRuO_3$ requires a larger applied strain to switch its unit cell from orthorhombic to tetragonal. Other related studies have been carried out by Ito, Masumoto, and Goto (2009), who grew $SrRuO_3$, $CaRuO_3$, and $BaRuO_3$ on $LaAlO_3$ and observed both small surface roughness and high conductivity with the $CaRuO_3$ films, which have the best lattice match with the substrate material.

As seen in Sec. IV, the change in the structure of the unit cell has a profound impact on the transport and magnetic properties of the films.

IV. PHYSICAL PROPERTIES

As seen in the previous section, under optimized conditions high-quality single-crystal thin films can be grown. At the same time, many physical measurements have been made on films that are less ideal, complicating the task of reviewing the physical properties of $SrRuO_3$ thin films comprehensively. Indeed the physical properties of $SrRuO_3$ thin films vary considerably as a function of numerous parameters, including the substrate used, the degree (and nature) of off-stoichiometry, strain, disorder, thickness, and more.

Some properties are more sensitive than others. For example, the magnetic properties are particularly sensitive. As discussed below, high-quality MBE-grown films exhibit uniaxial magnetocrystalline anisotropy. On the other hand, if a film contains regions in which the uniaxial anisotropy is aligned in different directions relative to the film plane, the "effective" measured magnetic anisotropy will be different and so will be the magnetotransport properties.

TABLE II. A summary of the structural properties of $CaRuO_3$ and $SrRuO_3$ films grown on various substrates. From Vailionis, Siemons, and Koster, 2008.

Substrate	Lattice parameters (Å and deg) $SrRuO_3$				Strain (%)		a/b
	a	b	c	γ	[001]	[−110]	
$SrTiO_3$(001)	5.529	5.577	7.810	89.41	−0.441	−0.439	1.0087
$DyScO_3$(110)	5.560	5.561	7.903	90.49	0.744	0.640	1.0002
Bulk $SrRuO_3$	5.530	5.567	7.845	90.00	···	···	1.0066
			$CaRuO_3$				
	a	b	c	γ	[001]	[−110]	
$NdGaO_3$(110)	5.359	5.535	7.706	90.28	0.745	0.392	1.0328
$SrTiO_3$(001)	5.461	5.463	7.760	90.42	1.451	0.778	1.0004
Bulk $CaRuO_3$	5.354	5.524	7.649	90.00	···	···	1.0318

To deal reasonably with the situation, in reviewing the magnetic and transport properties of $SrRuO_3$ films, we focus first on the properties of films grown on $SrTiO_3$ substrates, which as we have seen are in general of the highest quality. For example, these films typically exhibit the highest resistivity ratios (assuming constant growth parameters). Other properties appear to be less sensitive to the growth method. Finally, we end this section by reviewing the effect of various parameters on the physical properties with special emphasis on stoichiometry and film thickness.

A. Magnetism

In this section, we review the main magnetic properties of $SrRuO_3$ films. We discuss the itinerant nature of the magnetism, which yields spin polarization of the conducting electrons and affects the low-temperature excitations. We address the strong uniaxial and temperature-dependent (also in its direction) magnetocrystalline anisotropy exhibited by these materials, which in turn leads to strong magnetic anisotropy both above and below T_C. We also discuss the nature of the magnetic transition, which exhibits an Ising universality class and the formation of striped magnetic domain structures.

1. Magnetic order

Epitaxial films of $SrRuO_3$ undergo a ferromagnetic phase transition at a Curie temperature of ~150 K (Eom *et al.*, 1992) [~ 160 K in bulk samples and unstrained films (Kanbayasi, 1976a; Gan *et al.*, 1998]. The measured moment above T_C is $2\mu_B$, which implies, in an oversimplified local description, a low-spin state of the four ruthenium electrons. The spontaneous magnetization in the limit of zero temperature is $1.4\mu_B$, consistent with band calculations that show strong $2p$-$4d$ hybridization (Allen *et al.*, 1996a; Singh, 1996a).

Magnetism in $SrRuO_3$ is itinerant and primarily due to electrons with Ru $4d$ character. The ratio q between the high-temperature moment and the zero-temperature saturated magnetization of $SrRuO_3$ is ~1.3. The q value is a common measure of the degree of itinerancy in the magnetism: $q \sim 1$–2 indicates strong (i.e., more local in real space) itinerant ferromagnetism, while higher values of q indicate weak and less localized magnetism. For a review, see, e.g., Moriya (1987). Therefore, we expect the magnetic properties of $SrRuO_3$ to be similar to those of the elemental $3d$ ferromagnets nickel, cobalt, and iron for which $q \sim 1$–2, and different, for example, from the weak itinerant ferromagnet $ZrZn_2$ for which $q \geq 5$.

$SrRuO_3$ is a minority-band itinerant ferromagnet; namely, the average spin polarization of the charge carriers at the Fermi surface is in opposite direction to its magnetization. By measuring the magnetoresistance (MR) of a ferromagnet-insulator-ferromagnet tunnel junction, the spin polarization in $SrRuO_3$ was determined to be $P = -9.5\%$. These experiments also provided a test of the empirical Julliere model (Worledge and Geballe, 2000), which should be comparable to a spin polarization determined by Andreev reflections. Yet, from the experiments by Nadgorny *et al.* (2003) and Raychaudhuri *et al.* (2003), who used Nb point contacts, in the ballistic limit a value of -50% was obtained, noting that this technique is insensitive to the sign of the polarization. The observed numerical difference might have been due to the fact that the quality of the barrier used in the MR experiments is limiting. Interestingly, the two band structure calculations so far published on this compound predict small values: $P = -9\%$ (Singh, 1996a; Mazin and Singh, 1997a) and $P = -20\%$ (Allen *et al.*, 1996a).

There have been several reports claiming that $SrRuO_3$ is a spin glass (Palai *et al.*, 2009). There has also been a report claiming exchange bias behavior attributed to the spin-glass property (Pi *et al.*, 2006b). However, this report was retracted (Pi *et al.*, 2006a) following a comment by Klein (2006). In our view, there is overwhelming evidence that $SrRuO_3$ is ferromagnetic and the observed "spin-glass-like features" are due to the high coercivity of $SrRuO_3$.

2. Magnetic anisotropy

The reported magnetocrystalline anisotropy of bulk materials is somewhat confusing. Kanbayasi (1978) reported torque measurements of different phases of single crystals. In one case, he reported pseudocubic anisotropy with the $\langle 110 \rangle_{ps}$ directions (in the cubic frame) being the easy axes and an anisotropy field of ~2 T. However, he also reported on a tetragonal phase with easy axes only in the (001) plane (Kanbayasi, 1976b) and an anisotropy field (inferred from the reported anisotropy energy) larger than 10 T.

The study of magnetocrystalline anisotropy on twin-free films grown on miscut $SrTiO_3$ substrates indicates that there is a single easy axis which lies in the (001) plane. Above T_C the easy axis is the b axis which is ~45° relative to the film normal. This was demonstrated by Kats *et al.* (2005) who used measurements of the extraordinary Hall effect (EHE) using the relation $R_{EHE} = \mu_0 R_s M_\perp t$, where R_s is the extraordinary Hall coefficient, $M_\perp$ is the component of the magnetization perpendicular to the film plane, and t is the thickness of the sample. They showed (see Figs. 25 and 26) that the

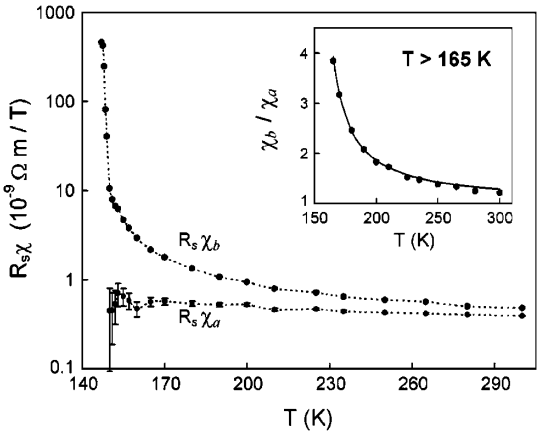

FIG. 25. Susceptibility along the crystallographic directions [100](χ_a) and [010](χ_b) as a function of temperature, on a semilogarithmic plot. The values are multiplied by R_s, whose temperature dependence is expected to be smooth. The error bars for $R_s\chi_a$ reflect an uncertainty of up to 2° in θ. The dashed lines are guides to the eye. The inset shows the ratio χ_b/χ_a for $165 < T < 300$ K. The solid curve is a fit to $(T - T_{c,a}^{MF})/(T - T_{c,b}^{MF})$ with $T_{c,a}^{MF} = 109$ K and $T_{c,b}^{MF} = 150.5$ K. From Kats *et al.*, 2005.

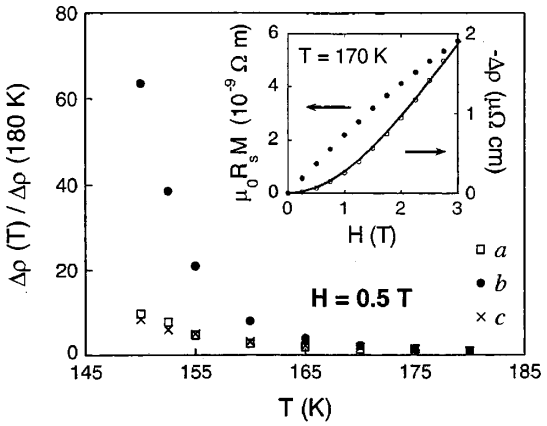

FIG. 26. Magnetoresistance as a function of temperature with a field of 0.5 T applied along the different crystallographic directions (the values are normalized to the values at 180 K). The inset shows the magnetization ($\mu_0 R_s M$) and MR ($\Delta\rho$) as a function of a field (applied along the b direction, at $T = 170$ K). The solid curve is a fit to $\Delta\rho \propto -M^2$. From Kats *et al.*, 2005.

susceptibility along the b axis χ_b exhibits a striking divergence at T_C, becoming several orders of magnitude larger than χ_a. Using magnetoresistance measurements, they showed that the magnetic response along the c axis (which is in the film plane and therefore cannot be measured using EHE) is similar to the response along the a axis.

Below T_C there is an orientational transition (Lifshitz, Landau, and Pitaevskii, 1984) in which the easy axis continuously changes its angle θ with respect to the normal from ~45° to ~30° at low temperatures, at a practically constant rate of ~0.1 deg/K (Klein, Dodge, Ahn, Reiner *et al.*, 1996) (see Fig. 27).

The uniaxial anisotropy energy below T_C can be described by $E_{\text{anis}} = K\sin^2\theta$, where θ is the angle between the magnetization and the easy axis and K is a weakly temperature-dependent anisotropy constant whose low-temperature value is $(1.2 \pm 0.1) \times 10^7$ ergs/cm^3. This gives an effective anisotropy field of $h_a = 2K/M \approx 12$ T. As described in Sec. IV.C.4, recent ferromagnetic resonance measurements using the time-resolved magneto-optic Kerr effect give $h_a \approx 7.2$ T, with an easy axis consistent with magnetization measurements. This measurement provides an accurate value of the true anisotropy field at small θ, whereas the static measurements provide an effective anisotropy that is useful for a simplified understanding of magnetization reversal.

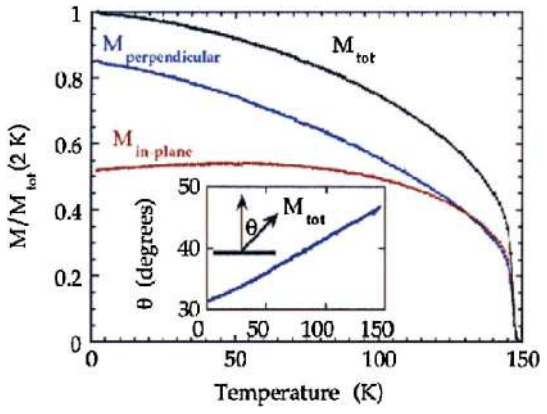

FIG. 27 (color online). Temperature dependences of the in-plane, out-of-plane, and total remanent magnetizations of a $SrRuO_3$ film. The film was cooled in a saturating field down to 5 K and the magnetization was measured upon warming after removing the applied field. The temperature dependence of the angle between the magnetic moment and the normal to the film plane is also shown. From Klein, Dodge, Ahn, Reiner *et al.*, 1996.

The intrinsic nature of the uniaxial magnetocrystalline anisotropy in the films was demonstrated by Marshall *et al.* (1999) who studied the magnetic microstructure of $SrRuO_3$ thin films using Lorentz TEM and found that, irrespective of the orientation of the orthorhombic unit cell relative to the $SrTiO_3$ substrate, the easy axis is close to the b axis.

Other reports indicated that there is uniaxial anisotropy with the easy axis at 5 K at ~26° relative to the film normal (Kolesnik *et al.*, 2006; Yoo *et al.*, 2006). Structural analysis by x-ray diffraction experiments showed that this unique transformation of magnetic anisotropy is related to a distortion from the bulk orthorhombic lattice into a triclinic structure in the epitaxial film, such that the lattice along the [010] direction expands while its [100] counterpart contracts as shown in Fig. 19 (Gan *et al.*, 1999). The distortion appears to arise from rotation and tilt of RuO_6 octahedra. The finding indicates that the magnetic anisotropy in epitaxial $SrRuO_3$ films is rooted in the crystalline anisotropy influenced by strong spin-orbit interactions.

There have been reports of other types of magnetocrystalline anisotropy, which most likely can be attributed to twinning, as demonstrated by Kolesnik *et al.* (2006), who compared the anisotropy in twinned and untwinned films, as well as nonstoichiometric films. Finally, Herranz *et al.* (2006) showed a possible relationship between anisotropies and the growth mechanism.

We briefly discuss the effect of epitaxial strain in Sec. IV.E.1 and the effect of substitutions on magnetic anisotropy in Sec. IV.E.3, respectively. Also, in Sec. IV.E.5, the effect of the film thickness on magnetic anisotropy is discussed.

3. Critical behavior

The magnetic phase transition of single crystals of $SrRuO_3$ has been studied by Kim *et al.* (2003). They found that the critical exponents associated with the magnetization are $\beta = 0.50 \pm 0.03$, $\gamma = 0.99 \pm 0.03$, and $\delta = 3.1 \pm 0.3$, all within error bars of mean-field values down to reduced temperatures of 0.0003. Kats *et al.* (2001) studied the magnetic phase transition in $SrRuO_3$ films based on magnetoresistance measurements. They found $\beta = 0.34 \pm 0.02$, and essentially the same γ from data below and above T_C, $\gamma = 1.14 \pm 0.07$ and $\gamma = 1.17 \pm 0.14$, respectively. These values suggest that $SrRuO_3$ films belong to the Ising universality class. This result is consistent with the uniaxial magnetocrystalline anisotropy described above. It is unclear if the differences between these two studies are due to a difference in the analysis or to intrinsic differences between bulk samples and thin films.

4. Low-temperature excitations

The remanent magnetization of $SrRuO_3$ shows a pronounced temperature dependence at low temperatures (see Fig. 27). This temperature dependence is attributed to spin-wave and Stoner excitations, which yield $T^{3/2}$ and T^2 terms, respectively (Klein *et al.*, 1995a). By contrast, according to Snyder (1997), the temperature dependence of the magnetization of bulk samples of $SrRuO_3$ includes only a T^2 term. Also, their T_C and magnetocrystalline anisotropy differ from that found in films. Fitting the temperature dependence of the full magnetic moment assuming $M/M_0 = 1 - AT^{3/2} - BT^2$ yields $A = 1 \times 10^{-4}$ $(1/K^{3/2})$ and $B = 2 \times 10^{-5}$ $(1/K^2)$, close to the theoretical predictions. The contribution of the two kinds of excitations was predicted theoretically by Herring and Kittel (1951) and was observed in other strong itinerant ferromagnets as well; see, for example, Argyle, Charap, and Pugh (1963) and Kaul (1991).

5. Magnetic domains

Lorentz microscopy studies of $SrRuO_3$ films (Marshall *et al.*, 1999) (see Fig. 28) show domain structures in the form of stripes parallel to the in-plane projection of the b axis. For films grown on miscut $SrTiO_3$ the b axis is out of plane and the low-temperature width of the stripes is ~200 nm. When the film grows with the b axis in the film plane, the low-temperature width of the stripes is more than a micron. This difference is attributed to shape dependence of the demagnetization factor. The domain-wall width cannot be measured directly with Lorentz microscopy, and based on the magnetic anisotropy, it was estimated to be ~3 nm (see also Sec. IV.A.2). Scanning tunneling spectroscopy measurements (Asulin *et al.*, 2006) on thin epitaxial $SrRuO_3/(100)YBa_2Cu_3O_{7-\delta}$ ferromagnet and superconductor bilayers suggest that the superconductor order parameter survives in regions in the vicinity of the domain walls, and based on the width of these regions, the domain-wall width was estimated to be less than 10 nm (see Fig. 29). The nature of the domains and the domain walls make them attractive for transport measurements, as discussed below. The stray field generated by the domain structure has also been used to suppress the superconducting critical current in Nb films in bilayers with $SrRuO_3$ (Feigenson *et al.*, 2005).

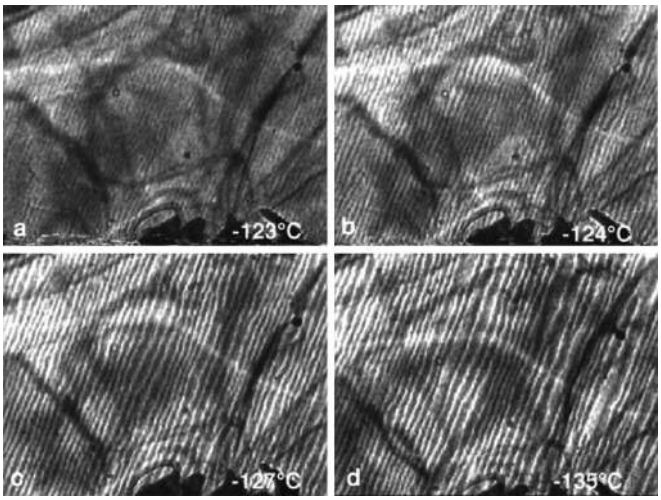

FIG. 28. Sequence of video images with Lorentz transmission electron microscopy during cooling of the $SrRuO_3$ film. The initial faint stripe structure (a) increases rapidly in contrast as the magnetization increases (b). Pairs of black-and-white domain walls annihilate to increase the average wall spacing (c). This process continues for about 15 K below T_C (d), and the wall structure remains unchanged with further cooling down to about 100 K. From Marshall *et al.*, 1999.

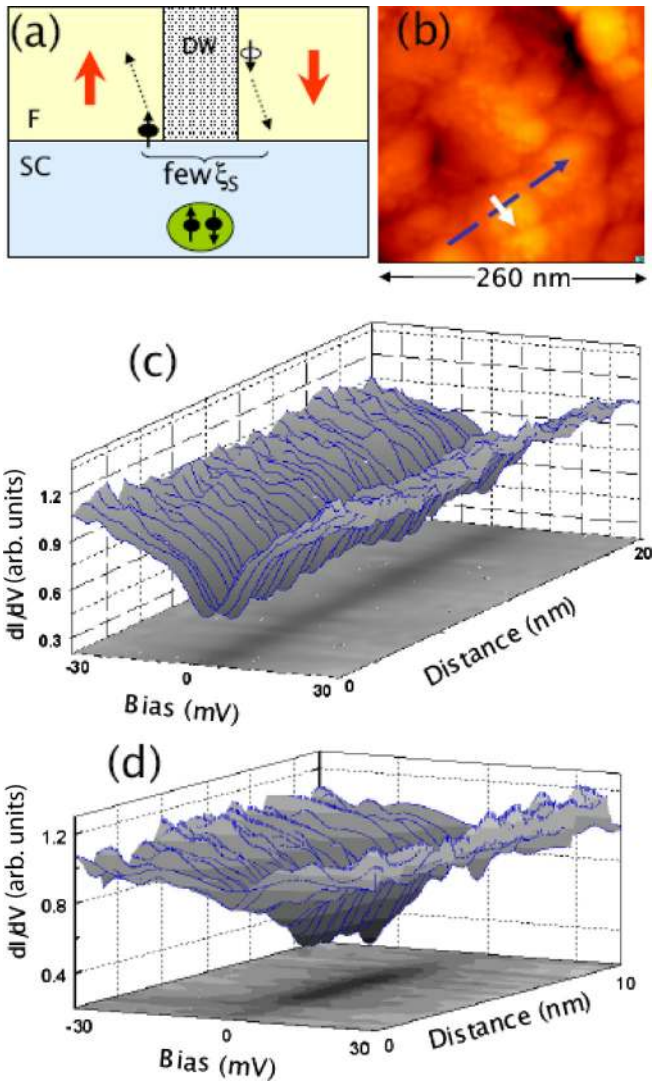

FIG. 29 (color online). STM measurement demonstrating the spatial evolution of the DOS within a "gapped strip" in the $SrRuO_3$. (a) A schematic crossed Andreev reflection diagram. (b) 260×260 nm^2 topographic image of a 18-nm-thick $SrRuO_3/(100)YBCO$ bilayer. (c) Tunneling spectra taken sequentially at fixed steps along the center of the gapped strip [white arrow in (b)]. (d) Tunneling spectra acquired across the gapped strip [white arrow in (b)]. From Asulin *et al.*, 2006.

B. Transport

We now turn to the transport properties of $SrRuO_3$. They are both exciting and challenging.

We first address the high resistivity observed at high temperatures that suggests inapplicability of the Boltzmann theory, and the sharp kink in the resistivity at T_C that suggests

the inapplicability of the Fisher-Langer theory of resistivity near the Curie temperature. On the other hand, the low-temperature resistivity in clean samples seems to exhibit Fermi-liquid behavior. More insight into the rich physics operating here is presented in the next section, where we address the optical properties of $SrRuO_3$.

In addition, we review the anisotropic MR, which is affected by the crystal symmetry, and the extraordinary Hall effect, which has inspired controversy concerning the responsible mechanism.

We end this section by reviewing the transport properties relevant to the spintronics. We address the strong effect of domain walls on the resistivity and the strong effect of current on the domain walls. The latter leads to efficient current-induced domain-wall motion. Both effects are presumably related to the narrowness of the domain walls (3 nm), which can be attributed to the large magnetocrystalline anisotropy, as described in the previous section. As $SrRuO_3$ offers the opportunity to study spintronic effects in the limit of very narrow domain walls, we anticipate a larger role for $SrRuO_3$ in spintronics research.

1. Resistivity

a. Resistivity at $T > T_C$

The high-temperature resistivity in $SrRuO_3$ was first addressed by Allen *et al.* (1996a) who studied single-crystal samples. They noted that the resistivity rises above T_C almost linearly with temperature up to 1000 K (see Fig. 7) and that the extracted mean free path is less than 1 nm above 500 K and therefore the Boltzmann theory should fail. This behavior is not unique: it is reminiscent of the resistivity seen in high-T_c superconductors and also seen in the high-T metallic phase of VO_2 (Allen *et al.*, 1993). Emery and Kivelson (1995) used this feature as the defining property of bad metals. Similar behavior has been observed in thin films of $SrRuO_3$; see Figs. 30(c) and 30(d).

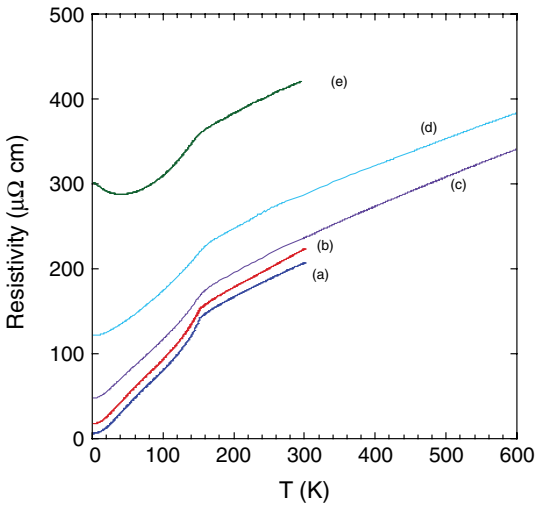

FIG. 30 (color online). Resistivity curves of $SrRuO_3$ films 1000 Å thick: (*a*) and (*b*) are on miscut $SrTiO_3$ substrates and the current is perpendicular to the *c* axis, (*c*) is on a regular $SrTiO_3$ substrate, (*d*) is on a $LaAlO_3$ substrate, and (*e*) is on a ytrria-stabilized zirconia (YSZ) substrate. From Klein, Dodge, Ahn, Reiner *et al.*, 1996.

b. Resistivity near the ferromagnetic phase transitions

The effect of critical spin fluctuations on the resistivity near T_C was first treated by de Gennes and Friedel (1958) who stressed the importance of the diverging spin-spin correlation near T_C and anticipated a concomitant peak in the resistivity. However, this peak was often not observed experimentally, which motivated Fisher and Langer (1968) to revisit the issue. They found that it was the short-range spin correlations that governed the resistivity, leading to an energylike term in ρ_m and critical behavior of $d\rho_m/dT$ above T_C that is identical to that of the specific heat. Subsequent work by Alexander, Helman, and Balberg (1976) concluded that the same critical behavior is also expected below T_C. Experimental tests of these relationships with good metallic ferromagnets (Zumsteg and Parks, 1970; Shacklet, 1974; Simons and Salamon, 1974) seem to confirm both the symmetry around the transition and the correspondence of $d\rho_m/dT$ with the specific heat. This picture implies a weak logarithmic divergence for Heisenberg ferromagnets and a weak power law with an exponent of ~ 0.1 for Ising ferromagnets.

Klein, Dodge, Ahn, Snyder *et al.* (1996) found a different behavior of $d\rho/dT$ near T_C in thin films. They reported

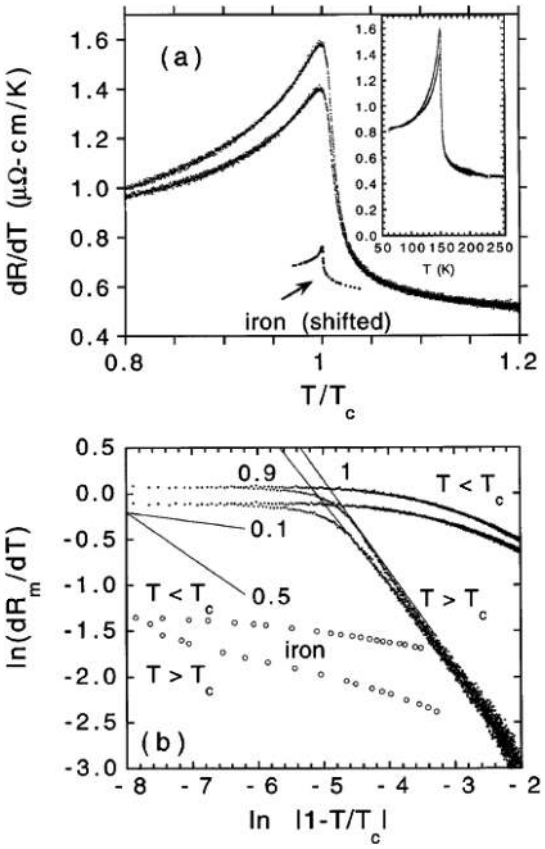

FIG. 31. (a) dR/dT with currents in the [001] and [110] directions; the stronger divergence is in the [110] direction. Iron data are shown for comparison, shifted with a constant of 0.5 $\mu\Omega$ cm. The inset shows a larger temperature range that enables an estimate of the nonmagnetic part in dR/dT. (b) Log-log plot of dR_m/dT with slopes of 0.1 (which is expected), 0.5 (not expected; the Gaussian limit), and iron data for comparison. From Klein, Dodge, Ahn, Snyder *et al.*, 1996.

power-law divergence with an exponent on the order of 1 as $T \rightarrow T_C^+$ and weak divergence as $T \rightarrow T_C^-$ (see Fig. 31). At the same time, they found that the magnetic phase transition itself is normal. They suggested that the striking deviations from the Fisher-Langer behavior may be related to the bad metal behavior exhibited by $SrRuO_3$. Roussev and Millis (2000) showed that the data are consistent with Heisenberg-like critical behavior if one adds a regular term and chooses a different T_C. In their response Klein, Dodge *et al.* (2000) rejected the criticism, arguing that the magnetic critical behavior is Ising-like above and below T_C, consistent with the large uniaxial anisotropy (see Sec. IV.A.2), and that there is no justification for the large regular term and the assumed shift in T_C.

Laad and Muller-Hartmann (2001) proposed that the anomalous transport properties of $SrRuO_3$ could result from the combined effects of orbital degeneracy and on-site Coulomb interactions. They constructed a model that includes these features and showed that it exhibits non-Fermi-liquid behavior consistent with the optical conductivity. We discuss this further in Sec. IV.C.1. Timm, Raikh, and von Oppen (2005) suggested that the critical resistivity anomaly is induced by disorder. Indications for non-Fermi-liquid behavior are also found in the related compound $CaRuO_3$ (Klein *et al.*, 1999), and theoretical work on the orbitally degenerate non-Fermi-liquid state has been extended to $CaRuO_3$ by Laad, Bradaric, and Kusmartsev (2008).

c. Resistivity at $T \ll T_C$

Capogna *et al.* (2002) demonstrated that the temperature dependence of the low-temperature resistivity of high-purity single crystals and thin films is close to quadratic, $\rho = \rho_0 + aT^2$, especially below 15 K. They pointed out that this behavior is sensitive to disorder. Therefore, experimentally the Fermi-liquid behavior at low temperatures is observable only in samples with low residual resistivity. This issue is further discussed in Sec. IV.C.1.

In good metallic ferromagnets a is of order $\sim 10^{-11}$ Ω cm [see, e.g., Volkensh, Dyakina, and Startsev (1973) and Campbell and Fert (1982)] and the T^2 dependence is attributed to electron-electron scattering. Klein, Dodge, Ahn, Snyder *et al.* (1996) showed that for $SrRuO_3$ the change in resistivity below 30 K is 3 orders of magnitude larger. Electron-magnon scattering is also expected to contribute T^2 dependence to resistivity. However, in clean ferromagnetic systems the magnon contribution is usually considered negligible compared to the electron-electron scattering.

The effect of point defects on resistivity was measured upon introducing point defects into the material by electron irradiation. The data show significant negative deviations from Matthiessen's rule, where for a fixed irradiation dose, the induced change in resistivity decreases with increasing temperature. Moreover, at a fixed temperature, the increase in resistivity with irradiation is found to be sublinear (Klein *et al.*, 2001).

Another interesting observation is the resistivity minima reported by Klein, Dodge, Ahn, Reiner *et al.* (1996); see Fig. 30(e) and a series of papers by Herranz and co-workers (Herranz *et al.*, 2003a, 2008; Herranz, F. Sanchez *et al.*, 2004) (see Fig. 32). The resistivity minima in $SrRuO_3$ are correlated with disorder, which may suggest that nonmagnetic disorder localizes the otherwise extended magnetic states. This may also explain the shift of the resistivity minima to higher temperatures as the residual resistivity (which reflects disorder) increases. It is also correlated with film thickness in that it becomes more pronounced in the ultrathin limit.

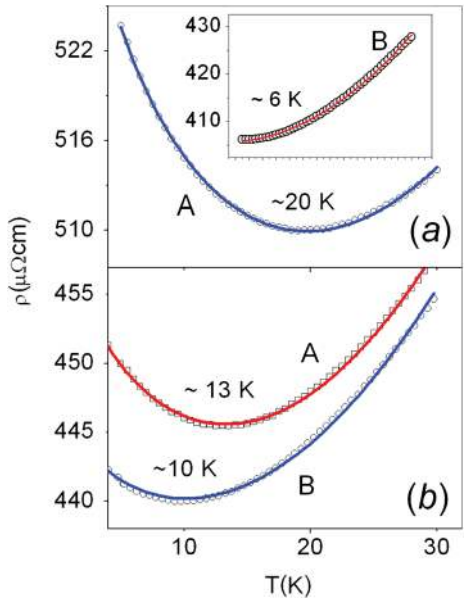

FIG. 32 (color online). Plot of the resistivity against the temperature for (a) two samples cooled down to room temperature at different rates (A, slow; B fast). (b) The two samples were grown on two $SrTiO_3$ substrates having different miscut angles (A, $\alpha = 0°$; B, $\alpha = 2°$). In both panels, fittings to a model described by Herranz, F. Sanchez *et al.* (2004) are plotted, showing excellent agreement with the experimental data. The temperatures at which the minima appear are written next to the corresponding curves. From Herranz, F. Sanchez *et al.*, 2004.

d. Resistivity anisotropy

Because $SrRuO_3$ films are almost cubic, their resistivity of films is quite isotropic, and therefore careful measurements are required to reliably determine the small anisotropy. Genish *et al.* (2007) measured the planar Hall effect in patterned films with current paths along eight different directions in the (110) plane and thereby determined the in-plane anisotropy both above and below T_C. They found that the resistivity is larger by a few percent along the $[1\bar{1}0]$ direction, which is the in-plane projection of the easy axis of the magnetization, and that the onset of magnetization decreases the anisotropy. They concluded that the nonmagnetic and magnetic sources of the anisotropy represent competing effects.

2. Anisotropic magnetoresistance

The anisotropic magnetoresistance (AMR) of a material provides a measure of the dependence of the resistivity on the direction of the magnetization. This phenomenon has been mainly studied in polycrystalline or amorphous materials, where it depends only on the angle between the current and

the magnetization. The study of AMR in epitaxial films of $SrRuO_3$ is more complicated. Crystalline effects are not averaged out, and therefore symmetry allows a dependence also on the angles of the current and the magnetization relative to the crystal axes. In addition, due to the large uniaxial magnetocrystalline anisotropy, monitoring the size and orientation of the magnetization is more complicated (see also Sec. IV.A.2). The AMR effect was studied in the paramagnetic phase by Genish *et al.* (2004) and Shperber *et al.* (2009). By using the EHE and symmetry considerations to determine the size and orientation of the magnetization for fields applied in the (001) plane, both groups found clear evidence for crystal symmetry effects. Large AMR effects were also observed below T_C (Rao, Kacedon, and Eom, 1998).

Ziese, Vrejoiu, and Hesse (2010) measured the AMR as a function of temperature below T_C for fields rotated within different planes and found indications of monoclinic-symmetry AMR.

3. Extraordinary Hall effect

The Hall effect in magnetic materials includes both the ordinary (or regular) Hall effect (OHE) and an extraordinary (or anomalous) Hall effect. The former originates from the Lorentz force and depends on the magnetic induction **B**, whereas the latter depends on the magnetization **M**. Usually, the EHE is attributed to spin-dependent scattering, and the total Hall effect is given by

$$\rho_{xy} = \rho_{xy}^{\mathrm{OHE}} + \rho_{xy}^{\mathrm{EHE}} = R_0 B_z + R_s(\rho)\mu_0 M_z, \tag{2}$$

where R_0 is the ordinary Hall coefficient related to the carrier density n, and R_s is the extraordinary Hall coefficient, which depends on the resistivity ρ as $R_s = a\rho + b\rho^2$, where the linear term is due to a spin-dependent preferred direction in scattering (''skew scattering'') (Smit, 1958), and the quadratic term is due to a lateral displacement involved in the scattering (''side jump'') (Berger, 1970).

Recently, it was suggested that the Berry phase (BP) effect (Berry, 1984) in crystal momentum space (**k** space) can also give rise to an EHE (Jungwirth, Niu, and MacDonald, 2002; Fang *et al.*, 2003; Mathieu *et al.*, 2004; Yao *et al.*, 2004). This is an intrinsic effect, which does not involve scattering, but it depends on the Bloch states and their occupation. In this effect, the EHE is described as

$$\rho_{xy}^{\mathrm{EHE}} = -\rho^2 \sigma_{xy}^{\mathrm{BP}}(M), \tag{3}$$

where the Berry phase transverse conductivity $\sigma_{xy}^{\mathrm{BP}}(M)$ does not depend on ρ, and the dependence of $\sigma_{xy}^{\mathrm{BP}}$ on M should be calculated from the band structure. This mechanism was first invoked to explain the EHE in (III,Mn)V ferromagnetic semiconductors (Jungwirth, Niu, and MacDonald, 2002), and then in $SrRuO_3$ (Fang *et al.*, 2003). Later it was shown that the Berry phase effect in **k** space can be the dominant mechanism even in iron (Yao *et al.*, 2004). Actually such a mechanism for the EHE was suggested by Karplus and Luttinger (Karplus and Luttinger, 1954; Luttinger, 1958) a long time ago, but later disregarded. This effect should be distinguished, however, from the Berry phase effect related to a motion in a topologically nontrivial spin background in *real* space, which has also been proposed as a source of EHE for some materials (Ye *et al.*, 1999; Shindou and Nagaosa, 2001; Taguchi *et al.*, 2001).

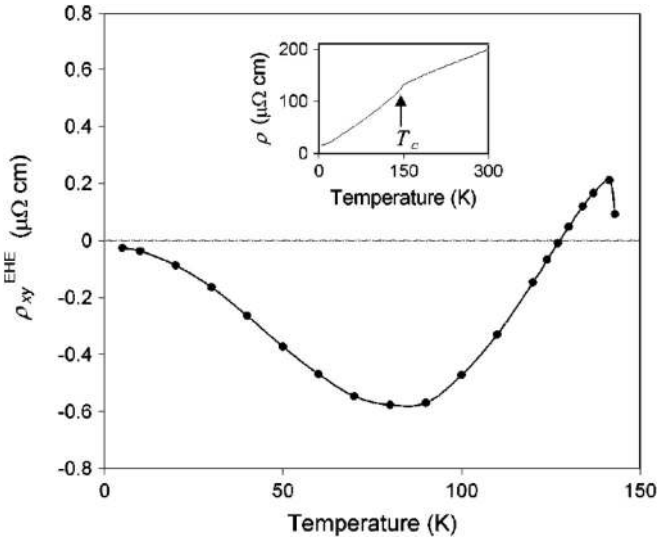

FIG. 33. Extraordinary Hall effect $\rho_{rxy}^{\mathrm{EHE}}$ (due to the spontaneous magnetization) as a function of temperature. The inset shows the longitudinal resistivity ρ as a function of temperature. From Kats *et al.*, 2004.

The EHE in the 4*d* itinerant ferromagnet $SrRuO_3$ exhibits a nonmonotonic temperature dependence, including a change of sign (see Fig. 33) (Izumi *et al.*, 1997; Klein, Reiner *et al.*, 2000), and R_s does not follow the relation $R_s = a\rho + b\rho^2$ (Klein, Reiner *et al.*, 2000).

As mentioned, Fang *et al.* (2003) argued that this behavior can be explained by the Berry phase effect in **k** space, which predicts a peculiar nonmonotonic dependence of $\sigma_{xy}^{\mathrm{BP}}$ on M assuming the exchange gap closes at T_C. They supported their contention with band calculations, which predicted an EHE of a correct order of magnitude and roughly reproduced its temperature dependence. However, band calculations for $SrRuO_3$ are very sensitive to the input parameters (Santi and Jarlborg, 1997; Fang *et al.*, 2003). Therefore, while the calculations support the explanation, they leave open the possibility that in practice the Berry phase effect in $SrRuO_3$ is much smaller, and the EHE is caused by a different mechanism.

Kats *et al.* (2004) tested the Berry phase scenario, which assumes exchange gap closing for $SrRuO_3$ by focusing on the point where the EHE vanishes and asking whether the vanishing occurs at a certain value of M, as one may anticipate for this Berry phase scenario, or at a certain value of ρ, as may be anticipated by the other mechanisms. They concluded that this Berry phase scenario that attributes the temperature dependence to exchange gap closing cannot explain the observed EHE. Recent experiments by Haham *et al.* (2011) show that the EHE scales with resistivity in the entire ferromagnetic phase. They attribute the observed behavior to the contribution of the extrinsic side-jumps mechanism and the intrinsic Berry phase mechanism. For the Berry phase mechanism they assume temperature independent exchange gap [consistent with Dodge *et al.* (1999a)] and they consider the temperature dependence of the scattering rates.

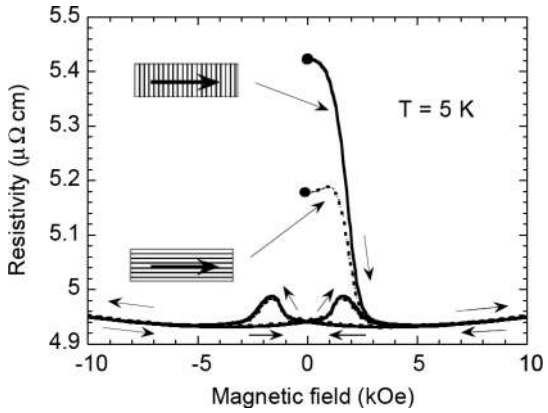

FIG. 34. Hysteresis loops of resistivity vs applied field for current parallel and perpendicular to the domain walls at $T = 5$ K. At the starting point with $H = 0$ (marked by a full circle), the sample is in its domain structure. Increasing the field annihilates the domain wall, and when the field is set back to zero the magnetization of the sample remains saturated. The difference between the initial zero-field resistivity and the subsequent zero-field resistivities is identified as the domain-wall resistivity. From Klein, Kats *et al.*, 2000.

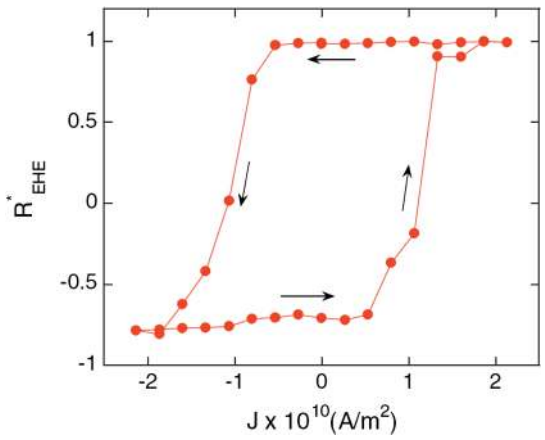

FIG. 35 (color online). Current-induced hysteresis loop with current pulses (100 ms) at $T = 140$ K and $H = 0$ measured with the normalized extraordinary Hall effect (R^*_{EHE}). From Feigenson, Reiner, and Klein, 2007.

4. Domain-wall resistivity

To determine the effect of magnetic domain walls on the resistivity of $SrRuO_3$, Klein, Kats *et al.* (2000) measured the resistivity of a film in the presence and absence of domain walls, thereby permitting extraction of the domain-wall contribution to the resistivity (DWR); see Fig. 34. Based on the study of the domain structure, the orientation and spacing of the domain walls in the sample was known, and the contribution of domain walls to the resistivity could be determined for currents perpendicular and parallel to the domain walls, and later also for intermediate angles (Feigenson *et al.*, 2003).

In the zero-temperature limit, the contribution of domain walls to the resistivity for perpendicular currents is $\rho^{\perp}_{\mathrm{DW}} \sim 0.48\ \mu\Omega$ cm and for parallel currents is $\rho^{\parallel}_{\mathrm{DW}} \sim 0.24\ \mu\Omega$ cm. The width of the domain wall is ~3 nm, while the spacing between the domain walls is ~200 nm. Therefore, in terms of bulk resistivity, the resistivity for the perpendicular current within the domain wall is $\sim 35\ \mu\Omega$ cm and the interface resistance is $\sim 10^{-15}\ \Omega\,\mathrm{m}^2$. This interface resistance is more than 3 orders of magnitude larger than the negative interface resistance of $6 \pm 2 \times 10^{-19}\ \Omega\,\mathrm{m}^2$ reported for cobalt (Ruediger *et al.*, 1998; Kent *et al.*, 1999). The big difference has been attributed to the width of the DW in cobalt, which is estimated to be 5 times larger than in $SrRuO_3$. Because of this thickness, the mechanisms suggested as relevant are those considered for magnetic multilayers by Barnas and Fert (1994): spin accumulation and potential steps. When a polarized current crosses an interface there is spin accumulation near the interface that induces a potential barrier which results in excess resistivity. This effect is relevant only for a perpendicular current. They also found that an interface between a magnetic and a nonmagnetic metal, or between different magnetic domains within a magnetic metal, acts similar to a potential step whose height is related to the exchange splitting. This effect is likely to affect resistivity for any current direction. Klein, Kats *et al.* (2000) found that for $SrRuO_3$ both effects contribute to interface resistance on the order of $10^{-15}\ \Omega\,\mathrm{m}^2$.

Detailed measurements (Feigenson *et al.*, 2003) of the dependence of the domain-wall resistivity on the angle between the current and the domain walls, combined with models developed for transport across magnetic interfaces, enabled the identification of spin accumulation contribution to the resistance and the extraction of spin diffusion length in $SrRuO_3$ as a function of temperature.

5. Current-induced domain-wall motion

The observation of current-induced domain-wall motion in $SrRuO_3$ enabled examination of this intriguing phenomenon in a system with narrow domain walls. Specifically, Feigenson, Reiner, and Klein (2007) demonstrated current-induced domain-wall motion in $SrRuO_3$ by trapping a single-domain wall in a submicrometer pattern and then following changes in its position by monitoring the EHE (see Fig. 35 for current-driven hysteresis loops).

The most interesting result of these measurements was the finding that the efficiency of current-induced domain-wall

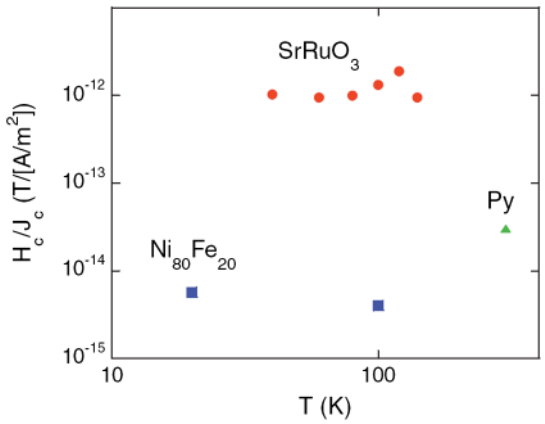

FIG. 36 (color online). H_c/J_c as a function of temperature in $SrRuO_3$ (circles), permalloy (Py, triangle), and $Ni_{80}Fe_{20}$ (squares). From Feigenson, Reiner, and Klein, 2007.

motion (defined as H_c/J_c, where H_c is the coercivity field and J_c is the depinning current), is orders of magnitude larger than the efficiency in magnetic $3d$ alloys (see Fig. 36). The difference was attributed to the narrowness of the domain walls in $SrRuO_3$. These results were further discussed by Tatara, Kohno, and Shibata (2008), who found them consistent with their prediction in the thin-wall limit.

The unique interplay between current and magnetic structure in $SrRuO_3$ is also manifest in the report of current-induced magnetic instability in single-layer structures (Feigenson, Reiner, and Klein, 2008), which is qualitatively and quantitatively distinct from current-induced domain-wall motion.

C. Optical properties

The electromagnetic response of $SrRuO_3$ has proved to be a fascinating subject. There are many interesting elements. We begin in Sec. IV.C.1 by describing the anomalous infrared response, which bears a similarity to cuprate superconductors and has attracted significant theoretical interest. Later, in the same section, we discuss Raman measurements of optical phonons. We discuss optical interband transitions in Sec. IV.C.2, and show that these are in good agreement with density functional calculations. The lack of strong temperature dependence in the interband transitions provides evidence for relatively localized moments that do not change significantly as the temperature is raised above the Curie point. In Sec. IV.C.3, we describe the magneto-optic response associated with both interband and intraband transitions; the latter is related to the extraordinary Hall effect discussed in Sec. IV.B.3. In Sec. IV.C.4, we describe the time-resolved optical effects, notably time-domain ferromagnetic resonance.

1. Infrared and Raman response

$SrRuO_3$, the cuprate superconductors, and many other transition metal oxides exhibit carrier dynamics that are not well described by a simple Drude model (Basov and Timusk, 2005; Dordevic and Basov, 2006). Bozovic *et al.* (1994) noted that $Ca_{0.5}Sr_{0.5}RuO_3$, $La_{0.5}Sr_{0.5}CoO_3$, and the cuprate superconductors all show two unusual features in common: infrared reflectance that falls quasilinearly with frequency and a broad, frequency-independent electronic Raman spectrum. Both of these features are associated with midinfrared conductivity in excess of that given by the conventional Drude model for metals. Subsequent work has shown the midinfrared conductivity band to be a generic feature of ruthenium oxides (Puchkov *et al.*, 1998; Lee *et al.*, 2001, 2002), including $SrRuO_3$ (Kostic *et al.*, 1998a).

Kostic *et al.* (1998a) measured the infrared reflectance of thin $SrRuO_3$ films deposited on $SrTiO_3$ substrates, as shown in Fig. 37(a). They found that at low temperatures the midinfrared conductivity evolves smoothly into a sharp peak at zero frequency, yielding an overall conductivity that followed a power-law form $\sigma_1(\omega) \propto 1/\sqrt{\omega}$. With increasing temperature the conductivity near zero frequency decreases, until near the ferromagnetic $T_C \approx 150$ K where the spectrum develops a local minimum at $\omega = 0$ and a peak at

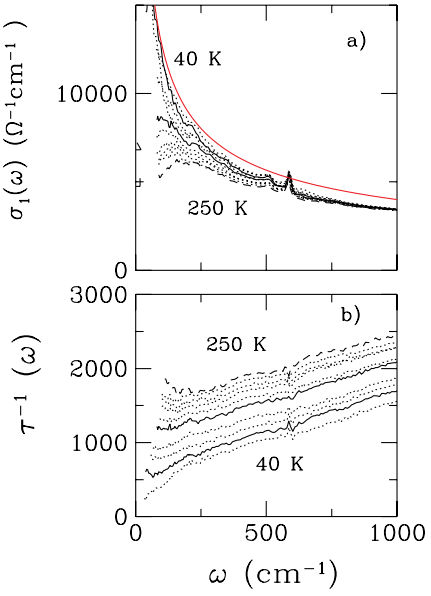

FIG. 37 (color online). (a) Optical conductivity of $SrRuO_3$ at $T =$ 40, 80 (solid curve), 105, 125, 145 (solid curve), 165, 185, 205, 225, and 250 K (dashed curve). Transport measurements at $\omega = 0$ are also shown for $T = 145$ (△) and 250 K (+), and the top curve is given by $\sigma_1(\omega) = c/\sqrt{\omega}$ with $c = 1.265 \times 10^5\ \Omega^{-1}\,\mathrm{cm}^{-1/2}$. (b) Frequency-dependent scattering rate $1/\tau(\omega)$ evaluated with Eq. (4), for the same temperatures. From Kostic *et al.*, 1998b.

$\hbar\omega \approx 3k_BT$. Similar behavior is exhibited by $SrRuO_3$ (Lee *et al.*, 2002).

Figure 37(b) shows the frequency-dependent scattering rate, obtained from the complex conductivity in a single-band model via the transformation

$$\frac{1}{\tau(\omega)} = \epsilon_0\omega_p^2 \mathrm{Re}\left\{\frac{1}{\sigma(\omega)}\right\}, \tag{4}$$

where ω_p is the carrier plasma frequency. At $T = 40$ K $1/\tau(\omega) \propto \sqrt{\omega}$, and from 250 to 1000 cm^{-1} the scattering rate is approximately linear with constant slope and an intercept that increases with temperature.

Dodge *et al.* (2000) provided a more detailed study of the carrier dynamics in the regime $\omega < 100$ cm^{-1} and $T <$ 100 K. To improve precision and accuracy over infrared reflectance spectroscopy, they used both time-domain terahertz and infrared spectroscopies in transmission geometry. For these studies miscut $NdGaO_3$ substrates were used, which are transparent in the far infrared. They showed that the power-law frequency dependence observed by Kostic *et al.* (1998a) crossed over to a dc limit in remarkable agreement with the empirical form (Ioffe and Millis, 1998; van der Marel, 1999)

$$\sigma(\omega, T) = \frac{A}{[1/\tau(T) - i\omega]^\alpha}, \tag{5}$$

with $\alpha \approx 0.4$. Although the nonanalytic behavior of Eq. (5) for $\alpha = 0.4$ is not expected of a Fermi liquid, the resulting values for $\tau(T)$ follow a Fermi-liquid form

$$\frac{\hbar}{\tau(T)} = \frac{\hbar}{\tau_0} + \frac{k_BT^2}{T_0}, \tag{6}$$

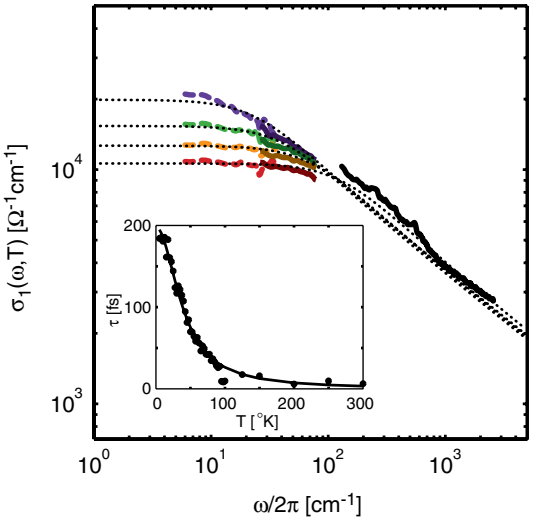

FIG. 38 (color online). Dynamical conductivity of $SrRuO_3$ at $T =$ 8, 40, 60, and 80 K. Dashed lines extending over 6–36 cm^{-1} show terahertz measurements and solid lines extending over 26–80 cm^{-1} show infrared measurements performed on the same sample, a $SrRuO_3$ film on an $NdGaO_3$ substrate. The solid line extending over 124–2440 cm^{-1} shows the results of Kostic *et al.* (1998a) with a 420 nm $SrRuO_3$ film deposited on $SrTiO_3$. Thin dotted lines show fits of Eq. (5) to the complex conductivity obtained from terahertz spectroscopy. The inset shows $1/\tau(T)$, together with a fit to Eq. (6). From Dodge *et al.*, 2000.

with $\tau_0 = 198$ fs and $T_0 = 40$ K. These results are shown in Fig. 38. $CaRuO_3$ exhibits similar behavior, with $\alpha = 0.5$, $\tau_0 = 550$ fs, and $T_0 = 53$ K (Kamal *et al.*, 2006).

Subsequent work by Capogna *et al.* (2002) showed that the description given by Eqs. (5) and (6) must break down in the $\omega = 0$, $T = 0$ limit of clean samples. They measured the temperature dependence of the dc resistivity in a large number of thin films and single crystals of $SrRuO_3$ and found them to be inconsistent with the dc extrapolation of Eqs. (5) and (6) when the residual resistivity was less than 8 $\mu\Omega$ cm. This is also the disorder scale below which $SrRuO_3$ exhibits quantum oscillations that have the temperature dependence expected of a Fermi liquid (Mackenzie *et al.*, 1998). Kats and Klein (2002) also found Eqs. (5) and (6) to be inconsistent with the resistivity changes induced in clean samples by electron irradiation. It remains unclear how the optical properties, critical resistivity, and high-temperature resistivity emerge from the apparently Fermi-liquid ground state that exists at low temperatures in samples with low disorder.

The samples studied by terahertz spectroscopy had residual resistivities near 40 $\mu\Omega$ cm, an order of magnitude larger than that required for these discrepancies to become apparent. Unfortunately, neither single crystals nor films deposited on $SrTiO_3$ are suitable for infrared transmission, so further investigation of the terahertz conductivity at lower levels of disorder will require improvements in sample preparation. The temperature independence of $\sigma(\omega)$ for $\omega \gtrsim 100$ cm^{-1} suggests that the influence of disorder is limited to very low frequencies, involving a small fraction of the overall conductivity spectral weight. Consequently, we expect the qualitative features described here to remain valid away from very low temperatures and frequencies with the cleanest samples. While this is not the regime most relevant for Fermi-liquid theory, it is nonetheless clear that it displays a robust phenomenology that demands explanation, including the anomalous critical transport near T_C and the lack of resistivity saturation above T_C (Allen *et al.*, 1996b; Klein, Dodge, Ahn, Reiner *et al.*, 1996; Klein, Dodge, Ahn, Snyder *et al.*, 1996; Klein, Dodge *et al.*, 2000; Roussev and Millis, 2000).

Several explanations for the conductivity in $SrRuO_3$ have been advanced. In single-electron band theory, $SrRuO_3$ possesses three bands that cross the Fermi level; each of these is spin split by the ferromagnetism, and transitions between spin-up and spin-down bands can occur at low energies because of the strong spin-orbit interaction. This could provide a mechanism for midinfrared conductivity, but it does not explain the peculiar dependence on frequency and temperature, nor can it explain the increase in spectral weight at low frequencies as the temperature is reduced.

Near some quantum phase transitions, the conductivity is expected to exhibit power laws in the frequency and temperature dependence (Sachdev, 1999), and this has been proposed to explain the conductivity in optimally doped cuprates (van der Marel *et al.*, 2003). Werner *et al.* (2008) argued that a multiband metal should exhibit a quantum phase transition as a function of local electron interactions, between a paramagnetic metal and an incoherent metal with frozen local moments. They proposed that the quantum critical regime of this transition should be broad enough that it could explain the power-law conductivity in $SrRuO_3$ and $CaRuO_3$.

Laad and Muller-Hartmann (2001) argued that the power-law conductivity is associated with an x-ray edge singularity as electrons hop between orbitals with different orientations in the presence of on-site interactions. In their model, the small orthorhombic distortion sets a low-energy coherence scale that cuts off the singularity and restores Fermi-liquid behavior at low temperatures and frequencies, consistent with the observations described here and in Sec. IV.B.1. Subsequent work has shown that the magnetotransport properties of $CaRuO_3$ are consistent with this model, as is the electronic Raman spectrum of $SrRuO_3$ (Laad, Bradaric, and Kusmartsev, 2008).

Ioffe and Millis (1998) suggested that the conductivity of the cuprates could be explained in a model with strong scattering rate anisotropy. Their model was for a two-dimensional metal, but it could be extended to the three-dimensional case appropriate to $SrRuO_3$. Currently there is no direct evidence that the scattering rate anisotropy in $SrRuO_3$ is as strong as it would need to be to produce the observed conductivity.

At low frequencies, the optical spectral weight increases significantly with decreasing temperature. Kamal *et al.* (2006) examined this effect in three different ruthenium compounds and noticed an interesting correlation between the spectral weight gain and the tendency toward ferromagnetism. Among $SrRuO_3$, $CaRuO_3$, and hexagonal $BaRuO_3$, ferromagnetic $SrRuO_3$ exhibits the largest change in spectral weight, while the weak paramagnet $BaRuO_3$ exhibits the smallest change, with nearly ferromagnetic $CaRuO_3$ intermediate between the two. Optical spectral weight can be

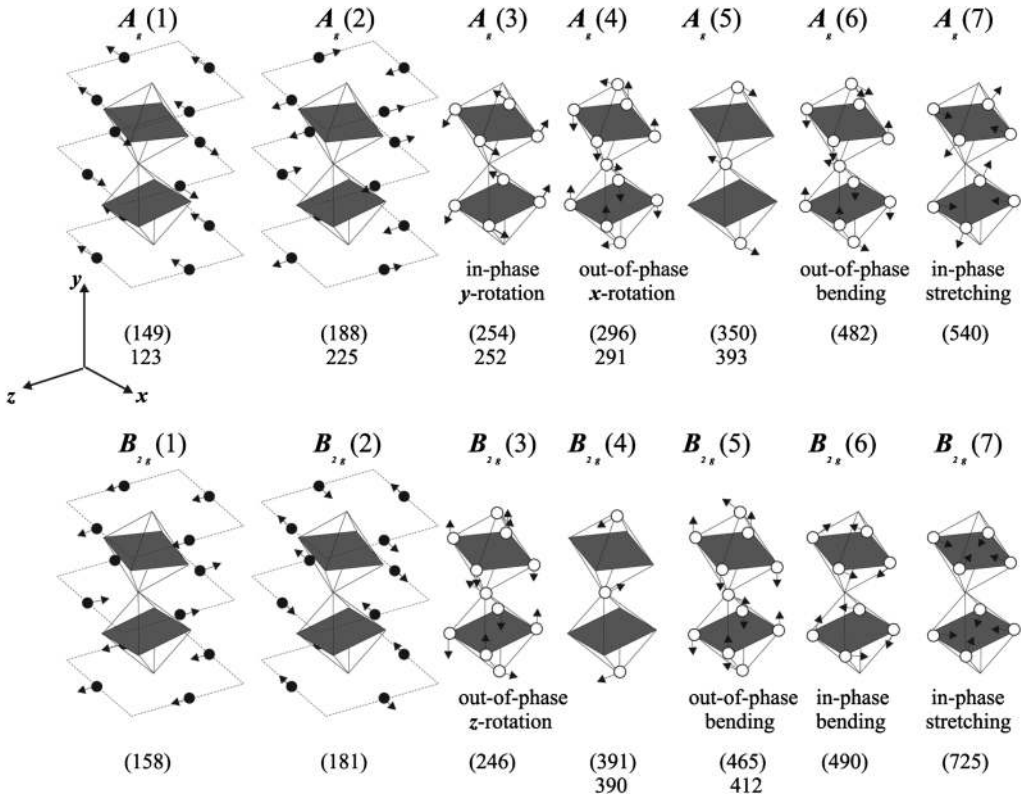

FIG. 39. Atomic motions for the 14 A_g and B_{2g} Raman-active phonon modes. Phonon frequencies obtained from lattice dynamical calculations are listed in parentheses below the associated mode; Raman line assignments are listed below these. All frequencies are given in wave numbers. From Iliev *et al.*, 1999.

associated with carrier kinetic energy, so this observation provides evidence for the basic picture of itinerant ferromagnetism being driven by a competition between kinetic and potential energy.

Recent work on the cuprates indicates that the electron-phonon interaction is essential to understanding many of their physical properties, including their optical conductivity (Mishchenko and Nagaosa, 2004; Rosch *et al.*, 2005; Gunnarsson and Roesch, 2008; Mishchenko *et al.*, 2008; Mishchenko, 2010). Changes in the chemical bond angles are enough to make $CaRuO_3$ paramagnetic (Mazin and Singh, 1997b), so it is reasonable to expect that phonons play a significant role in modulating magnetic interactions in $SrRuO_3$, and perhaps also to the infrared conductivity. The importance of electron-phonon interaction to the properties of ruthenates is relatively unexplored and promises to be an interesting avenue for future research.

The Raman spectrum of $SrRuO_3$ reveals seven phonon lines that have been studied as a function of temperature (Kirillov *et al.*, 1995; Iliev *et al.*, 1999). Figure 39 shows the atomic motions of the 14 predicted Raman-active A_g and B_{2g} modes (Iliev *et al.*, 1999). The calculated frequency is given in parentheses below each mode diagram in wave numbers, and the observed frequency is given below that in cases where an assignment is possible.

The lines assigned to $A_g(2)$, $A_g(3)$, $B_{2g}(4)$, and $B_{2g}(5)$ all exhibit anomalous frequency shifts as the temperature is lowered below the ferromagnetic transition, indicating an important role for electron-phonon interactions (Iliev *et al.*, 1999).

The high conductivity of $SrRuO_3$ screens the charge of the infrared-active phonons, making them difficult to observe. Five of the possible 25 infrared-active phonon modes have been observed in samples that have had their conductivity suppressed through intentional ruthenium deficiency or substitution with manganese (Crandles *et al.*, 2008a, 2008b).

2. Optical interband transitions

The optical conductivity spectra of four ruthenium oxide compounds show qualitatively similar interband features, as shown in Fig. 40 (Lee *et al.*, 2001). The spectrum of $SrRuO_3$ shown in Fig. 40(b) reveals three clear peaks that are labeled according to the schematic energy level diagram in Fig. 41: Peak A near 3 eV corresponds to transitions that have primarily $O(2p) \rightarrow Ru(4d, t_{2g})$ character; peak B near 6 eV corresponds to transitions that have primarily $O(2p) \rightarrow Ru(4d, e_g)$ character; and peak C near 10 eV corresponds to transitions that have primarily $O(2p) \rightarrow Sr(4d)$ character. From the energy difference between peaks A and B, the ligand field splitting can be estimated to be $10Dq \approx 3$ eV (Lee *et al.*, 2001, 2003).

These energy scales are all consistent with estimates from band structure calculations in the local density approximation (LDA) (Allen *et al.*, 1996b; Singh, 1996a; Mazin and Singh, 1997a). Figure 42 shows the measured optical conductivity together with an LDA calculation over the same energy range (Dodge *et al.*, 1999b). The comparison demonstrates that the energy scales are in quantitative agreement, while

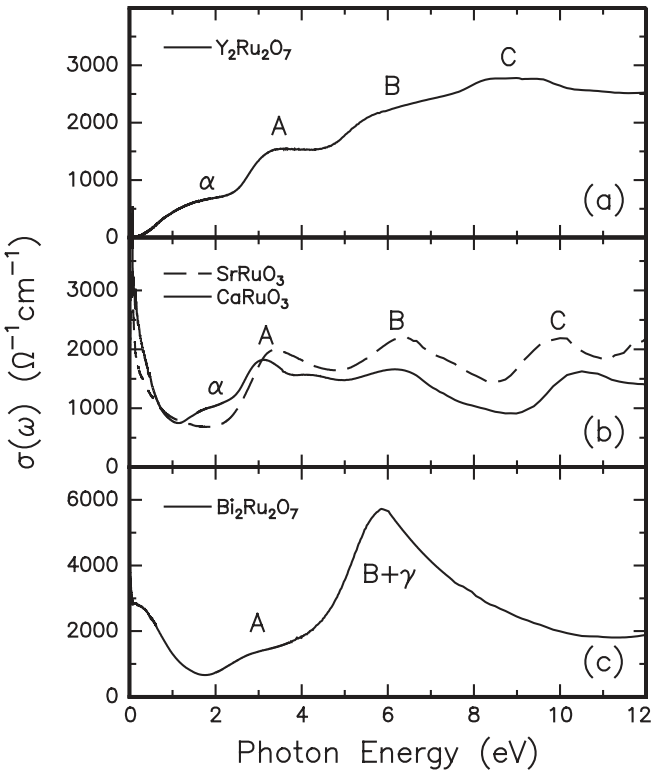

FIG. 40. Room-temperature optical conductivity of (a) $Y_2Ru_2O_7$, (b) $CaRuO_3$ and $SrRuO_3$, and (c) $Bi_2Ru_2O_7$. Peak labels correspond to interband transitions shown schematically in Fig. 41. From Lee *et al.*, 2001.

the magnitude of the optical matrix elements are correct to about a factor of 2. The agreement with LDA calculations was confirmed for both $SrRuO_3$ and $CaRuO_3$ by Mazin and Singh (1997a), who argued further that correlations beyond those included in the LDA were weak. However, LDA + U calculations with $U = 2.5$ eV do not appear to produce significant changes in the optical transition energies (Wang *et al.*, 2009). To place a bound on the strength of interactions beyond the LDA, it would be useful to vary the strength of the added interaction and determine the value at which the calculation disagrees measurably from experiment.

LDA calculations indicated that the local ferromagnetic exchange splitting should be strongly dependent on temperature in $SrRuO_3$, and that the local magnetization should

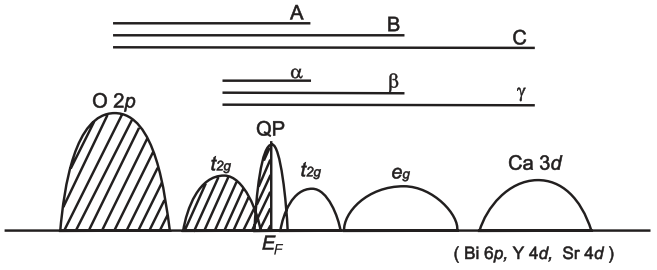

FIG. 41. Generic electronic structure for $Y_2Ru_2O_7$, $CaRuO_3$, $SrRuO_3$, and $Bi_2Ru_2O_7$, shown together with optical transitions assigned in Fig. 40. The specific case of $CaRuO_3$ is shown, although qualitatively similar behavior is expected for the other compounds. From Lee *et al.*, 2001.

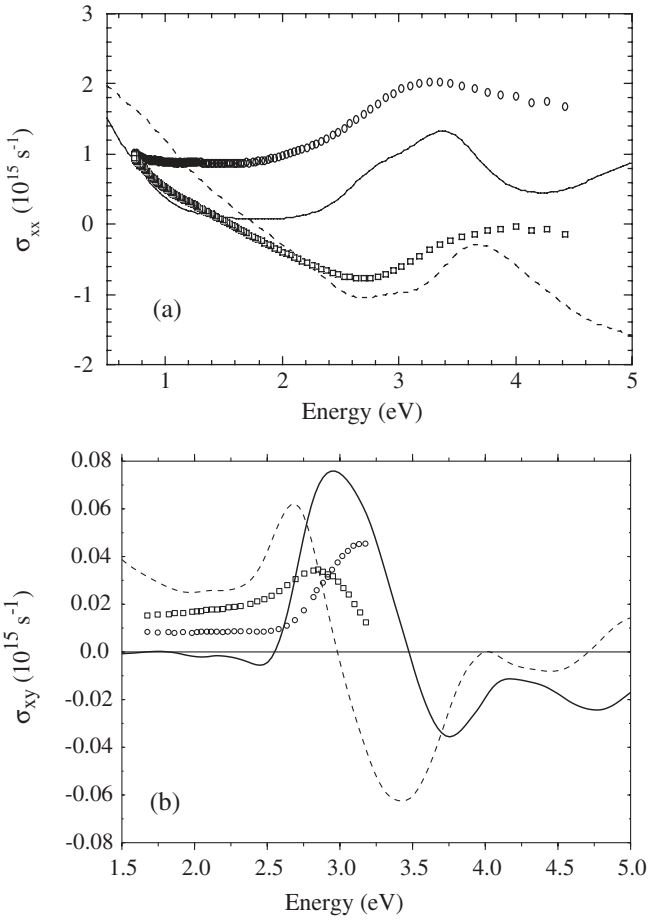

FIG. 42. (a) Optical conductivity $\sigma_{xx}(\omega)$ and (b) magneto-optic conductivity $\sigma_{xy}(\omega)$. Experimental measurements are shown as discrete markers, ○ for σ_{1xx} and σ_{2xy}, and □ for σ_{2xx} and σ_{1xy}; theoretical calculations in the local density approximation are shown as solid lines for σ_{1xx} and σ_{2xy}, and dashed lines for σ_{2xx} and σ_{1xy}. Experimental values for σ_{xx} were taken at room temperature, while those for σ_{xy} were taken at $T = 65$ K and scaled up using the known $M(T)$ to the value expected at $T = 0$. From Dodge *et al.*, 1999b.

disappear above T_C (Mazin and Singh, 1997b). However, the optical spectrum exhibits relatively little temperature dependence at these frequencies, indicating that the local ferromagnetic exchange splitting remains robust above T_C (Dodge *et al.*, 1999a).

3. Magneto-optical response

The strong spin-orbit interaction in ruthenium produces large magneto-optic effects in $SrRuO_3$ (Klein *et al.*, 1995b; Herranz *et al.*, 2005). Beyond its intrinsic interest, this magneto-optic activity has been useful for imaging magnetic domains (Klein *et al.*, 1995b) and sensing the magnetization of ultrathin films (Xia *et al.*, 2009). The lower panel of Fig. 42 shows the off-diagonal part of the optical conductivity $\sigma_{xy}(\omega)$, which is responsible for magneto-optical effects such as Faraday and Kerr rotation (Dodge *et al.*, 1999b). The peak in $\sigma_{2xy}(\omega)$ near 3 eV is associated with interband transitions to states with Ru($4d$, t_{2g}) character. The calculation yields a qualitatively different spectrum for the cubic structure, so the

agreement indicates that the orthorhombic structure is accurately reflected in the calculated wave functions (Solovyev, 1998).

In the infrared, magneto-optical effects result from intraband transitions and are associated with the EHE. Measurements and calculations indicate a peak feature near 100 meV, approximately the spin-orbit interaction energy (Fang *et al.*, 2003). Kim *et al.* (2007) resolved this resonance more completely by extending the spectral range to below 200 meV. As discussed in Sec. IV.B.3, the nonmonotonic temperature dependence of the EHE and associated peak feature was interpreted in terms of a Berry phase contribution to the extraordinary Hall effect.

4. Time-resolved optical effects

Pulsed lasers can be used to both manipulate and probe transition metal oxides on femtosecond time scales (Averitt and Taylor, 2002). Ogasawara *et al.* (2005) studied the ultrafast changes in the magneto-optic Kerr effect in several magnetic materials, including $SrRuO_3$. They found that each material exhibited the same behavioral sequence in response to irradiation by an intense femtosecond laser pulse. In the first 200 fs, the laser heats the electrons to cause a reflectivity change and in the Kerr effect. This heat is then transferred to the magnetic system in a few picoseconds, leaving a steplike change in the Kerr effect that initially oscillates around a quasiequilibrium value. The oscillations are associated with magnetization precession that occurs because of changes in the anisotropy field resulting from the laser heating. At longer times, the spin system thermalizes, damping the oscillations and producing a maximum change in the Kerr effect at about 0.5 ps. Subsequently, the heat generated by the pulse is dissipated into the substrate, and the system returns to its equilibrium state after about 10 ns. Figure 43(a) shows the ferromagnetic resonance oscillations in $SrRuO_3$ as a function of the external magnetic field, together with the associated Fourier spectra in Fig. 43(b). The magnetic anisotropy is then inferred to be $h_A = 7.2$ T (for $g = 2$), with the easy axis oriented at 30° to the film normal at $T = 5$ K. As described in Sec. IV.A.2, this orientation is identical to the static magnetization measurements, and the magnitude is within a factor of 2 of the value inferred from magnetization reversal. We expect the anisotropy field value obtained from the time-resolved magneto-optical Kerr effect to be the more reliable measurement, because it involves coherent magnetic precession at small angles θ with respect to the anisotropy axis, making the theoretical interpretation more straightforward. In contrast, magnetization reversal typically involves incoherent magnetization rotation, and the anisotropy energy is likely to deviate at large θ from the assumed form $E_{\text{anis}} = K\sin^2\theta$.

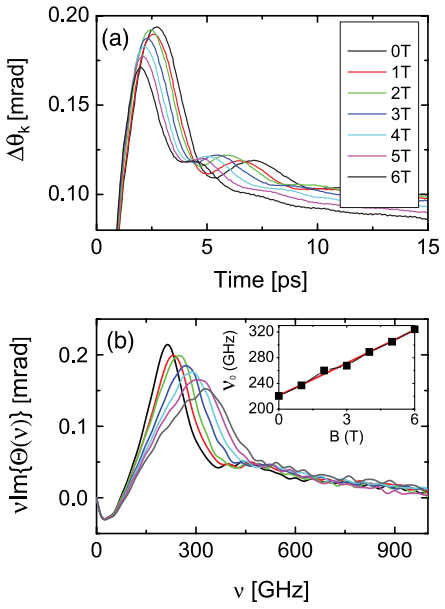

FIG. 43 (color online). Time-resolved magneto-optical measurements of ferromagnetic resonance in $SrRuO_3$ at $T = 5$ K. (a) Change in the magneto-optic Kerr rotation angle $\Delta\theta_K$ as a function of time delay following pulsed excitation with a femtosecond laser, and for several values of applied magnetic field. (b) Fourier transforms of the time traces shown in (a); the inset shows the ferromagnetic resonance frequency as a function of applied magnetic field. From Langner *et al.*, 2009.

Photoexcitation can induce strain in $SrRuO_3$ on a time scale of 500 fs (Schmising *et al.*, 2008). Optical absorption initially heats the electrons, and these give up their energy to phonons to produce the strain field. At $T > T_C$ the strain is generated through direct electron-phonon interaction, but at $T < T_C$ the electronic relaxation depletes the magnetization, and this in turn couples to phonons through the magnetostrictive interaction. This effect has been utilized in heterostructures with $SrRuO_3$ to induce large pulses of uniaxial stress on materials sandwiched between $SrRuO_3$ layers (Schmising *et al.*, 2006, 2007a, 2007c).

D. Photoemission and electronic structure

The degree of correlation in $SrRuO_3$ and its doped variants (mostly Ca and Ti on the Sr and Ru sites, respectively) has been a primary issue in the discussion of photoemission in these materials for over a decade. Since the Ru 4*d* orbitals tend to be more spread out than typical 3*d* orbitals, the degree of correlation is expected to be less. In core-level photoemission spectra, screened and unscreened features in the Ru 3*d* doublet, and their respective spectral weight, are possible indicators for the degree of correlation. In valence-band spectra, a spectral weight shift to incoherent features can point to correlation effects.

1. Surface preparation

As discussed, it is mainly the oxygen activity during synthesis that determines the stoichiometry of a $SrRuO_3$ film and thereby its electronic and magnetic properties. Indeed, oxygen activity along with strain and initial growth (termination) form a primary trio of factors that govern the intrinsic properties of $SrRuO_3$ thin films. It follows therefore that photoemission should yield results compatible with the picture painted by optical and transport measurements and reveal the effects of each of these three factors. However, since photoemission is a surface-sensitive technique and probes only a few monolayers deep into the material, one has to be concerned about how the surface was prepared. For bulk samples, to our knowledge, only scraping of the surface has been employed, together with oxygen annealing. For films,

samples are either introduced into the analysis chamber from outside the vacuum (*ex situ*), and subsequently *cleaned* by common annealing techniques, or grown in vacuum and transferred into an adjacent analysis chamber without breaking the vacuum (*in situ*). It is clear that the most reliable data would be obtained from the *in situ* case.

2. Core-level photoemission

Before discussing photoemission experiments on thin films, we briefly examine photoemission results on ruthenium oxides more generally. H. D. Kim *et al.* (2004) showed using core-level photoemission spectroscopy (PES) how the degree of correlation varies systematically in the ruthenate family of complex oxides as a whole. The properties of these oxides range from good metals (RuO_2) to insulators ($Y_2Ru_2O_7$). They suggest that this change in electronic behavior can be attributed to a change in electron-electron correlation. They come to this conclusion based on fits of experimental core-level photoemission spectra [x-ray photoemission spectroscopy (XPS) (Cox *et al.*, 1983)] using dynamic mean-field theory (DMFT) (Georges *et al.*, 1996). The 3*d* peaks of ruthenium are compared for ruthenates ordered by their degree of metallicity, and a systematic relative shift in spectral weight from the so-called screened peak to the unscreened peak is observed, as shown in Fig. 44. To explain these shifts, H. D. Kim *et al.* (2004) used a model in which the fitting parameters are the Hubbard U and the bandwidth W of the ruthenium 4*d* band. The outcome of their analysis, given in Table III, is that the ratio U/W correlates with the ratio of the screened and unscreened peaks, from which one can deduce that the stronger the screened peak the less correlation there is (i.e., the more metallic).

Both $SrRuO_3$ and $CaRuO_3$ can be classified by their XPS and ultraviolet photoemission spectroscopy (UPS) spectra in this way, despite having, for example, similar transport properties at room temperature. Based on the classification by XPS spectra $CaRuO_3$ would be a more correlated system than $SrRuO_3$. However, the samples studied by H. D. Kim *et al.* (2004) could have suffered from the same off stoichiometry as discussed earlier (in Sec. III.E.1) (for instance, due to the surface or sample preparation processes).

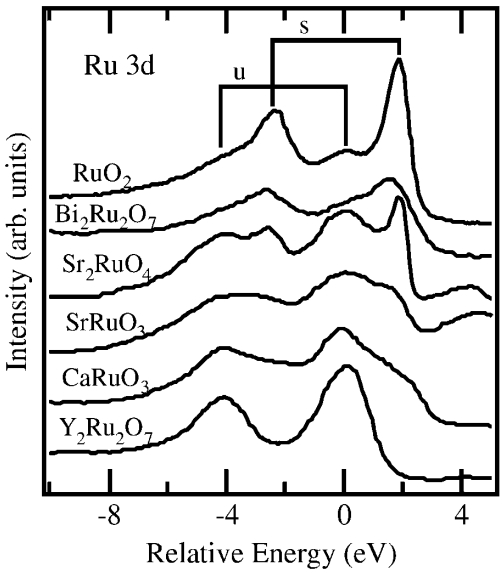

FIG. 44. Ru 3*d* XPS spectra of RuO_2, $Bi_2Ru_2O_7$, Sr_2RuO_4, $SrRuO_3$, $CaRuO_3$, and $Y_2Ru_2O_7$. *s* and *u* denote screened and unscreened peaks, respectively. All the spectra are aligned by the unscreened-peak positions of Ru $3d_{(5/2)}$. From H. D. Kim *et al.*, 2004.

TABLE III. Parameter values (in eV) obtained from fitting Ru 3*d* spectra of ruthenates. From H. D. Kim *et al.*, 2004.

x in $Y_{2-x}Bi_xRu_2O_7$	U	W	Ru compound	U	W
0.0	1.7	1.2	$CaRuO_3$	2.7	2.6
0.4	1.7	2.1	$SrRuO_3$	2.15	2.6
1.0	1.7	2.15	Sr_2RuO_4	2.15	2.8
1.6	1.7	2.9	RuO_2	1.8	3.6
2.0	1.7	2.7			

Comparing the results above with spectra of $Ca_{1-x}Sr_xRuO_3$ thin films obtained by Takizawa *et al.* (2005), as seen in Fig. 45, the evolution of the screened and unscreened peak as a function of Ca content can be seen. Assuming no off-stoichiometry, in the scheme of H. D. Kim *et al.* (2004), the lowering of the screened peak in $CaRuO_3$ could be interpreted as an increase in correlation compared to $SrRuO_3$.

3. Valence-band photoemission

In UPS spectra, another shift in spectral weight is observed. In this case, the t_2g peak, which is close to the Fermi level and referred to as the coherent peak (i.e., the quasiparticle band near E_F), is reduced as correlation increases, and a broad peak around 1.5 eV starts to rise. This latter peak is called the incoherent peak (i.e., the remnant of the Hubbard bands 1–2 eV above and below E_F). Whether the spectral weight measured is a surface feature or truly a feature of correlation can more or less be resolved by correcting more bulk-sensitive Al-$K\alpha$ spectra with surface-sensitive He I spectra, the latter is subtracted from the former after appropriate resolution broadening (Maiti and Singh, 2005). This

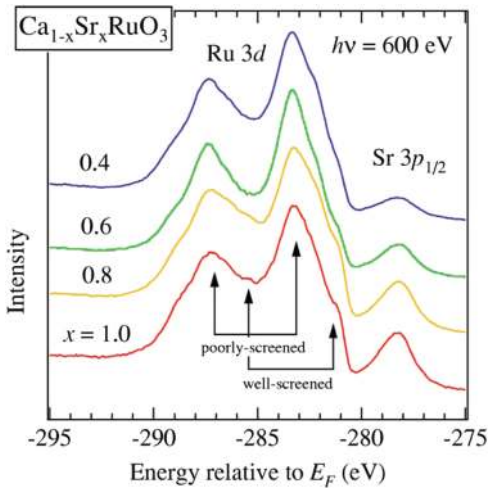

FIG. 45 (color online). Ru 3*d* and Sr 3*p* core-level photoemission spectra of $Ca_{1-x}Sr_xRuO_3$. From Takizawa *et al.*, 2005.

technique works well because the Ru t_{2g} band is well separated from the O $2p$ band in case of the UPS spectra. It is noteworthy here that a clear t_{2g} peak at the Fermi level has not yet been observed with scraped bulk samples (Cox *et al.*, 1983; Fujioka *et al.*, 1997; Okamoto *et al.*, 1999; Rao *et al.*, 2001; Maiti and Singh, 2005; Maiti, Singh, and Medicherla, 2007a) or cleaned *ex situ* thin film samples (Park *et al.*, 2004). As pointed out by Kim, Chung, and Oh (2005), *in situ* prepared thin film specimens may provide the best opportunity for investigating the intrinsic electronic structure of $SrRuO_3$ with photoemission spectroscopy.

In an attempt to be more quantitative, the spectra can be compared with DOS calculations (Allen *et al.*, 1996a; Fujioka *et al.*, 1997; Okamoto *et al.*, 1999; Rao *et al.*, 2001; Vidya *et al.*, 2004; Maiti and Singh, 2005). A representative calculation and a measurement on a scraped bulk sample are shown in Fig. 46.

The calculations show a t_{2g} peak with almost the same height as the O $2p$ peak. The discrepancy with the measured data can be considered in terms of a self-energy correction to the one-electron band structure (Inoue *et al.*, 1996a, 1996b; Fujioka *et al.*, 1997; Imada, Fujimori, and Tokura, 1998; Okamoto *et al.*, 1999; Kim, Chung, and Oh, 2005). Because of the k dependence of the self-energy the spectral weight at the Fermi level is reduced by a factor m_k/m_b, where m_k is called the k mass and m_b is the bare band mass. Combining these values with the mass enhancement factor m^*/m_b as derived from the electronic specific heat γ, one obtains the quasiparticle weight $Z = (m_k/m_b)/(m^*/m_b)$.

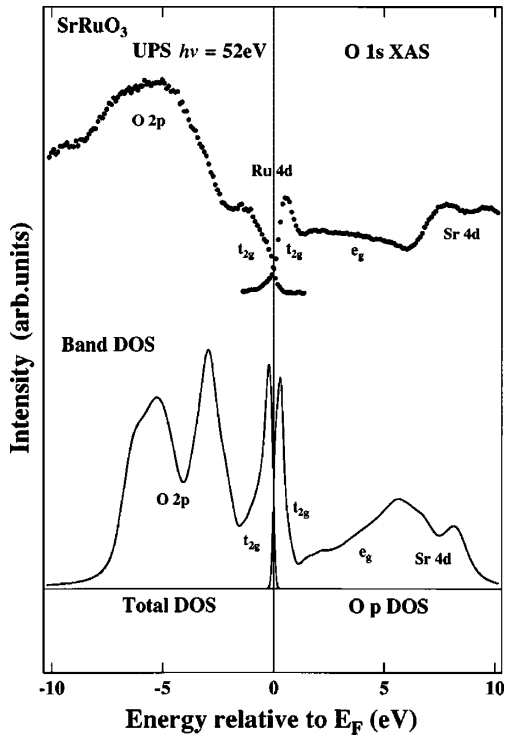

FIG. 46. UPS and O 1*s* XAS spectra of $SrRuO_3$ compared with the band DOS in the ferromagnetic state. The band DOS has been broadened as described in the text. For the XAS spectra, the oxygen p partial DOS is compared. From Fujioka *et al.*, 1997.

By comparing to band calculations, Siemons *et al.* (2007) estimated m_k/m_b to be 0.3 for samples with ruthenium vacancies and 0.6 for stoichiometric samples. For m^*/m_b they used the average value of 4.1 as determined by two different measurements (Allen *et al.*, 1996a; Okamoto *et al.*, 1999). This leads to values of Z^{-1} of 13 and 7 for the ruthenium-poor and stoichiometric samples, respectively. The value of 13 for the ruthenium-poor samples is in line with what has been reported by most (Fujioka *et al.*, 1997; Okamoto *et al.*, 1999; Kim, Chung, and Oh, 2005). The value of 7 for the stoichiometric samples is slightly lower than what was reported by Kim, Chung, and Oh (2005) on their samples. The high values for Z^{-1} have been used by others (Fujioka *et al.*, 1997; Okamoto *et al.*, 1999) to explain the reduction of the t_{2g} peak at the Fermi level due to electron correlation. The work by Siemons *et al.* (2007) showed that the intensity of the t_{2g} peak is sensitive to the ruthenium stoichiometry and that UPS spectra of stoichiometric films look much more like the calculated DOS than ruthenium-poor films. They conclude that ruthenium stoichiometry (and possibly surface states contribute as well) has a much larger impact on PES spectra than previously assumed and could function in large part as an explanation for the observed photoemission results. Of course, the change in the PES spectra could be caused by a change in correlation due to the change in unit cell and the Ru-O-Ru bond angle, but it is also possible that the vacancies themselves cause it. Finally, Siemons *et al.* (2007) proposed that, besides a change in correlation, the transfer of spectral weight could also be caused by inelastic processes at the ruthenium vacancies. The t_{2g} orbitals that form the conduction band form states spreading in two dimensions. To define the energy of a state to within the observed 0.5 eV peak, it is necessary to construct a packet of band states, for a band of width 4 eV, which extended $4/0.5 = 8$ cube edges. The corresponding $\pi \times 4^2 = 50$ ruthenium sites generally contain at least one vacancy, even at only 2% vacancies. It is reasonable to expect that the removal of a band electron might cause shake-off excitations, vibrational or electronic, of the vacancy. This would increase the energy needed to eject the electron, as can be seen in both the UPS and XPS spectra.

High-resolution angle-resolved photoemission spectroscopy (ARPES) is ideally suited for studying the quasiparticle interactions and Fermi surface of $SrRuO_3$. Recently, Shen *et al.* (2010) succeeded in performing ARPES studies of epitaxial thin films of $SrRuO_3$ grown *in situ* by oxide molecular beam epitaxy on $SrTiO_3$. Atomically pristine surfaces were maintained by synthesizing, transferring, and measuring the films under UHV conditions. Consistent with the photoemission studies of Kim, Chung, and Oh (2005) and Siemons *et al.* (2007), sharp t_{2g} spectral weight was observed at E_F, in contrast to results on polycrystalline materials. In addition, on stoichiometric films with high residual resistivity ratios (RRR $>$ 10), sharp quasiparticle bands and Fermi surfaces were clearly observed at low temperatures (10 K). The Fermi surfaces demonstrated excellent agreement with earlier local spin density approximation calculations of the ferromagnetic Fermi surfaces calculated by Singh (1996a), and the quasiparticle dispersion exhibited clear evidence of strong coupling of the electrons to bosons

in the system, which may be the origin of the observed large effective masses.

a. Surface versus bulk spectra

Park *et al.* (2004) studied sputtered films of (Sr, Ca)RuO_3 by *ex situ* photoemission, cleaned in the vacuum system by heating. They introduced a method to extract Ru 4*d* partial spectral weight by measuring at different photon energies, making use of the strong dependence of the photoionization cross section of the Ru 4*d* levels.

As a strategy to extract bulk properties from spectra obtained from *ex situ* prepared samples, a correction is possible by subtracting surface components measured at shallow take-off angles. After such corrections, comparing their spectra (see Fig. 47) with band calculations, Maiti, Singh, and Medicherla (2007b) came to the conclusion that U/W is not larger than 0.2 with a total bandwidth of about 3. This is much smaller than was concluded by H. D. Kim *et al.* (2004) from the core-level measurements. The mass enhancement m^*/m_b is about 2.9, smaller than the 4.1 found with specific heat measurements (Allen *et al.*, 1996a; Okamoto *et al.*, 1999).

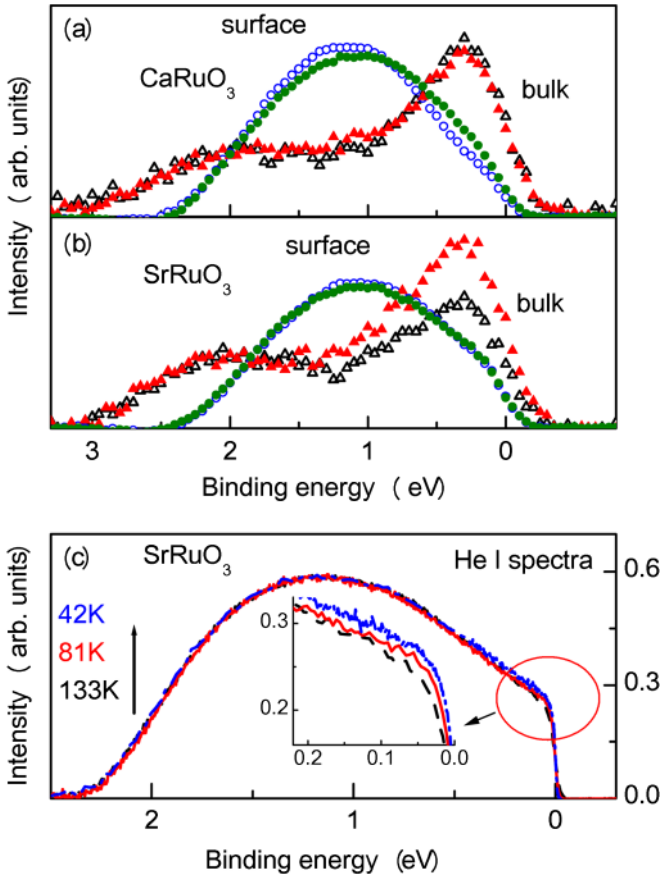

FIG. 47 (color online). Surface (circles) and bulk (triangles) spectral functions of (a) $CaRuO_3$ and (b) $SrRuO_3$. Closed symbols represent spectra at 300 K and the open ones represent spectra at 48 and 35 K for $CaRuO_3$ and $SrRuO_3$, respectively. (c) High-resolution He I spectra of $SrRuO_3$. The dashed, solid, and dot-dashed lines represent the spectrum at 133, 81, and 42 K, respectively. The inset shows the expanded view of the same spectra near the Fermi level. From Maiti, Singh, and Medicherla, 2007b.

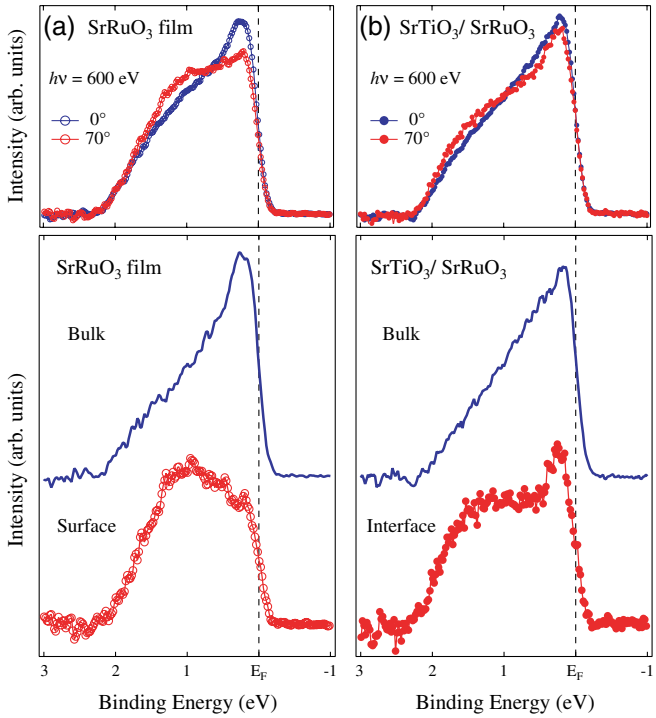

FIG. 48 (color online). Top: Angular dependence of Ru 4*d* spectra for (a) $SrRuO_3$ films and (b) $SrTiO_3/SrRuO_3$ bilayers, where the 70° spectra are more surface and interface sensitive. Bottom: (a) Bulk and surface spectra extracted from the PES spectra for $SrRuO_3$ films and (b) bulk and interface spectra of $SrTiO_3/SrRuO_3$ bilayers. From Kumigashira *et al.*, 2008.

Another technique was introduced by Kumigashira *et al.* (2008), using 600 eV x rays. They capped their films with a thin layer of $SrTiO_3$ in order to protect the surface of the $SrRuO_3$ film and avoid surface reconstructions. In Fig. 48(b) one can see that the valence-band signal at the Fermi level, coming from the interface, is considerably sharper in comparison with the previously obtained results, for example, as seen in Fig. 47, but also an uncapped film [Fig. 48(a)]. These results suggest that correlations are less important than one would conclude from the experiments described above and, as seen in the next section, such conclusions are even more difficult to draw if one has to take the stoichiometry of the samples into account.

E. Influence of strain, stoichiometry, and film thickness on $SrRuO_3$ properties

As noted earlier, the three major influences on the properties of thin films are strain due to growth on a substrate, off-stoichiometry due to the growth process, and the thickness of the film, which could cause effects through a change in dimensionality. In this section these influences are reviewed by looking at their influence on structural, electronic transport, magnetic, and electronic structure of films.

1. Influence of strain

The influence of strain is most easily studied by growing films on different substrates. It has been established that $SrRuO_3$ remains uniformly strained up to thicknesses of

several 100 nm, which allows for determination of strain through measurement of the unit-cell parameters with x-ray diffraction. Vailionis, Siemons, and Koster (2008) studied the effects of strain by growing films on $SrTiO_3$ and $DyScO_3$. The films on $SrTiO_3$ were in compression and those on $DyScO_3$ in tension. They found films on $SrTiO_3$ to be orthorhombic and those on $DyScO_3$ to be tetragonal (both with slight monoclinic distortions of less than 1°). Tensile strain affected the transport properties in a negative way, increasing both the room-temperature and low-temperature resistivity. The changes were attributed to the change in the Ru-O-Ru bond angle, which is related to the bandwidth of the material. In this interpretation, the octahedral rotations are expected to be larger in the tetragonal phase induced by the tensile strain, despite its higher symmetry; see also Vailionis *et al.* (2011). Currently, however, there is no direct evidence for this hypothesis. Vailionis, Siemons, and Koster (2008) repeated the same experiments for $CaRuO_3$ grown on $NdGaO_3$ (compressive strain) and $SrTiO_3$ (tensile strain) and found the same qualitative result. Their resistivity versus temperature transport data are given in Fig. 49. A similar tendency toward higher symmetry under the influence of tensile strain was measured by Choi *et al.* (2010) on $GdScO_3$, as confirmed by x-ray diffraction shown in Fig. 50. Note that R. A. Rao *et al.* (1997) found an even stronger effect: when $CaRuO_3$ was grown under tensile strain, the material was less stable against cation off stoichiometry, and, as a result, some films were found to be semiconducting.

To directly compare the properties of a strained to an unstrained film, one can grow a film, measure the properties, and then etch away the substrate to create a free-standing film to measure the properties of the unstrained film. This is the approach taken by Gan *et al.* (1998), and they observed a reduced Curie temperature, a broadening of the ferromagnetic transition, and a reduction of the saturated magnetic moment

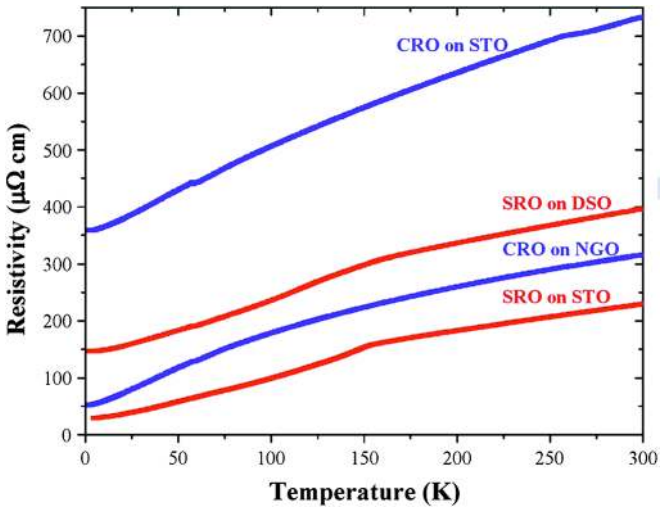

FIG. 49 (color online). Resistivity as a function of temperature of $SrRuO_3$ and $CaRuO_3$ thin films grown on different substrates. $SrRuO_3$ on $DyScO_3$ and $CaRuO_3$ on $SrTiO_3$ layers affected by a higher tensile strain are tetragonal and exhibit larger resistivity values, while orthorhombic $SrRuO_3$ on $SrTiO_3$ and $CaTiO_3$ on $NdGaO_3$ layers show smaller resisitivity values. From Vailionis, Siemons, and Koster, 2008.

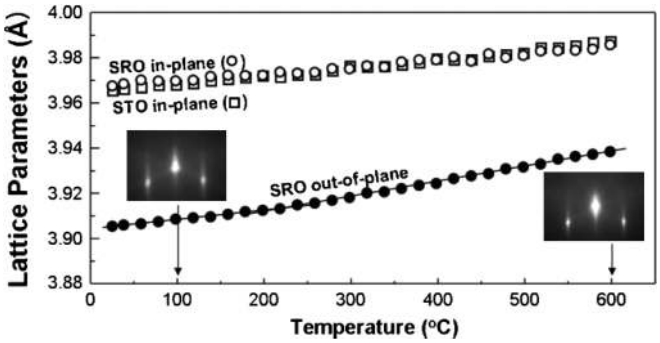

FIG. 50. Temperature dependence of in-plane and out-of-plane lattice parameters of the strained $SrRuO_3$ film grown on a GSO substrate. The insets show RHEED images obtained at different temperatures. From Choi *et al.*, 2010.

compared to bulk when compressive strain is applied (growth on $SrTiO_3$). The effect can be clearly seen in resistivity measurements as a function of temperature in Fig. 51, by comparing T_C.

A more gradual way to apply strain is by growing a buffer layer of a compound for which the lattice parameter can be tuned by changing stoichiometry, or where the strain relaxation is a function of thickness. Jung *et al.* (2004), Lee *et al.* (2008) ($CaHfO_3$), and Terai *et al.* (2004) ($Ba_{1-x}SrTiO_3/BaTiO_3$) used a buffer layer to study the effect of strain on the magnetic properties of $SrRuO_3$. Both groups observed that the direction of the easy axis changes from out of plane for compressive strain [in the (001) pseudocubic direction, similar to what was found by others on $SrTiO_3$; see Fig. 27] to in plane for tensile strain. The magnetization measurements of Terai *et al.* (2004) are shown in Fig. 52.

The changes in structure and magnetism can also be understood from a theoretical point of view. Zayak *et al.* (2006, 2008) showed through *ab initio* calculations how the tilting of the oxygen octahedra dominate the properties of strained films. They also offered a route to a nonmagnetic, which has not been observed experimentally.

In a recent report by Grutter *et al.* (2010), an enhancement of the magnetic moment per Ru atom was seen, as depicted in Fig. 53, by growing thin films on (111)-oriented $SrTiO_3$

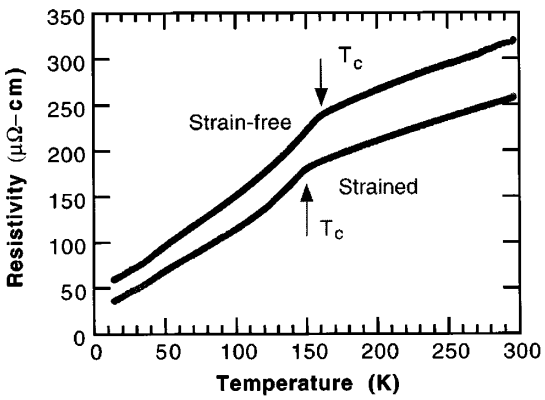

FIG. 51. The resistivity vs temperature curves for both a strained and a strain-relaxed $SrRuO_3$ thin film. The arrows indicate the Curie temperature T_C. From Gan *et al.*, 1998.

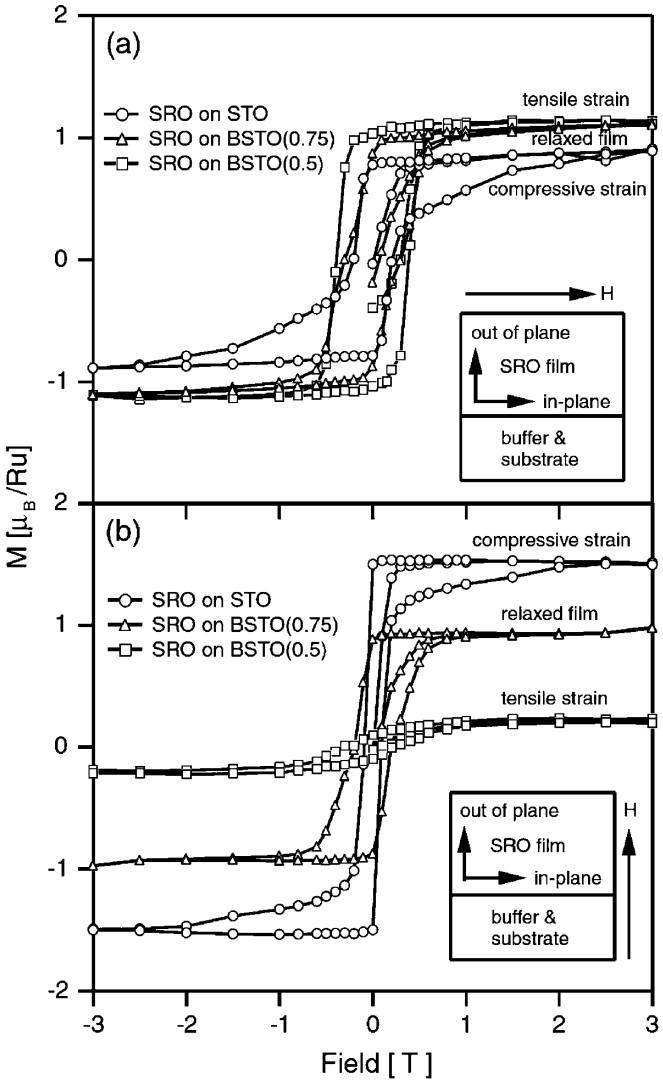

FIG. 52. Magnetic hysteresis loops of strained and strain-free $SrRuO_3$ films on $SrTiO_3$ (STO) and on $Ba_{(1-x)}Sr_xTiO_3$ (BSTO) with $x = 0.75$ and 0.5, respectively. The magnetic field was applied (a) parallel and (b) perpendicular to the sample surface. The measurements were done at 10 K. The compressively strained $SrRuO_3$ (SRO) film shows the largest magnetization and the smallest coercivity, indicating that the easy axis of magnetization is more out of plane. From Terai *et al.*, 2004.

substrates. They observed magnetization values for $(111)_{pc}$ $SrRuO_3$ films of $(2.22–3.4)\mu_B$/Ru ion, exceeding the low spin moment value of the $2\mu_B$/Ru ion. They suggested stabilization of the high-spin $4\mu_B/Ru^{4+}$ configuration to explain the enhanced Ru moment in the trigonally distorted $(111)_{pc}$ $SrRuO_3$ films. Note that the moment showed a large thickness dependence.

2. Influence of stoichiometry

Off stoichiometry in $SrRuO_3$ can occur on either of the cation sites (Sr or Ru) or the anion site (O). Little is known about Sr vacancies, probably because they are hard to create controllably, but Ru and O vacancies are well studied.

Ru off-stoichiometry was studied systematically in polycrystalline samples by Dabrowski *et al.* (2004). They

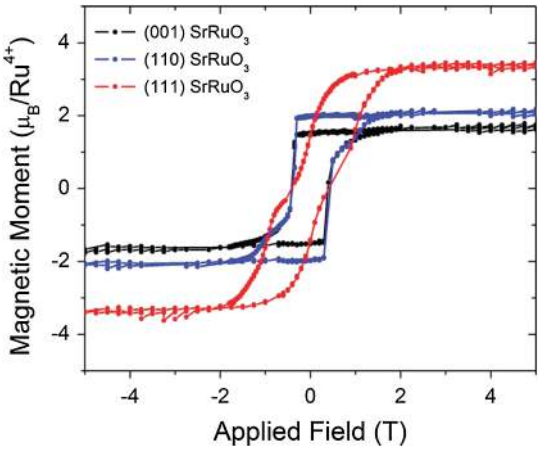

FIG. 53 (color online). Film magnetic moment vs applied field measured with a SQUID magnetometer. Samples were 24-nm-thick (001)-, (110)-, and (111)-oriented $SrRuO_3$ films on $SrTiO_3$. From Grutter *et al.*, 2010.

observed an increase in unit-cell volume with an increase in Ru vacancies. The vacancies also brought the Ru-O-Ru bond angle closer to 180°. At the same time, a reduction in the Curie temperature was observed. This reduction in T_C was not attributed to a weakening of superexchange or double-exchange interaction, but can likely be attributed to enhanced local disorder or to correlation effects due to the strongly hybridized p and d orbitals.

Vacancies on the oxygen sites result in degraded properties as well. Hiratani *et al.* (1996) showed that one can grow crystalline $SrRuO_3$ at pressures as low as 10^{-6} Torr, but at the cost of a tenfold increase in resistivity compared to samples grown at high oxygen pressures (about 100 mTorr). They also observed an upturn of the resistivity at the lowest temperatures. Their transport measurements are shown in Fig. 54 and demonstrate a clear dependence on oxygen pressure. Likely a combination of oxygen off-stoichiometry and cation defects (due to the effect of enhanced particle bombardment at low pressure using PLD) are at play here.

A major influence on the transport properties of $SrRuO_3$ thin films is the stoichiometry of the films. This was demonstrated in a wide range of films by Siemons *et al.* (2007). As mentioned, most films suffer from ruthenium deficiency due to a high oxygen activity during deposition (see Sec. III.E.1). In order to get a quantitative indicator of the ruthenium deficiency, Siemons and co-workers examined the change in lattice parameters in samples ranging from stoichiometric to ruthenium poor. In Fig. 55 θ-2θ, scans for two thick films are shown (330 nm, determined from the period of the fringes), one grown with MBE in low oxygen pressure and one with PLD in high oxygen pressure, to illustrate the difference in the d spacing for the out-of-plane (110) direction of $SrRuO_3$ when different deposition techniques are used. These films are much thicker than the samples compared in other parts of this section to show that the films remain perfectly crystalline and strained up to large thicknesses. In addition these scans reveal the very high degree of crystallinity of the samples by the existence of finite-size fringes in the scans for both samples. As can be seen, the out-of-plane lattice constant is larger for the film grown in high

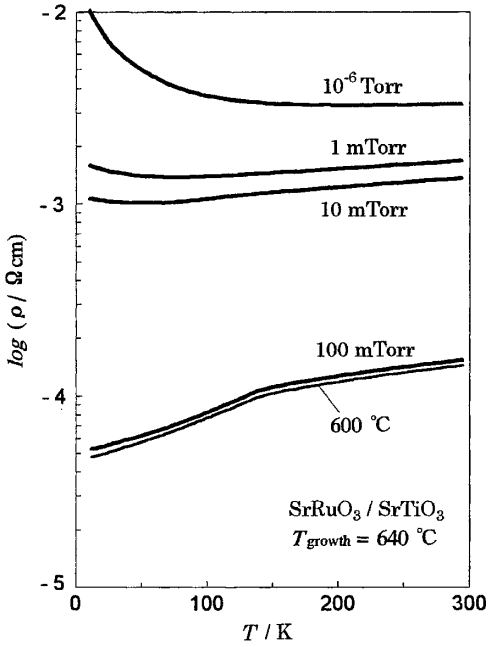

FIG. 54. Oxygen pressure dependence of resistivity vs temperature curves for $SrRuO_3$ thin films grown at 640 °C on $SrTiO_3$ (001) single-crystal substrates. From Hiratani *et al.*, 1996.

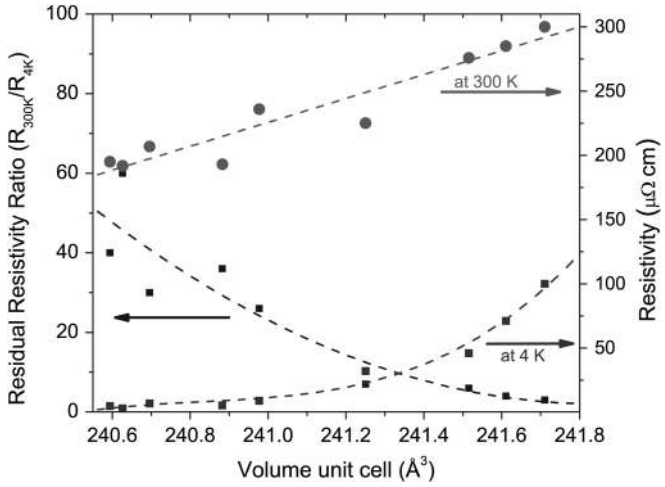

FIG. 56. A comparison between the volume of the $SrRuO_3$ unit cell in thin films on $SrTiO_3$ substrates grown by either MBE or PLD and their transport properties: room-temperature and low-temperature resistivity on the right *y* axis and residual resistance ratio on the left *y* axis. The dashed lines are guides to the eye. From Siemons *et al.*, 2007.

oxygen pressures, which is explained by a lower ruthenium content (Dabrowski *et al.*, 2004). Since the *c* axis (in plane) of the $SrRuO_3$ is fixed by epitaxy (the films are fully strained), the increase in the (110) direction (linear combination of the *a* and *b* axes) is directly proportional to an increase in unit-cell volume, which is taken as a measure of the ruthenium deficiency in Fig. 56.

Figure 56 shows how changes in the transport data correlate with the volumes of the orthorhombic unit cell for various films studied. The room-temperature and low-temperature resistivities, as well as the RRRs, show a clear trend with smaller volumes correlating with the lowest resistivities and highest RRRs. These films are typically found to have been made by MBE (oxygen activity tuned to optimize oxidation and ruthenium sticking). On the other end, PLD films appear to have larger volumes and poorer transport properties. Note that the Curie temperature should also show a similar trend, although the change in T_C is small for this range of vacancy densities (below 2% for these samples). Yoo *et al.* (2005) studied the effect of oxygen partial pressure during PLD and observed Ru vacancies over the whole range. Ito, Masumoto, and Goto (2006) studied film properties as a function of T and pO_2. And larger variations in stoichiometry were reported by Takahashi *et al.* (2002), where a comparison is made between MOCVD and sputter deposition of $SrRuO_3$ (on LSAT and $SrTiO_3$), resulting in metallic and semiconducting behavior, respectively. Sakai *et al.* (2006) annealed their samples in Ar ambient and noticed a loss of oxygen already below 500 °C, as measured with non-Rutherford elastic resonance scattering. When $T > 600$ °C, more dramatic effects were observed, which they called a collapse of the RuO_6 octahedra, but this seemed reversible. The existence of 0.5 mTorr O_2 in the Ar annealing gas was revealed to be effective in making a $SrRuO_3$ film retain its oxygen stoichiometry, crystal structure, and conductivity even T as high as 700 °C. However, it should be noted that the as-sputtered films used in this investigation appeared to have a relatively high resistivity compared to what has been reported by others.

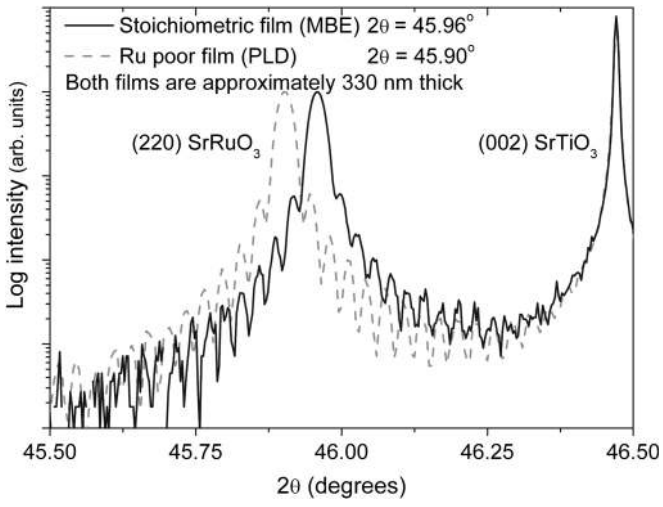

FIG. 55. Comparison of θ-2θ XRD scans of two thick (330 nm) films grown by PLD and MBE. The fringes indicate good crystalline quality of the films, and the shift in peak position shows that the PLD film has a larger out-of-plane lattice parameter (110 direction). From Siemons *et al.*, 2007.

A systematic study of the effect of disorder on the magnetism and transport of $SrRuO_3$ films was performed by Chen *et al.* (1997), who irradiated $SrRuO_3$ PLD films with 400 keV H^+ ions up to 6×10^{16} cm^2 and subsequently measured their resistivity versus temperature. They observed a "blurring" of the magnetic transition, a lowering of T_C by several degrees, and an increase in resistivity (RRR = 3 and $R_{300} = 350$ $\mu\Omega$ at the final dosage) in their samples with starting resistivity parameters of $RRR_{init} = 7$ and $R_{300} = 300$ $\mu\Omega$. In another study, Herranz *et al.* (2008) compared disorder induced both by varying the vicinal cut of the substrate and by irradiation.

In their resistivity data, they observed an increase in resistivity and a lowering of T_C, but also an increasing upturn in the resistivity at temperatures below 100 K and an increasing slope of the resistivity with temperature for higher temperatures, as a function of both vicinal angle and increasing dosage of 100 keV Ar^+ ions up to $10^{13}/cm^2$. They attributed the observations for the low-temperature regime to localization effects, whereas they pointed out that the observed high-temperature resistivity behavior has not been seen in other strongly correlated materials, such as the $A15$ compounds. In a related study, Oh and Park (2000) observed a strongly reduced T_C in sputtered films. They explained this by the fact that the crystal structure is cubic or tetragonal, as was confirmed by TEM measurements, possibly indicative of the existence of point defects, but did not give an explanation for the stability of this structure.

In photoemission experiments, besides the possibility of surface states, differences in valence-band spectra arise from variation in stoichiometry of the film. Siemons *et al.* (2007) observed that ruthenium-poor samples show spectral weight at 1.5 eV in He I UPS, which was previously attributed to an incoherent peak in a picture of a strongly correlated system. When the 1.5 eV peak is absent, the t_{2g} peak at the Fermi level becomes more pronounced. This shift in spectral weight is to be expected when the spectra are compared with DOS calculations; see Fig. 57.

For core-level spectra, Siemons *et al.* (2007) showed that the Ru $3d$ peaks in $SrRuO_3$ with vacancies suggest that ruthenium-poor samples show almost no screened peaks, whereas the stoichiometric samples show pronounced screened peaks. How the details of the surface matter in the case of XPS (as opposed to UPS) is an open question in photoemission studies.

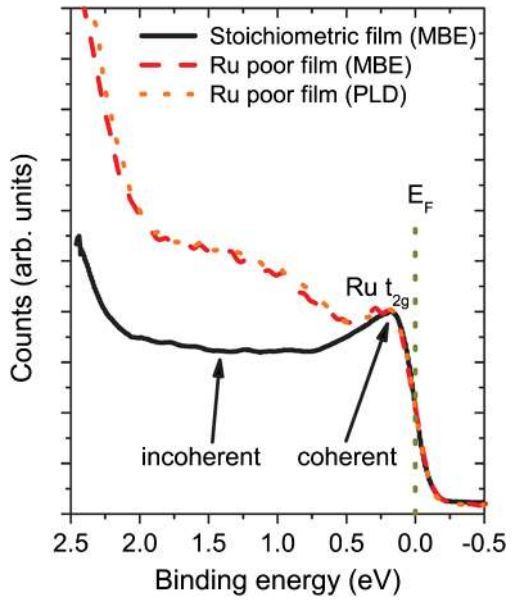

FIG. 57 (color online). UPS spectra at room temperature of three $SrRuO_3$ films: a MBE film, a ruthenium poor MBE film, and a PLD film. All samples show states at the Fermi edge and a Ru t_2g peak close to the Fermi level. The spectra have been normalized on the t_{2g} peak. From Siemons *et al.*, 2007.

3. Substitutions (Sr, *A*)(Ru, *B*)O_3; *A* = Ca, Ba; *B* = Ti

Synthesis methods: Pioneering work by Gupta, Hussey, and Shaw (1996) and Mieville *et al.* (1996, 1997) showed that using PLD it is possible to obtain films with the full range of solid solutions within the (Sr, Ca, Ba)(Ru, Ti)O_3 system. This allows the systematic study of the property-composition relation in a fairly straightforward manner, although one must keep in mind that unavoidably the strain state in these samples is a hidden variable. Furthermore, Gupta, Hussey, and Shaw (1996) showed that epitaxial growth of thin films of $SrTi_{1-x}Ru_xO_{3-\delta}$ by PLD at low oxygen partial pressure [$< 10^{-3}$ mTorr (necessary to make possible the usage of standard RHEED during deposition)] assisted by atomic oxygen, clearly exhibit degraded magnetic and electronic properties. The degree of degradation was later found to be dependent on the exact initial composition (Ohara *et al.*, 2001).

B-site substitutions: Using the same *in situ* synthesis methodology (at standard PLD pressures of 100 mTorr) as mentioned, Kim, Chung, and Oh (2005) studied the metal-to-insulator transition in the $SrTi_{1-x}Ru_xO_3$ system. They came to the conclusion that both disorder and correlation play roles in this system and that the system exhibits a palette of complex metallic and insulating states as a function of composition, which is summarized in Fig. 58. Further studies using *in situ* photoemission and x-ray absorption on films produced by PLD confirmed these observations (Kim *et al.*, 2006). This conclusion was not supported by Abbate *et al.* (2002), who performed their studies on scraped samples.

Other studies that focus on substitutions on the *B* site were performed by Kolesnik *et al.* (2006), who compared the magnetic anisotropy by rotational magnetization using a SQUID magnetometer of a 10% Cr-doped sample with both a nominally pure sample and a Ru-deficient sample. They found that for the Cr-doped sample, the magnetic easy axis is closer to the normal of the surface and explained this result by the assumption of orientational disorder of the RuO_6 octahedra. Hikita *et al.* (2008) observed a negative differential resistance in Schottky junctions formed in Mn-doped $SrRuO_3/Nb$ heterostructures deposited on $SrTiO_3$. They attributed this to an interface effect in which Mn atoms acting as resonance states gave rise to a current peak in the dI/dV measurement. Also noteworthy is the elaborate study by Taniguchi *et al.* (2009) of the crystal structure and magnetic properties of Mn- and Ti-doped $CaRuO_3$.

A-site substitutions: Substitution of Ba or Ca on the Sr position has mostly been studied in bulk samples. Eom *et al.* (1992) were the first to report transport and magnetic properties in thin films as a function of the Sr:Ca ratio, but they were mainly motivated by the fact that the lattice parameters can be tuned from 3.83 to 3.93 Å as a function of this ratio. The ability to tune the lattice parameters allows growth of epitaxial multilayers with many complex oxides. Christen *et al.* (2003) used this same material system as a model to demonstrate a compositional spread method. Finally, Ito, Masumoto, and Goto (2008a, 2008b) used Ba-substituted $SrRuO_3$ on quartz in their research on tailored buffer materials [see also Fukushima *et al.* (1998) and H. C. Kim *et al.*, 2004].

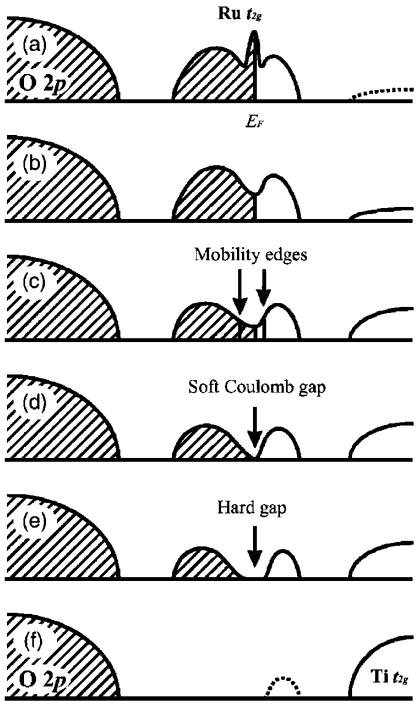

FIG. 58. A schematic diagram for $SrTi_{1-x}Ru_xO_3$. As x decreases, (a) DOS of a correlated metal ($1-x$), shows (b) suppression in the correlated quasiparticle peak first due to disorder (a disordered metal, $x \sim 0.7$). With further decrease of x, (c) mobility edges are formed near E_F (an Anderson insulator, $x \sim 0.5$), and (d) the increased Coulomb interaction results in a soft Coulomb gap at E_F (a soft Coulomb gap insulator, $x \sim 0.4$). (e) Finally the disorder-induced correlation opens a hard gap (a disordered correlation insulator, $x \sim 0.2$). And further decrease of x makes the system (f) a band insulator with a wide optical gap ($x \sim 0$). From Kim, Chung, and Oh, 2005.

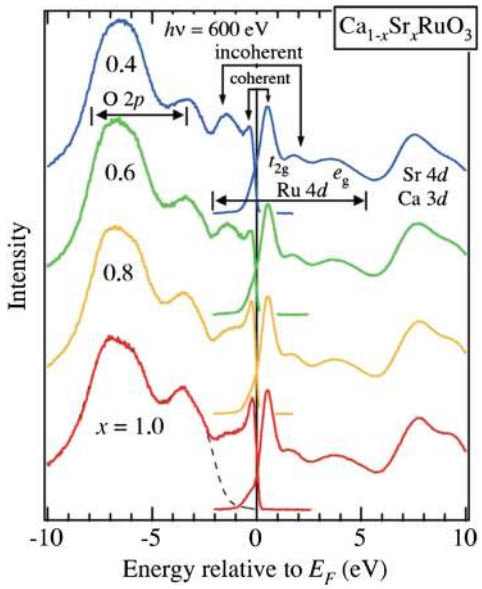

FIG. 59 (color online). A combined plot of the valence-band spectra and the O 1s XAS spectra of $Ca_{1-x}Sr_xRuO_3$. The dashed curve shows how the O 2p band has been subtracted to obtain the Ru 4d band. From Takizawa *et al.*, 2005.

The effect of Ca doping on the valence-band structure was investigated by Manica *et al.* (2004) and confirmed by Takizawa *et al.* (2005) (see Fig. 59). With increasing Ca doping, they found that the Ru 4d peak just below the Fermi level (coherent peak) decreases in intensity. Also, on all samples, they measured lower Ru 4d peaks compared to DOS calculations and attributed this to many-body effects beyond the LDA approximations. However, sharp peaks at the Fermi level were recently observed by various groups on crystalline films, which were analyzed *in situ* (Kim, Chung, and Oh, 2005; Siemons *et al.*, 2007). Singh, Medicherla, and Maiti (2008) saw essentially the same trend, where surface spectra showed more signs of correlation, but they also found a decrease in the coherent part of the valence spectrum for temperatures below the magnetic transition temperature. This reduction was attributed to the exchange coupling moving the down-spin part of this peak above the Fermi level. Core-level measurements by Singh and Maiti (2007) showed the importance of A-site cation-oxygen covalency in these systems with regard to core hole screening, which significantly affects the core-level spectra. This contribution to the spectra decreases with decreasing Ca doping and appears to be insignificant for samples without Ca, i.e., $SrRuO_3$.

4. Superlattices

Examples of substitution studies in more ordered systems, such as superlattices, can be found by Park, Kwon, and Min (2002), Schmising *et al.* (2007b). Woerner *et al.* (2009) used ultrafast x rays to study $SrRuO_3/SrTiO_3$ superlattices and Uozu *et al.* (2004) investigated antiferromagnetic coupling in ferromagnetic oxide trilayer films composed of $Sr_{0.7}Ca_{0.3}RuO_3$ and $La_{0.6}Sr_{0.4}MnO_3$.

In superlattice structures with stoichiometry higher than Sr:Ru = 1:1, other layered ruthenate phases may be stabilized, most notably the Ruddlesden-Popper series $Sr_{n+1}Ru_nO_{3n+1}$. Tian *et al.* (2007) grew this series with $n = 1$–5 and $n = \infty$ ($SrRuO_3$) using reactive MBE. In Fig. 60, high-resolution TEM images are depicted, and from magnetic measurements on these samples they observed an increase of the ferromagnetic transition to 85, 95, and 130 K for the $n = 3$, 4, and 5 compounds, respectively. For $n = 1$ and 2, no ferromagnetic transition was seen. They concluded that the strength of the ferromagnetic interactions is related to the dimensionality of the RuO_2 sheets. Their magnetic measurements are summarized in Fig. 61.

Superlattices are an alternative way to study the effect of dimensionality (compared to the thickness studies described in the following section) on the transport of $SrRuO_3$, i.e., the $SrRuO_3$ layers are embedded in a superlattice with an insulator, and the thickness of the layers is varied. Ueda *et al.* (2000) demonstrated this approach using a superlattice of $SrRuO_3$ and $BaTiO_3$ (in an n:n ML ratio) and found a steady decrease of ferromagnetic transition temperature and magnetization below 11 ML. For the 2 ML sample, they observed antiferromagnetism and anisotropy in the transport properties. Izumi, Nakazawa, and Bando (1998) and Izumi *et al.* (1998) made similar superlattices based on $SrTiO_3$ and $SrRuO_3$. However, they observed metallic conductivity and a ferromagnetic transition for all layers over 1 ML. They also

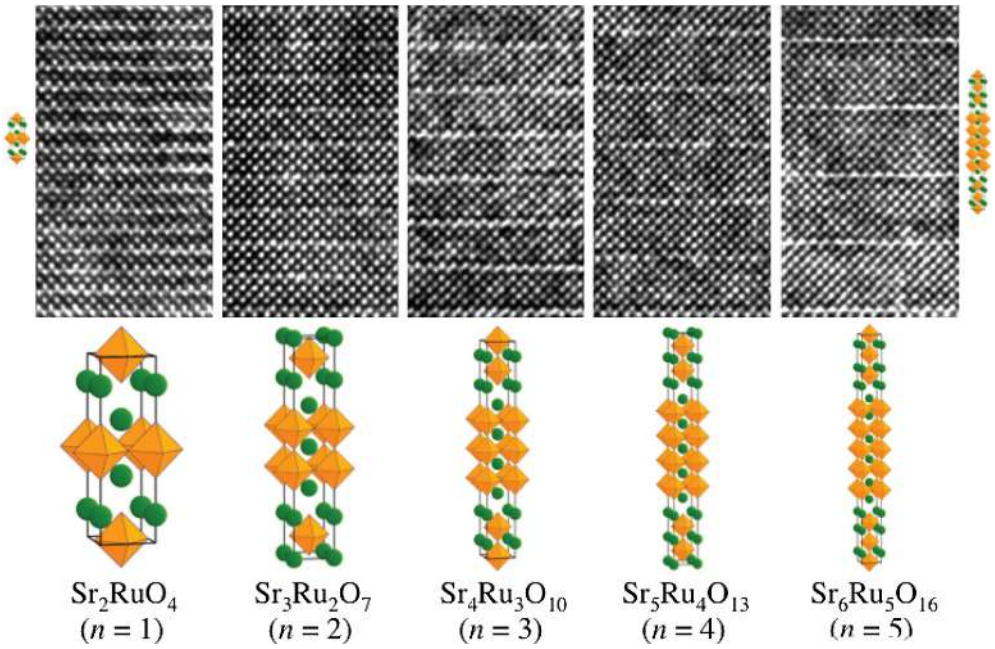

FIG. 60 (color online). Cross-sectional high-resolution TEM images from left to right of $n = 1$–5 $Sr_{n+1}Ru_nO_{3n+1}$ films. The two adjacent white rows in the images correspond to the [100] projections of the rocksalt SrO layers. Between the double SrO layers lies the [100] projection of the $SrRuO_3$ perovskite sheet. From Tian *et al.*, 2007.

observed localization effects at low temperatures for layer thicknesses under 4 ML.

5. Influence of film thickness

Historically, interest in the influence of film thickness on the properties of $SrRuO_3$ thin films was strongly stimulated by the report of a metal-insulator transition (MIT) in $SrRuO_3$ as a function of film thickness reported by Toyota *et al.* (2005, 2006). The question naturally arises whether dimensionality affects the properties of $SrRuO_3$, and, if so, how (Tringides, Jalochowski, and Bauer, 2007). Schultz *et al.* (2009) showed that effects of finite film thickness become more apparent for thicknesses below 10 nm. The Curie temperature decreases and the transition is smeared. Down to $d = 7.5$ nm, there is no change in the orientational transition, while for 5.4 nm the easy axis shifts toward the normal by about 5°, and for $d = 3$ nm, the easy axis is more perpendicular to the film plane for all temperatures below the Curie temperature T_C.

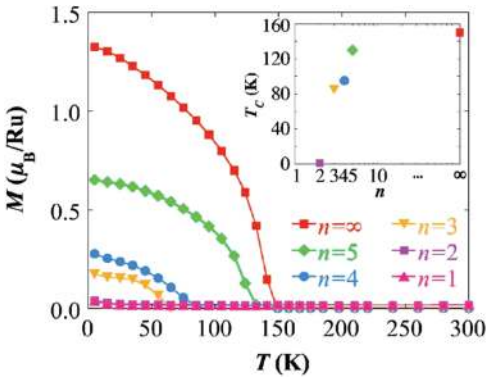

FIG. 61 (color online). Magnetization as a function of temperature of $n = 1$–5 $Sr_{n+1}Ru_nO_{3n+1}$ films and an $n = \infty$ $Sr_{n+1}Ru_nO_{3n+1}$ film. Note that the $n = 3$, 4, 5, and ∞ samples show ferromagnetism, while no sign of ferromagnetism is observed for the $n = 1$ and 2 samples. The inset shows a plot of the ferromagnetic transition temperatures of the $n = 3$, 4, 5, and ∞ $Sr_{n+1}Ru_nO_{3n+1}$ samples vs n. For comparison, the metamagnetic phase transition temperature 1.1 K of the $n = 2$ $Sr_3Ru_2O_7$ single crystal in a magnetic field of 7.9 T data from Grigera *et al.* (2004) is also shown. From Tian *et al.*, 2007.

Xia *et al.* (2009) investigated thinner films and found that, below 4 ML, otherwise metallic and ferromagnetic $SrRuO_3$ films grown on $SrTiO_3$ become insulating, and an antiferromagnetic layer appears with the moment in the plane of the films. They postulated that antiferromagnetic puddles emerge in contact with ferromagnetic puddles.

a. Electronic structure as a function of thickness

Toyota *et al.* (2005, 2006), using transport and photoemission measurements, studied the electronic structure as a function of $SrRuO_3$ film thickness (at the few monolayer level) and showed that an insulator-to-metal transition occurs as film thickness increases. In Fig. 62, one clearly sees the spectral weight decrease with decreasing thickness until at about 4 ML no crossing at the Fermi energy is observed, suggestive of a gap opening. However, atomic force microscopy of these films reveals a morphological evolution as well, going from small 3D islands for thin films to a smooth surface for thicker films. There seems undoubtedly to be a link between the morphology and the magnetic and electronic structure of these films. Films with a smooth morphology throughout the various thickness scales such as observed by Rijnders *et al.* (2004) still remain to be studied using photoemission.

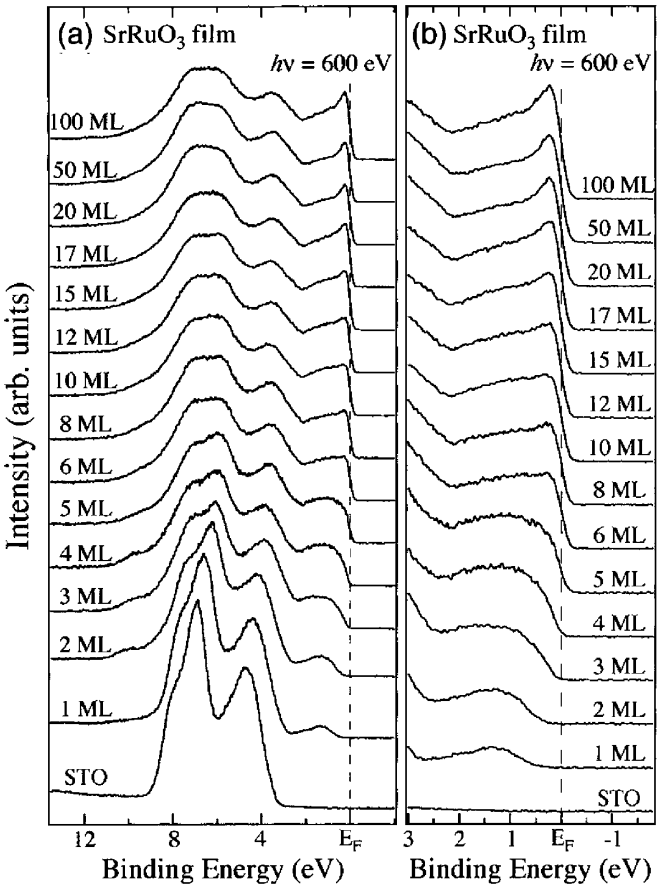

FIG. 62. (a) *In situ* valence-band spectra of $SrRuO_3$ thin films with varying nominal film thickness. (b) The photoemission spectra near E_F in an enlarged binding energy scale. From Toyota *et al.*, 2005, 2006.

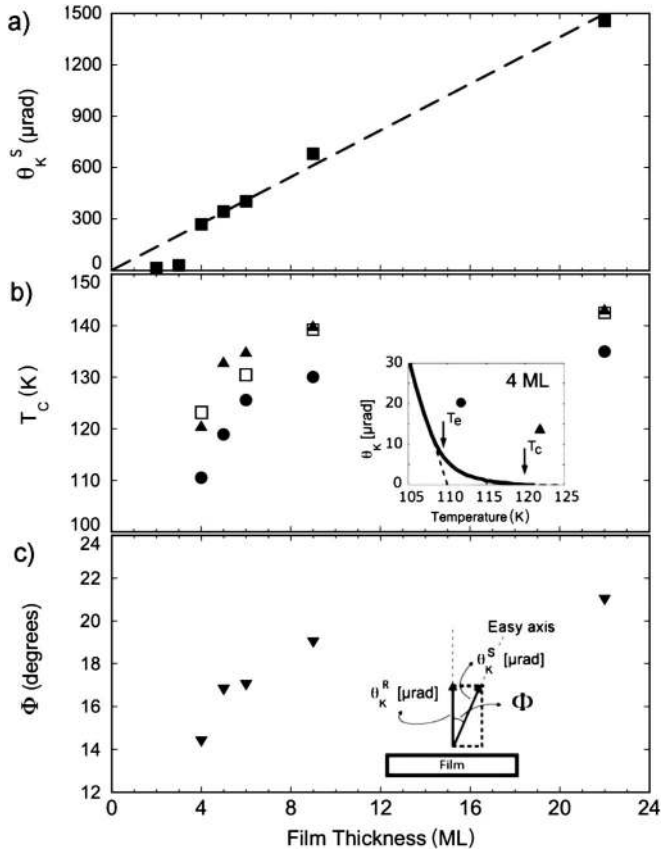

FIG. 63. Thickness dependencies of (a) the saturated Kerr signal (■) at the lowest temperature; (b) Curie temperature T_C (▲), extrapolated Curie temperature T_e (●), and resistivity anomaly (□); and (c) the angle Φ (▼) between film normal and magnetic easy axis at the lowest temperature. The dashed line in (a) is the linear fit of the data point between 4 and 22 ML. The inset in (b) shows how T_C and T_e are determined. From Xia *et al.*, 2009.

b. Magnetism as a function of thickness

The magnetism of $SrRuO_3$ is influenced by the thickness of the film as well. Xia *et al.* (2009) performed a detailed study of films with thicknesses under 10 ML, which they studied using a modified magneto-optical Kerr effect setup (Xia, Beyersdorf *et al.*, 2006). They found an interesting abrupt transition from a ferromagnetic to a paramagnetic state when going from 4 to 3 ML [as opposed to Chang *et al.* (2009) who found a MIT at 1–2 unit-cell layers]. This change in magnetism is accompanied by a MIT. We present here the main findings of their work.

A summary of the results on all their samples is given in Fig. 63. Several properties are shown: the saturation Kerr signal $[\theta_K^S(T)]$, which is determined as the highest point of the hysteresis loop, as a function of thickness; the T_C of the films; the variation of the easy axis; and the magnitude of the coercive field for all ferromagnetic films. One clear result is that below 4 ML there is neither a saturated signal nor a finite Curie temperature, indicating that these films are not ferromagnetic. Taken with the observation on the disappearance of itineracy, they conclude that both ferromagnetism and the MIT occur at the same critical thickness (between 3 and 4 ML). They further note that the saturated Kerr signal is proportional to the film thickness in the range from the thick (22 ML) to the thinnest samples, extrapolating to zero thickness. Noting that all these films are in the very thin limit compared to the optical penetration depth of the light, this result clearly shows that ferromagnetism is lost at a critical thickness below which ferromagnetism is not supported.

Figure 63(b) shows the thickness dependence of T_C. To determine the temperature above which no ferromagnetism is observed, the region near the transition is magnified as shown in the inset of the figure. While in general the magnetization vanishes at T_C, with an exponent smaller than unity, this is not the case for these very thin films. Therefore, two critical temperatures are defined as shown in the inset, and both are plotted in Fig. 63(b). Note that it is T_C, the temperature at which the Kerr signal vanishes, that smoothly extrapolates to the thick film limit and corresponds to previously published data on three-dimensional $SrRuO_3$ films (Klein, Dodge, Ahn, Reiner *et al.*, 1996). Both T_e and T_C vanish below 4 ML. Defining a distance $\zeta \equiv (T_{c-Te})/T_c$, Klein *et al.* noted that ζ increases with decreasing film thickness, especially below ~9 ML. This result may point to the fact that the transition from ferromagnetic to nonferromagnetic films with decreasing thickness is a first-order transition occurring at T_e, with T_C being a mean-field transition. In fact, the lower-temperature data in the $\theta_K(T)$ extrapolate closely to T_C rather than T_e.

These results showed that in ultrathin films of $SrRuO_3$ itinerancy and ferromagnetism disappear at a critical film thickness between 3 and 4 ML. While a MIT could also happen if there are subtle rotations of the oxygen octahedra, rendering the unit-cell symmetry tetragonal or even cubic for extremely thin films, this could not be the case for these fully strained films, since the observed MIT is abrupt while strained films will relieve the strain gradually with increasing thickness. A strong deviation from thick film behavior that begins around 9 ML may indicate either a 2D-to-3D transition or a change in the order of the transition to the ferromagnetic state. At that thickness transport is 2D dominated with a weak localization increase in the resistance at low temperatures.

In addition to the metal-insulator transition, these researchers determined the magnetic anisotropy angle, $\Phi = \cos^{-1}[\theta_K^R(T)/\theta_K^S(T)]$. The results are shown in the inset of Fig. 63(c). Φ as a function of the film thickness is plotted in Fig. 63(c). Φ decreases from 22° in the case of 22 ML film, which is close to the value in thick films (Herranz *et al.*, 2005), to 14° in the 4 ML film. Applying this trend to thinner films would imply that, if they were ferromagnetic, the magnetic easy axis would have been even more out of plane, and thus any ferromagnetic moment would have been easily detected in the zero-field warm-up measurements. The coercive field reaches a maximum for the 9 ML thick film and is lower for both thinner and thicker films.

c. Theory

The cause of the metal-insulator transition is yet to be determined, but the observation by Xia *et al.* (2009) of exchange bias behavior in the thinnest films suggests that it is the creation of an antiferromagnetic layer that drives the system insulating. A theoretical investigation of the problem by Rondinelli, Caffrey *et al.* (2008) has not been able to fully explain the MIT. On the other hand, it did not include extrinsic factors or dynamic spin correlations. The calculations do show that some amount of correlation ($U \sim 0.6$ eV) is needed to fit the models to existing spectroscopic data, suggesting $SrRuO_3$ is a moderately correlated ferromagnet. An increased electron-electron correlation and the lowering of T_C with thickness would match the Stoner model (Stoner, 1938).

Recently, Mahadevan *et al.* (2009) predicted an AFM state for thinner films, which is attributed to the surface RuO_5 unit. The experience from earlier experiments examining the initial growth of $SrRuO_3$ on $SrTiO_3$ point to a so-called termination switch (Rijnders *et al.*, 2004). This entails a switch from a *B*-site termination, as expected from the surface treatment [8], to an *A*-site termination within the first deposited monolayer of $SrRuO_3$, leaving a SrO surface for all investigated thicknesses. This means that Ru is always in a RuO_6 configuration. Liebsch (2003) performed DMFT calculations on $SrRuO_3$ and determined that Coulomb interactions are more pronounced at the surface than in the bulk. In other words, there is more electron-electron interaction at the surface of films. However, this does not agree with recent photoemission findings in which a steady trend is observed toward less correlation as film thickness is increased. It also does not explain the observed MIT between 3 and 4 ML where all the layers at once become conducting and magnetic. One should note, however, that the calculations may be valid in the thick limit.

V. APPLICATIONS

A. Electrodes

$SrRuO_3$ has become the most popular epitaxial electrode for complex oxide heterostructures. In 1999, $SrRuO_3$ appeared on the International Technology Roadmap for Semiconductors for stacked-capacitor dynamic random access memory. As recognized early on by Eom *et al.* (1992), metallic $SrRuO_3$ is a good candidate because of its perfect registry with several substrate materials and its nearly ideal growth mode. These factors result in almost single-crystalline, atomically smooth thin films, as discussed in Sec. III. The most prominent example in this regard has been the successful use of $SrRuO_3$ in ferroelectric perovskite capacitor structures, as first demonstrated by Eom *et al.* (1993) in the case of a $Pb(Zr_{0.52}Ti_{0.48})O_3$ capacitor structure, which is schematically indicated in Fig. 64. In particular, favorable fatigue characteristics were observed (see Fig. 65), as also reported earlier in other oxide-oxide heterostructures (Ramesh *et al.*, 1991, 1992). However, $SrRuO_3$ comes with some notable advantages: it is a nearly isotropic conductor; it is chemically and thermally stable [detailed studies were performed by Halley *et al.* (2004), Lee *et al.* (2004), and Shimizu and Kawakubo (2001)]; it is superior in terms of crystallinity and surface smoothness; it is possible to fabricate these structures at relatively modest temperatures, which minimized interdiffusion; and there is the possibility of domain engineering of low-symmetry oxide thin films on top of $SrRuO_3$ due to its orthorhombic structure.

Numerous other ferroelectric materials have been used in combination with $SrRuO_3$ electrodes. We mention here a few examples: in combination with $BiFeO_3$ (Wang *et al.*, 2004; Yang *et al.*, 2005; Das *et al.*, 2006; Pabst *et al.*, 2007), with dielectrics $(Bi, Nd)_4Ti_3O_{12}$ (Kojima *et al.*, 2002), and other materials (Takahashi *et al.*, 2006) Ahn *et al.* (1996) and Ahn, Hammond *et al.* (1997) demonstrated that $SrRuO_3$ can be

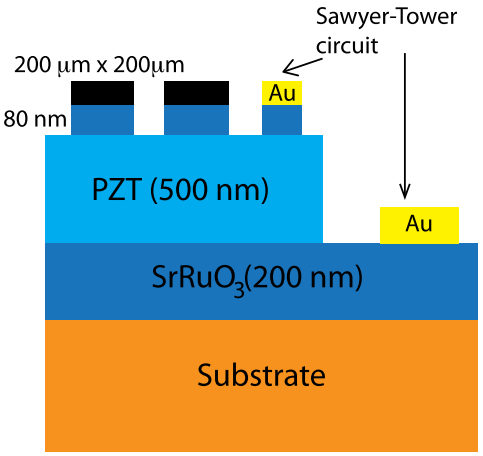

FIG. 64 (color online). Schematic illustration of the capacitor test structure that was used by Eom *et al.* (1993).

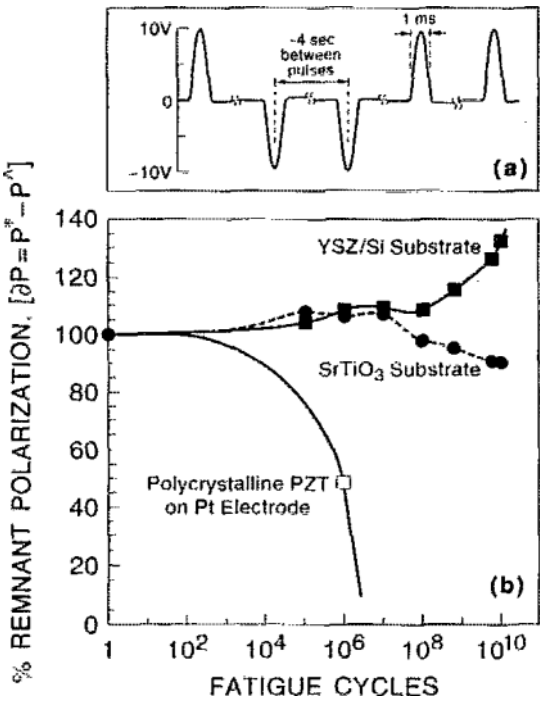

FIG. 65. (a) The pulse train used to measure the effective read cycle discrimination. (b) Remnant polarization vs number of fatigue cycles at 10 V for the $SrRuO_3/PZT/SrRuO_3$ and $SrRuO_3/PZT/SrRuO_3/YSZ/Si$ structures, compared with data for a typical polycrystalline ferroelectric layer on a Pt base electrode. The solid line is a guide to the eye based on behavior reported in the literature (Scott and Paz de Araujo, 1989). From Eom *et al.*, 1993.

electronically modified by switching the ferroelectric material in a heterostructure. Moreover, local switching has been demonstrated: carrier density of $SrRuO_3$ is modified locally by writing switched domains in the ferroelectric material on top using an AFM, as can be seen schematically in Fig. 66 (Ahn, Tybell *et al.*, 1997). Finally, $SrRuO_3$ was used as a gate electrode in field-effect transistors made of transparent oxide thin films (Prins *et al.*, 1996).

$SrRuO_3$ was also used to study strain effects on ferroelectric and multiferroic thin films (Jang *et al.*, 2008; Kim *et al.*, 2008). For example, a strain engineering approach using

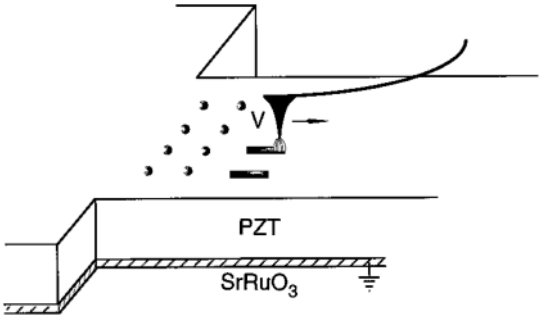

FIG. 66. Schematic of the $PZT/SrTiO_3$ heterostructure. With the use of an AFM with a metallized tip, ferroelectric domains can be polarized by applying a voltage between the tip and $SrRuO_3$ film that exceeds the coercive field of the PZT layer, resulting in a local, nonvolatile change in the electronic properties of the underlying film. From Ahn, Tybell *et al.*, 1997.

epitaxial strain was used to dramatically enhance the properties of $BaTiO_3$ deposited on $SrRuO_3$ electrodes (Choi *et al.*, 2004). This strain was imposed by coherent epitaxy of $BaTiO_3$ and a $SrRuO_3$ bottom electrode deposited on $GdScO_3$ and $DyScO_3$ substrates. This approach capitalizes on the much larger strains that can be imparted on thin films before they break compared to bulk samples and opens up a new way to enhance the properties of oxide materials beyond their bulk counterparts.

The substitution of Ca in $SrRuO_3$ forms a solid solution in which the lattice parameter can be controlled from 3.83 to 3.93 Å. This is important in the growth of coherent ferroelectric thin films on different substrates as a means to study strain effects on ferroelectric thin films. Jang *et al.* (2010) used lattice-matched $Sr_{0.2}Ca_{0.8}RuO_3$ as the bottom and top electrodes on a $NdGaO_3$ substrate to match the lattice parameter and maximize the critical thickness of both the bottom electrode and $SrTiO_3$. Gruverman *et al.* (2009) demonstrated a reproducible tunneling electroresistance effect on nanometer-thick epitaxial $BaTiO_3$ single-crystalline thin films on $SrRuO_3$ bottom electrodes. The results show a change in resistance by about 2 orders of magnitude upon polarization reversal on a lateral scale of 20 nm at room temperature; see Fig. 67. These results are promising for employing ferroelectric tunnel junctions in nonvolatile memory and logic devices. Similar results were obtained in lead zirconate titanate ($Pb[Zr_xTi_{(1-x)}]O_3$) (PZT) and $BaTiO_3$ using a $La_{0.67}Sr_{0.33}MnO_3$ bottom electrode (Maksymovych *et al.*, 2009; Garcia *et al.*, 2010).

Theoretical work on the thickness dependence of ferroelectricity and its relation to the electrode material used was carried out by Junquera and Ghosez (2003) and Nagarajan *et al.* (2006). The most notable result of this work is shown in Fig. 68, where a permanent dipole is lost due to limited screening in the $SrRuO_3$ electrode, in contrast to calculations on metal-oxide systems (F. Y. Rao *et al.*, 1997; Stengel, Vanderbilt, and Spaldin, 2009).

Other theoretical work by Rondinelli, Stengel, and Spaldin (2008) demonstrated a linear magnetoelectric effect that arises from a carrier-mediated mechanism, and is a universal

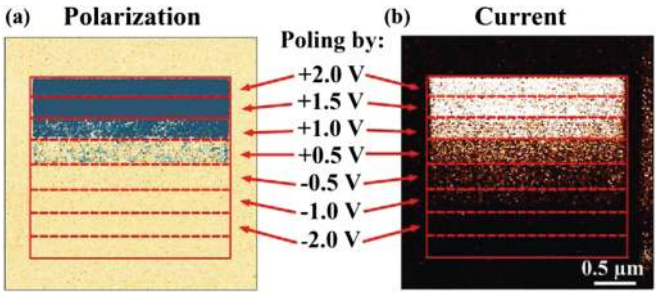

FIG. 67 (color online). Spatially resolved correlation between the onset of polarization reversal (a) and a change in electrical conductance (b). A change in the polarization contrast in (a) illustrates polarization reversal under an incrementally changing tip bias. Dashed lines indicate where the bias is changing. The change in PFM contrast correlates with the transition from low current (dark contrast) to high current (bright contrast). From Gruverman *et al.*, 2009.

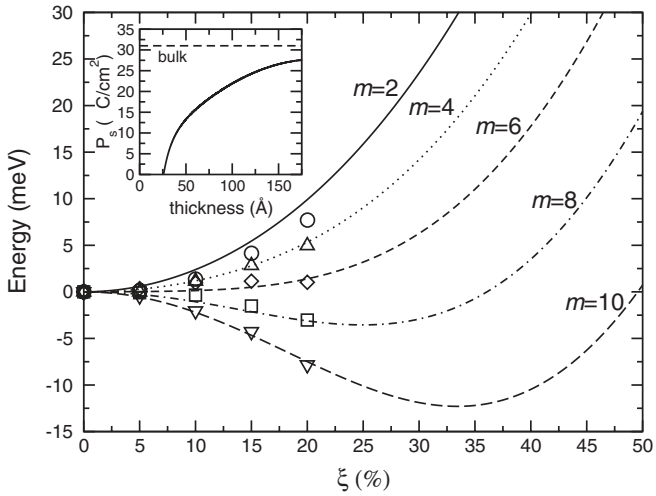

FIG. 68. Evolution of the energy as a function of the soft-mode distortion ξ. First-principles results (symbols) and electrostatic model results (lines) are shown for different thicknesses of the ferroelectric thin film: $m = 2$ (○, full line), $m = 4$ (△, dotted line), $m = 6$ (◇, short-dashed line), $m = 8$ (□, dot-dashed line), and $m = 10$ (▽, long-dashed line). The magnitude of ξ is reported as a percentage of the bulk soft-mode displacements of $BaTiO_3$ atoms ($\xi = 1$ corresponds to the distortion of the bulk tetragonal ferroelectric phase). The energy of the paraelectric phase is taken as reference. The inset shows the evolution of the spontaneous polarization P_s with thickness. For each thickness, P_s is deduced from the amplitude of ξ at the minimum. From Junquera and Ghosez, 2003.

feature of the interface between a dielectric and a spin-polarized metal. Using first-principles DFT calculations they illustrated this effect at the $SrRuO_3/SrTiO_3$ interface, which is schematically depicted in Fig. 69. They point out that this effect could be used to create an interfacial multiferroic.

B. Magnetic tunnel junctions

In some early work, Mieville *et al.* (1998) made a detailed study of the effect of interfaces on transport in various combinations of ferromagnetic oxide and metal interfaces. Somewhat later, the magnetoresistance of a $La_{0.7}Sr_{0.3}MnO_3/SrTiO_3/SrRuO_3$ tunnel junction (Worledge and Geballe, 2000) was studied, and the results used to determine the spin polarization. They found that the MR was negative in $SrRuO_3$. A detailed discussion was given in Sec. IV.A.

In another interesting experiment on all-epitaxial oxide magnetic tunnel junctions, $La_{0.7}Sr_{0.3}MnO_3/SrTiO_3/SrRuO_3$ trilayer films, inverse tunnel magnetoresistance (TMR), i.e., higher and lower junction resistance levels in parallel and antiparallel magnetization configurations, respectively, was observed, indicating the negative spin polarization of $SrRuO_3$ in contrast to the positive one of $La_{0.7}Sr_{0.3}MnO_3$. They observed that the TMR action persists up to T_C of the $SrRuO_3$ layer due to the robust spin polarization at the $SrTiO_3/SrRuO_3$ interface (Takahashi *et al.*, 2003). Other examples of $SrRuO_3/SrTiO_3/SrRuO_3$ heterostructures for magnetic tunnel junctions are the work of Herranz *et al.* (2003c), where they studied the effect of the barrier thickness and observed uncoupled switching of the electrodes above a thickness of 2.5 nm.

VI. MAJOR ISSUES: SOLVED, UNSOLVED, AND THEIR RELATION TO MODERN THEORY QUESTIONS

A great deal has been learned about $SrRuO_3$ over the past two decades, since the renaissance of interest in complex oxides and the demonstration that high-quality thin films could be grown using epitaxial deposition. What makes epitaxial thin films of $SrRuO_3$ so interesting for basic research is the convergence of interesting properties with the ability to measure them in a controlled way thanks to the ability to grow these films reproducibly with the degree of order, and more recently control over their stoichiometry that is usually found only in high-purity single crystals. One of the most important questions for the future is whether the high quality of $SrRuO_3$ thin films for basic study is a peculiarity of this particular material, or whether the advances in thin films deposition and *in situ* characterization that have played such an important role in this case can be generalized. One thing is clear, however, the future will increasingly involve heterostructures with interesting interfaces both for basic studies

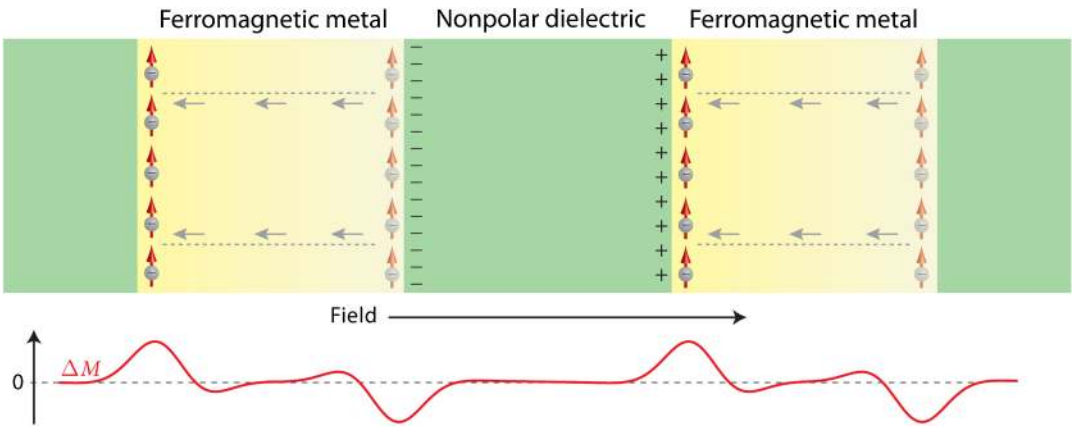

FIG. 69 (color online). Schematic of the carrier-mediated magnetoelectricity mechanism. The accumulation of up-spin electrons adjacent to the positive face of the dielectric, and their depletion from the negative face, leads to the net magnetization change ΔM. From Rondinelli, Stengel, and Spaldin, 2008.

and for applications. The foundations to do this appear to be in place.

But, despite all that has been learned, we believe that a comprehensive understanding of $SrRuO_3$ is still lacking. In what follows, we try to demonstrate this point. The magnetic properties of $SrRuO_3$ are well explored and largely understandable. By contrast, the understanding of all the factors that make it a ferromagnet in the first place, while $CaRuO_3$ is only a paramagnet, seems incomplete. Conventional electronic structure calculations provide some help, but the degree and importance of correlation are still issues, as in so many complex oxides. For example, photoemission data indicate considerable correlation in $SrRuO_3$, but it falls short of being highly correlated. The sensitivity of the degree of correlation to Ru deficiency is striking and surely a demonstration of the importance of local physics. And while several suggestions for the origin of the bad metal behavior observed in $SrRuO_3$ have been put forward, there is no basis yet for selection between them, nor a clear understanding of how the bad metal behavior in $SrRuO_3$ (a clean undoped $S = 1$ itinerant ferromagnet) relates to that well known in the cuprates (disordered doped Mott insulators). Put succinctly, is there a common physical idea underlying bad metal behavior or not? And if there is, what is it?

There are also questions related to the interplay between transport and magnetism. For example, the demonstration of anomalous critical behavior of the resistivity suggests the failure of conventional transport principles, and a comprehensive quantitative understanding of this phenomenon remains a challenge. The demonstration of an unusually large domain-wall resistivity combined with high efficiency in current-induced domain-wall motion has focused attention on the strong interaction between current and the extremely narrow domain walls of this compound. However, the most relevant mechanisms are yet to be determined. The anomalous Hall effect is yet another spin-sensitive transport phenomenon waiting for further study in view of conflicting interpretations. Addressing these questions is likely to make significant contributions to spintronics.

From the materials science point of view there are also opportunities. Since $SrRuO_3$ exhibits such outstanding, almost ideal, film growth, it has the promise to be a model system to study atomistic growth mechanisms for complex oxide materials. Almost all we know now about thin film growth and surface diffusion comes from studies of ''simple'' semiconductors and metals, where it is fairly clear that the constituent atoms hop on the surface, finding energetically favorable kinks or surface steps. The diffusion processes involved in complex oxide film growth and the influence of oxygen pressure on them are both interesting future areas of study. To date, experiments have been limited to observations of the final product of the film growth, as revealed by x-ray diffraction.

Returning again to the question of correlation, since the properties of a material are directly related to the composition and structure (e.g., Ru vacancies), control of the latter at the atomic scale is essential. In the perovskite $SrRuO_3$, the Ru-O-Ru bond angle, determined by the tilting of the oxygen octahedra, dominates the physical properties. In epitaxial thin films, this tilting is determined by the strain and orientation as well as the interface properties of the thin film. This has been demonstrated by various studies of the properties of thin films. Experimentally, a thickness limit of the itinerant ferromagnetic oxide $SrRuO_3$ has been observed. Epitaxial $SrRuO_3$ films remain metallic and ferromagnetic for a thickness larger than three unit cells. Whether this thickness limit is fundamental, due, for instance, to orbital-selective quantum confinement effects, or related to structural changes, due to tilting of the oxygen octahedra, is still an open question. Future experiments, in which the composition and structure of $SrRuO_3$ thin films are controlled at the atomic scale, are required to address these issues. The atomic arrangements, bond angles, and the octahedral shape need to be precisely determined, as well as their effect on the properties. This is probably best performed by studying thin $SrRuO_3$ films within, for instance, heteroepitaxial superlattices.

If nothing else, the symbiotic relationship between the physical study and the materials science of $SrRuO_3$ will be as necessary going forward, as it has been to get us where we are. At the same time, a greater contribution from theory will be necessary if the experimental advances to date are to lead to a comprehensive understanding.

ACKNOWLEDGMENTS

J. S. D. acknowledges support from the Canadian Institute for Advanced Research (CIFAR) and the National Sciences and Engineering Research Council of Canada (NSERC). L. K. acknowledges support by the Israel Science Foundation founded by the Israel Academy of Sciences and Humanities. C. B. E. gratefully acknowledges the financial support of the National Science Foundation through Grants No. ECCS-0708759 and No. DMR-0906443, the Office of Naval Research through Grant No. N00014-07-1-0215, and the David and Lucile Packard Foundation. G. K., G. R., W. S., and D. H. A. B. acknowledge support from the Netherlands foundation for Scientific Research (NWO) and NanoNed. The work at Stanford was supported initially by the U.S. Air Force Office of Scientific Research and subsequently by the U.S. Department of Energy through the Office of Basic Energy Sciences. The authors are grateful for useful discussions held with Ted Geballe, Aharon Kapitulnik, Robert Hammond, Jim Reiner, Charles Ahn, and Kyle Shen.

REFERENCES

Abbate, M., J. A. Guevara, S. L. Cuffini, Y. P. Mascarenhas, and E. Morikawa, 2002, Eur. Phys. J. B **25**, 203.

Ahn, C. H., L. Antognazza, T. Tybell, K. Char, M. Decroux, R. H. Hammond, T. H. Geballe, M. R. Beasley, O. Fischer, and J. M. Triscone, 1996, J. Low Temp. Phys. **105**, 1517.

Ahn, C. H., R. H. Hammond, T. H. Geballe, M. R. Beasley, J. M. Triscone, M. Decroux, O. Fischer, L. Antognazza, and K. Char, 1997, Appl. Phys. Lett. **70**, 206.

Ahn, C. H., T. Tybell, L. Antognazza, K. Char, R. H. Hammond, M. R. Beasley, O. Fischer, and J. M. Triscone, 1997, Science **276**, 1100.

Albina, J. M., M. Mrovec, B. Meyer, and C. Elsaesser, 2007, Phys. Rev. B **76**, 165103.

Alexander, S., J. S. Helman, and I. Balberg, 1976, Phys. Rev. B **13**, 304.

Allen, P. B., H. Berger, O. Chauvet, L. Forro, T. Jarlborg, A. Junod, B. Revaz, and G. Santi, 1996a, Phys. Rev. B **53**, 4393.
Allen, P. B., H. Berger, O. Chauvet, L. Forro, T. Jarlborg, A. Junod, B. Revaz, and G. Santi, 1996b, Phys. Rev. B **53**, 4393.
Allen, P. B., R. M. Wentzcovitch, W. W. Schulz, and P. C. Canfield, 1993, Phys. Rev. B **48**, 4359.
Argyle, B., S. Charap, and E. Pugh, 1963, Phys. Rev. **132**, 2051.
Asulin, I., O. Yuli, G. Koren, and O. Millo, 2006, Phys. Rev. B **74**, 092501.
Averitt, R. D., and A. J. Taylor, 2002, J. Phys. Condens. Matter **14**, R1357.
Bachelet, R., F. Sanchez, J. Santiso, and J. Fontcuberta, 2008, Appl. Phys. Lett. **93**, 151916.
Bachelet, R., F. Sanchez, J. Santiso, C. Munuera, C. Ocal, and J. Fontcuberta, 2009, Chem. Mater. **21**, 2494.
Barnas, J., and A. Fert, 1994, Phys. Rev. B **49**, 12 835.
Basov, D. N., and T. Timusk, 2005, Rev. Mod. Phys. **77**, 721.
Bell, W. E., and M. Tagami, 1963, J. Phys. Chem. **67**, 2432.
Berger, L., 1970, Phys. Rev. B **2**, 4559.
Berry, M. V., 1984, Proc. R. Soc. A **392**, 45.
Bozovic, I., J. H. Kim, J. S. Harris, C. B. Eom, J. M. Phillips, and J. T. Cheung, 1994, Phys. Rev. Lett. **73**, 1436.
Bushmeleva, S. N., V. Y. Pomjakushin, E. V. Pomjakushina, D. V. Sheptyakov, and A. M. Balagurov, 2006, J. Magn. Magn. Mater. **305**, 491.
Campbell, I. A., and A. Fert, 1982, in *Handbook of Ferromagnetic Materials*, edited by E. P. Wohlfarth (North-Holland, Amsterdam), Vol. 3, Chap. 9, p. 747.
Cao, G., S. McCall, M. Shepard, J. E. Crow, and R. P. Guertin, 1997, Phys. Rev. B **56**, 321.
Capogna, L., *et al.*, 2002, Phys. Rev. Lett. **88**, 076602.
Chae, R. H., R. A. Rao, Q. Gan, and C. B. Eom, 2000, J. Electroceram. **4**, 345.
Chang, Y. J., C. H. Kim, S. H. Phark, Y. S. Kim, J. Yu, and T. W. Noh, 2009, Phys. Rev. Lett. **103**, 057201.
Chen, C. L., Y. Cao, Z. J. Huang, Q. D. Jiang, Z. Zhang, Y. Y. Sun, W. N. Kang, L. M. Dezaneti, W. K. Chu, and C. W. Chu, 1997, Appl. Phys. Lett. **71**, 1047.
Choi, J., C. B. Eom, G. Rijnders, H. Rogalla, and D. H. A. Blank, 2001, Appl. Phys. Lett. **79**, 1447.
Choi, K. J., S. H. Baek, H. W. Jang, L. J. Belenky, M. Lyubchenko, and C.-B. Eom, 2010, Adv. Mater. **22**, 759.
Choi, K. J., *et al.*, 2004, Science **306**, 1005.
Chopdekar, R. V., Y. Takamura, and Y. Suzuki, 2006, J. Appl. Phys. **99**, 08F503.
Christen, H. M., and G. Eres, 2008, J. Phys. Condens. Matter **20**, 264005.
Christen, H. M., C. M. Rouleau, I. Ohkubo, H. Y. Zhai, H. N. Lee, S. Sathyamurthy, and D. H. Lowndes, 2003, Rev. Sci. Instrum. **74**, 4058.
Cox, P. A., R. G. Egdell, J. B. Goodenough, A. Hamnett, and C. C. Naish, 1983, J. Phys. C **16**, 6221.
Crandles, D. A., F. Eftekhari, R. Faust, G. S. Rao, and F. S. Razavi, 2008a, J. Phys. D **41**, 135007.
Crandles, D. A., F. Eftekhari, R. Faust, G. S. Rao, M. Reedyk, and F. S. Razavi, 2008b, Appl. Opt. **47**, 4205.
Dabrowski, B., O. Chmaissem, P. W. Klamut, S. Kolesnik, M. Maxwell, J. Mais, Y. Ito, B. D. Armstrong, J. D. Jorgensen, and S. Short, 2004, Phys. Rev. B **70**, 014423.
Das, R. R., *et al.*, 2006, Appl. Phys. Lett. **88**, 242904.
de Gennes, P. G., and J. Friedel, 1958, J. Phys. Chem. Solids **4**, 71.
Dodge, J. S., *et al.*, 1999a, Phys. Rev. B **60**, R6987.
Dodge, J. S., *et al.*, 1999b, Phys. Rev. B **60**, R6987.
Dodge, J. S., C. P. Weber, J. Corson, J. Orenstein, Z. Schlesinger, J. W. Reiner, and M. R. Beasley, 2000, Phys. Rev. Lett. **85**, 4932.
Dordevic, S., and D. N. Basov, 2006, Ann. Phys. (N.Y.) **15**, 545.
Emery, V. J., and S. A. Kivelson, 1995, Phys. Rev. Lett. **74**, 3253.
Eom, C. B., R. J. Cava, R. M. Fleming, J. M. Phillips, R. B. Vandover, J. H. Marshall, J. W. P. Hsu, J. J. Krajewski, and W. F. Peck, 1992, Science **258**, 1766.
Eom, C. B., J. Z. Sun, K. Yamamoto, A. F. Marshall, K. E. Luther, T. H. Geballe, and S. S. Laderman, 1989, Appl. Phys. Lett. **55**, 595.
Eom, C. B., R. B. Vandover, J. M. Phillips, D. J. Werder, J. H. Marshall, C. H. Chen, R. J. Cava, R. M. Fleming, and D. K. Fork, 1993, Appl. Phys. Lett. **63**, 2570.
Fang, Z., N. Nagaosa, K. S. Takahashi, A. Asamitsu, R. Mathieu, T. Ogasawara, H. Yamada, M. Kawasaki, Y. Tokura, and K. Terakura, 2003, Science **302**, 92.
Feigenson, M., L. Klein, M. Karpovski, J. W. Reiner, and M. R. Beasley, 2005, J. Appl. Phys. **97**, 10J120.
Feigenson, M., L. Klein, J. W. Reiner, and M. R. Beasley, 2003, Phys. Rev. B **67**, 134436.
Feigenson, M., J. W. Reiner, and L. Klein, 2007, Phys. Rev. Lett. **98**, 247204.
Feigenson, M., J. W. Reiner, and L. Klein, 2008, J. Appl. Phys. **103**, 07E741.
Fisher, M. E., and J. S. Langer, 1968, Phys. Rev. Lett. **20**, 665.
Fujioka, K., J. Okamoto, T. Mizokawa, A. Fujimori, I. Hase, M. Abbate, H. J. Lin, C. T. Chen, Y. Takeda, and M. Takano, 1997, Phys. Rev. B **56**, 6380.
Fukushima, N., K. Sano, T. Schimizu, K. Abe, and S. Komatsu, 1998, Appl. Phys. Lett. **73**, 1200.
Funakubo, H., T. Oikawa, N. Higashi, and K. Saito, 2002, J. Cryst. Growth **235**, 401.
Gan, Q., R. A. Rao, and C. B. Eom, 1997, Appl. Phys. Lett. **70**, 1962.
Gan, Q., R. A. Rao, C. B. Eom, J. L. Garrett, and M. Lee, 1998, Appl. Phys. Lett. **72**, 978.
Gan, Q., R. A. Rao, C. B. Eom, L. Wu, and F. Tsui, 1999, J. Appl. Phys. **85**, 5297.
Garcia, V., *et al.*, 2010, Science **327**, 1106.
Genish, I., Y. Kats, L. Klein, J. W. Reiner, and M. R. Beasley, 2004, J. Appl. Phys. **95**, 6681.
Genish, I., L. Klein, J. Reiner, and M. Beasley, 2007, Phys. Rev. B **75**, 125108.
Georges, A., G. Kotliar, W. Krauth, and M. J. Rozenberg, 1996, Rev. Mod. Phys. **68**, 13.
Grigera, S. A., *et al.*, 2004, Science **306**, 1154.
Grutter, A., F. Wong, E. Arenholz, M. Liberati, A. Vailionis, and Y. Suzuki, 2010, Appl. Phys. Lett. **96**, 082509.
Gruverman, A., *et al.*, 2009, Nano Lett. **9**, 3539.
Gunnarsson, O., and O. Roesch, 2008, J. Phys. Condens. Matter **20**, 043201.
Gupta, A., B. W. Hussey, and T. M. Shaw, 1996, Mater. Res. Bull. **31**, 1463.
Haham, N., Y. Shperber, M. Schultz, N. Naftalis, E. Shimshoni, J. W. Reiner, and L. Klein, 2011, Phys. Rev. B **84**, 174439.
Halley, D., C. Rossel, D. Widmer, H. Wolf, and S. Gariglio, 2004, Mater. Sci. Eng. B **109**, 113.
Herranz, G., N. Dix, F. Sanchez, B. Martinez, J. Fontcuberta, M. V. Garcia-Cuenca, C. Ferrater, M. Varela, D. Hrabovsky, and A. R. Fert, 2005, J. Appl. Phys. **97**, 10M321.
Herranz, G., V. Laukhin, F. Sanchez, P. Levy, C. Ferrater, M. V. Garcia-Cuenca, M. Varela, and J. Fontcuberta, 2008, Phys. Rev. B **77**, 165114.

Herranz, G., B. Martinez, J. Fontcuberta, F. Sanchez, C. Ferrater, M. V. Garcia-Cuenca, and M. Varela, 2003a, Phys. Rev. B **67**, 174423.
Herranz, G., B. Martinez, J. Fontcuberta, F. Sanchez, M. V. Garcia-Cuenca, C. Ferrater, and M. Varela, 2003b, Appl. Phys. Lett. **82**, 85.
Herranz, G., B. Martinez, J. Fontcuberta, F. Sanchez, M. V. Garcia-Cuenca, C. Ferrater, and M. Varela, 2003c, J. Appl. Phys. **93**, 8035.
Herranz, G., F. Sanchez, N. Dix, D. Hrabovsky, I. C. Infante, J. Fontcuberta, M. V. Garcia-Cuenca, C. Ferrater, and M. Varela, 2006, Appl. Phys. Lett. **89**, 152501.
Herranz, G., F. Sanchez, B. Martinez, J. Fontcuberta, M. Garcia-Cuenca, C. Ferrater, M. Varela, and P. Levy, 2004, Eur. Phys. J. B **40**, 439.
Herranz, G., R. Sanchez, B. Martinez, J. Fontcuberta, M. Garcia-Cuenca, C. Ferrater, and M. Varela, 2004, Mater. Sci. Eng. B **109**, 221.
Herring, C., and C. Kittel, 1951, Phys. Rev. **81**, 869.
Hikita, Y., L. F. Kourkoutis, T. Susaki, D. A. Muller, H. Takagi, and H. Y. Hwang, 2008, Phys. Rev. B **77**, 205330.
Hiratani, M., C. Okazaki, K. Imagawa, and K. Takagi, 1996, Jpn. J. Appl. Phys. **35**, 6212.
Hong, W., H. N. Lee, M. Yoon, H. M. Christen, D. H. Lowndes, Z. G. Suo, and Z. Y. Zhang, 2005, Phys. Rev. Lett. **95**, 095501.
Iliev, M. N., A. P. Litvinchuk, H.-G. Lee, C. L. Chen, M. L. Dezaneti, C. W. Chu, V. G. Ivanov, M. V. Abrashev, and V. N. Popov, 1999, Phys. Rev. B **59**, 364.
Imada, M., A. Fujimori, and Y. Tokura, 1998, Rev. Mod. Phys. **70**, 1039.
Inoue, I. H., Y. Aiura, Y. Nishihara, Y. Haruyama, S. Nishizaki, Y. Maeno, T. Fujita, J. G. Bednorz, and F. Lichtenberg, 1996a, Physica B (Amsterdam) **223–224**, 516.
Inoue, I. H., Y. Aiura, Y. Nishihara, Y. Haruyama, S. Nishizaki, Y. Maeno, T. Fujita, J. G. Bednorz, and F. Lichtenberg, 1996b, J. Electron Spectrosc. Relat. Phenom. **78**, 175.
Ioffe, L. B., and A. J. Millis, 1998, Phys. Rev. B **58**, 11 631.
Ito, A., H. Masumoto, and T. Goto, 2006, Mater. Trans., JIM **47**, 2808.
Ito, A., H. Masumoto, and T. Goto, 2008a, Mater. Trans., JIM **49**, 1822.
Ito, A., H. Masumoto, and T. Goto, 2008b, J. Ceram. Soc. Jpn. **116**, 441.
Ito, A., H. Masumoto, and T. Goto, 2009, Thin Solid Films **517**, 5616.
Izumi, M., K. Nakazawa, and Y. Bando, 1998, J. Phys. Soc. Jpn. **67**, 651.
Izumi, M., K. Nakazawa, Y. Bando, and Y. Yoneda, 1998, Solid State Ionics **108**, 227.
Izumi, M., K. Nakazawa, Y. Bando, Y. Yoneda, and H. Terauchi, 1997, J. Phys. Soc. Jpn. **66**, 3893.
Jang, H. W., *et al.*, 2008, Phys. Rev. Lett. **101**, 107602.
Jang, H. W., *et al.*, 2010, Phys. Rev. Lett. **104**, 197601.
Jiang, J. C., X. Q. Pan, and C. L. Chen, 1998, Appl. Phys. Lett. **72**, 909.
Jiang, J. C., W. Tian, X. Pan, Q. Gan, and C. B. Eom, 1998a, Mater. Sci. Eng. B **56**, 152.
Jiang, J. C., W. Tian, X. Q. Pan, Q. Gan, and C. B. Eom, 1998b, Appl. Phys. Lett. **72**, 2963.
Jones, C. W., P. D. Battle, P. Lightfoot, and W. T. A. Harrison, 1989, Acta Crystallogr. Sect. C **45**, 365.
Jung, C. U., H. Yamada, M. Kawasaki, and Y. Tokura, 2004, Appl. Phys. Lett. **84**, 2590.
Jungwirth, T., Q. Niu, and A. H. MacDonald, 2002, Phys. Rev. Lett. **88**, 207208.
Junquera, J., and P. Ghosez, 2003, Nature (London) **422**, 506.
Kamal, S., D. M. Kim, C. B. Eom, and J. S. Dodge, 2006, Phys. Rev. B **74**, 165115.
Kanbayasi, A., 1976a, J. Phys. Soc. Jpn. **41**, 1876.
Kanbayasi, A., 1976b, J. Phys. Soc. Jpn. **41**, 1879.
Kanbayasi, A., 1978, J. Phys. Soc. Jpn. **44**, 108.
Karplus, R., and J. M. Luttinger, 1954, Phys. Rev. **95**, 1154.
Kats, Y., I. Genish, L. Klein, J. W. Reiner, and M. R. Beasley, 2004, Phys. Rev. B **70**, 180407.
Kats, Y., I. Genish, L. Klein, J. W. Reiner, and M. R. Beasley, 2005, Phys. Rev. B **71**, 100403.
Kats, Y., and L. Klein, 2002, Physica B (Amsterdam) **312–313**, 793.
Kats, Y., L. Klein, J. W. Reiner, T. H. Geballe, M. R. Beasley, and A. Kapitulnik, 2001, Phys. Rev. B **63**, 054435.
Kaul, S. N., 1991, J. Phys. Condens. Matter **3**, 4027.
Kawasaki, M., K. Takahashi, T. Maeda, R. Tsuchiya, M. Shinohara, O. Ishiyama, T. Yonezawa, M. Yoshimoto, and H. Koinuma, 1994, Science **266**, 1540.
Kennedy, B. J., and B. A. Hunter, 1998, Phys. Rev. B **58**, 653.
Kent, A. D., U. Rudiger, J. Yu, L. Thomas, and S. S. P. Parkin, 1999, J. Appl. Phys. **85**, 5243.
Kim, D., B. L. Zink, F. Hellman, S. McCall, G. Cao, and J. E. Crow, 2003, Phys. Rev. B **67**, 100406.
Kim, D. H., H. N. Lee, M. D. Biegalski, and H. M. Christen, 2008, Appl. Phys. Lett. **92**, 012911.
Kim, H. C., Y. S. Kim, Y. B. Kim, and D. K. Choi, 2004, J. Non-Cryst. Solids **336**, 107.
Kim, H. D., H. J. Noh, K. H. Kim, and S. J. Oh, 2004, Phys. Rev. Lett. **93**, 126404.
Kim, J., J. Chung, and S. J. Oh, 2005, Phys. Rev. B **71**, 121406.
Kim, J., J. Y. Kim, B. G. Park, and S. J. Oh, 2006, Phys. Rev. B **73**, 235109.
Kim, M.-H., *et al.*, 2007, Phys. Rev. B **75**, 214416.
Kirillov, D., Y. Suzuki, L. Antognazza, K. Char, I. Bozovic, and T. H. Geballe, 1995, Phys. Rev. B **51**, 12 825.
Kiyama, T., K. Yoshimura, K. Kosuge, Y. Ikeda, and Y. Bando, 1996, Phys. Rev. B **54**, R756.
Kleibeuker, J. E., *et al.*, 2010, Adv. Funct. Mater. **20**, 3490.
Klein, L., 2006, Appl. Phys. Lett. **89**, 036101.
Klein, L., L. Antognazza, T. H. Geballe, M. R. Beasley, and A. Kapitulnik, 1999, Phys. Rev. B **60**, 1448.
Klein, L., J. S. Dodge, C. H. Ahn, J. W. Reiner, L. Mieville, T. H. Geballe, M. R. Beasley, and A. Kapitulnik, 1996, J. Phys. Condens. Matter **8**, 10111.
Klein, L., J. S. Dodge, C. H. Ahn, G. J. Snyder, T. H. Geballe, M. R. Beasley, and A. Kapitulnik, 1996, Phys. Rev. Lett. **77**, 2774.
Klein, L., J. S. Dodge, T. H. Geballe, M. R. Beasley, and A. Kapitulnik, 2000, Phys. Rev. Lett. **84**, 2280.
Klein, L., J. S. Dodge, T. H. Geballe, A. Kapitulnik, A. F. Marshall, L. Antognazza, and K. Char, 1995a, Appl. Phys. Lett. **66**, 2427.
Klein, L., J. S. Dodge, T. H. Geballe, A. Kapitulnik, A. F. Marshall, L. Antognazza, and K. Char, 1995b, Appl. Phys. Lett. **66**, 2427.
Klein, L., Y. Kats, A. F. Marshall, J. W. Reiner, T. H. Geballe, M. R. Beasley, and A. Kapitulnik, 2000, Phys. Rev. Lett. **84**, 6090.
Klein, L., Y. Kats, N. Wiser, M. Konczykowski, J. W. Reiner, T. H. Geballe, M. R. Beasley, and A. Kapitulnik, 2001, Europhys. Lett. **55**, 532.
Klein, L., J. R. Reiner, T. H. Geballe, M. R. Beasley, and A. Kapitulnik, 2000, Phys. Rev. B **61**, R7842.
Kojima, T., T. Sakai, T. Watanabe, H. Funakubo, K. Saito, and M. Osada, 2002, Appl. Phys. Lett. **80**, 2746.
Kolesnik, S., Y. Z. Yoo, O. Chmaissem, B. Dabrowski, T. Maxwell, C. W. Kimball, and A. P. Genis, 2006, J. Appl. Phys. **99**, 08F501.

Koster, G., B. L. Kropman, G. J. H. M. Rijnders, D. H. A. Blank, and H. Rogalla, 1998, Appl. Phys. Lett. **73**, 2920.
Kostic, P., Y. Okada, N. C. Collins, Z. Schlesinger, J. W. Reiner, L. Klein, A. Kapitulnik, T. H. Geballe, and M. R. Beasley, 1998a, Phys. Rev. Lett. **81**, 2498.
Kostic, P., Y. Okada, N. C. Collins, Z. Schlesinger, J. W. Reiner, L. Klein, T. A. Kapitulnik, T. H. Geballe, and M. R. Beasley, 1998b, Phys. Rev. Lett. **81**, 2498.
Kumigashira, H., M. Minohara, M. Takizawa, A. Fujimori, D. Toyota, I. Ohkubo, M. Oshima, M. Lippmaa, and M. Kawasaki, 2008, Appl. Phys. Lett. **92**, 122105.
Laad, M. S., I. Bradaric, and F. V. Kusmartsev, 2008, Phys. Rev. Lett. **100**, 096402.
Laad, M. S., and E. Muller-Hartmann, 2001, Phys. Rev. Lett. **87**, 246402.
Langner, M. C., C. L. S. Kantner, Y. H. Chu, L. M. Martin, P. Yu, J. Seidel, R. Ramesh, and J. Orenstein, 2009, Phys. Rev. Lett. **102**, 177601.
Lee, B. W., C. U. Jung, M. Kawasaki, and Y. Tokura, 2008, J. Appl. Phys. **104**, 103909.
Lee, H. N., H. M. Christen, M. F. Chisholm, C. M. Rouleau, and D. H. Lowndes, 2004, Appl. Phys. Lett. **84**, 4107.
Lee, J. S., Y. S. Lee, T. W. Noh, K. Char, J. Park, S.-J. Oh, J.-H. Park, C. B. Eom, T. Takeda, and R. Kanno, 2001, Phys. Rev. B **64**, 245107.
Lee, Y. S., J. S. Lee, T. W. Noh, D. Y. Byun, K. S. Yoo, K. Yamaura, and E. Takayama-Muromachi, 2003, Phys. Rev. B **67**, 113101.
Lee, Y. S., J. J. Yu, J. S. Lee, T. W. Noh, T. H. Gimm, H. Y. Choi, and C. B. Eom, 2002, Phys. Rev. B **66**, 041104.
Leitus, G. M., S. Reich, and F. Frolow, 1999, J. Magn. Magn. Mater. **206**, 27.
Li, J. L., Y. R. Li, Y. Zhang, X. W. Deng, F. Yang, and W. D. Fei, 2005, J. Cryst. Growth **274**, 612.
Li, Y. R., J. L. Li, Y. Zhang, X. W. Deng, F. Yang, and W. D. Fei, 2005, Mater. Sci. Forum **475–479**, 4255.
Liebsch, A., 2003, Eur. Phys. J. B **32**, 477.
Lifshitz, E. M., L. D. Landau, and L. P. Pitaevskii, 1984, *Electrodynamics of Continuous Media* (Elsevier Butterworth-Heinemann, Oxford).
Luke, G. M., *et al.*, 1998, Nature (London) **394**, 558.
Luttinger, J. M., 1958, Phys. Rev. **112**, 739.
Mackenzie, A. P., and Y. Maeno, 2003, Rev. Mod. Phys. **75**, 657.
Mackenzie, A. P., J. W. Reiner, A. W. Tyler, L. M. Galvin, S. R. Julian, M. R. Beasley, T. H. Geballe, and A. Kapitulnik, 1998, Phys. Rev. B **58**, R13 318.
Mahadevan, P., F. Aryasetiawan, A. Janotti, and T. Sasaki, 2009, Phys. Rev. B **80**, 035106.
Maiti, K., and R. Singh, 2005, Phys. Rev. B **71**, 161102.
Maiti, K., R. S. Singh, and V. R. R. Medicherla, 2007a, Phys. Rev. B **76**, 165128.
Maiti, K., R. S. Singh, and V. R. R. Medicherla, 2007b, Europhys. Lett. **78**, 17 002.
Maksym, P. A., 1988, Semicond. Sci. Technol. **3**, 594.
Maksymovych, P., S. Jesse, P. Yu, R. Ramesh, A. P. Baddorf, and S. V. Kalinin, 2009, Science **324**, 1421.
Manica, J., M. Abbate, J. A. Guevara, and S. L. Cuffini, 2004, Physica B (Amsterdam) **354**, 39.
Maria, J. P., H. L. McKinstry, and S. Trolier-McKinstry, 2000, Appl. Phys. Lett. **76**, 3382.
Marshall, A. F., L. Klein, J. S. Dodge, C. H. Ahn, J. W. Reiner, L. Mieville, L. Antagonazza, A. Kapitulnik, T. H. Geballe, and M. R. Beasley, 1999, J. Appl. Phys. **85**, 4131.
Mathieu, R., A. Asamitsu, H. Yamada, K. S. Takahashi, M. Kawasaki, Z. Fang, N. Nagaosa, and Y. Tokura, 2004, Phys. Rev. Lett. **93**, 016602.
Mazin, I. I., and D. J. Singh, 1997a, Phys. Rev. B **56**, 2556.
Mazin, I. I., and D. J. Singh, 1997b, Phys. Rev. B **56**, 2556.
Mieville, L., T. H. Geballe, L. Antognazza, and K. Char, 1997, Appl. Phys. Lett. **70**, 126.
Mieville, L., J. McGuirk, T. H. Geballe, L. Antognazza, and K. Char, 1996, Czech. J. Phys. **46**, 2105.
Mieville, L., D. Worledge, T. H. Geballe, R. Contreras, and K. Char, 1998, Appl. Phys. Lett. **73**, 1736.
Mishchenko, A. S., 2010, Adv. Condens. Matter Phys. **2010**, 1.
Mishchenko, A. S., and N. Nagaosa, 2004, Phys. Rev. Lett. **93**, 036402.
Mishchenko, A. S., N. Nagaosa, Z. X. Shen, G. D. Filippis, V. Cataudella, T. P. Devereaux, C. Bernhard, K. W. Kim, and J. Zaanen, 2008, Phys. Rev. Lett. **100**, 166401.
Mlynarczyk, M., K. Szot, A. Petraru, U. Poppe, U. Breuer, R. Waser, and K. Tomala, 2007, J. Appl. Phys. **101**, 023701.
Moriya, T., 1987, in *Metallic Magnetism*, edited by H. Capellmann, Topics in Current Physics Vol. 42 (Springer-Verlag, Berlin), p. 15.
Nadgorny, B., M. S. Osofsky, D. J. Singh, G. T. Woods, R. J. Soulen, M. K. Lee, S. D. Bu, and C. B. Eom, 2003, Appl. Phys. Lett. **82**, 427.
Nagarajan, V., *et al.*, 2006, J. Appl. Phys. **100**, 051609.
Nakahara, M., S. Tsunekawa, K. Watanabe, T. Arai, T. Yunogami, and K. Kuroki, 2001, J. Vac. Sci. Technol. B **19**, 2133.
Ogasawara, T., K. Ohgushi, Y. Tomioka, K. S. Takahashi, H. Okamoto, M. Kawasaki, and Y. Tokura, 2005, Phys. Rev. Lett. **94**, 087202.
Oh, S. H., and C. G. Park, 2000, J. Korean Phys. Soc. **37**, 961.
Oh, S. H., and C. G. Park, 2003, Philos. Mag. **83**, 1307.
Ohara, R., T. Schimizu, K. Sano, M. Yoshiki, and T. Kawakubo, 2001, Jpn. J. Appl. Phys. **40**, 1384.
Okamoto, J., T. Mizokawa, A. Fujimori, I. Hase, M. Nohara, H. Takagi, Y. Takeda, and M. Takano, 1999, Phys. Rev. B **60**, 2281.
Okuda, N., K. Saito, and H. Funakubo, 2000, Jpn. J. Appl. Phys. **39**, 572.
Pabst, G. W., L. W. Martin, Y.-H. Chu, and R. Ramesh, 2007, Appl. Phys. Lett. **90**, 072902.
Palai, R., H. Huhtinen, J. F. Scott, and R. S. Katiyar, 2009, Phys. Rev. B **79**, 104413.
Park, J., S. J. Oh, J. H. Park, D. M. Kim, and C. B. Eom, 2004, Phys. Rev. B **69**, 085108.
Park, J. H., S. K. Kwon, and B. I. Min, 2002, Phys. Rev. B **65**, 174401.
Pi, L., S. Zhang, S. Tan, and Y. Zhang, 2006a, Appl. Phys. Lett. **89**, 039902.
Pi, L., S. X. Zhang, S. Tan, and Y. H. Zhang, 2006b, Appl. Phys. Lett. **88**, 102502.
Prins, M. W. J., K. O. GrosseHolz, G. Muller, J. F. M. Cillessen, J. B. Giesbers, R. P. Weening, and R. M. Wolf, 1996, Appl. Phys. Lett. **68**, 3650.
Puchkov, A. V., M. C. Schabel, D. N. Basov, T. Startseva, G. Cao, T. Timusk, and Z.-X. Shen, 1998, Phys. Rev. Lett. **81**, 2747.
Ramesh, R., W. K. Chan, B. Wilkens, H. Gilchrist, T. Sands, J. M. Tarascon, V. G. Keramidas, D. K. Fork, J. Lee, and A. Safari, 1992, Appl. Phys. Lett. **61**, 1537.
Ramesh, R., A. Inam, W. K. Chan, B. Wilkens, K. Myers, K. Remschnig, D. L. Hart, and J. M. Tarascon, 1991, Science **252**, 944.
Rancourt, D. G., and M. Z. Dang, 1996, Phys. Rev. B **54**, 12 225.
Randall, J. J., and R. Ward, 1959, J. Am. Chem. Soc. **81**, 2629.

Rao, F. Y., M. Y. Kim, A. J. Freeman, S. P. Tang, and M. Anthony, 1997, Phys. Rev. B **55**, 13953.
Rao, M. V. R., V. G. Sathe, D. Sornadurai, B. Panigrahi, and T. Shripathi, 2001, J. Phys. Chem. Solids **62**, 797.
Rao, R. A., Q. Gan, C. B. Eom, R. J. Cava, Y. Suzuki, J. J. Krajewski, S. C. Gausepohl, and M. Lee, 1997, Appl. Phys. Lett. **70**, 3035.
Rao, R. A., D. B. Kacedon, and C. B. Eom, 1998, J. Appl. Phys. **83**, 6995.
Ratsch, C., M. D. Nelson, and A. Zangwill, 1994, Phys. Rev. B **50**, 14 489.
Ratsch, C., and A. Zangwill, 1993, Appl. Phys. Lett. **63**, 2348.
Raychaudhuri, P., A. P. Mackenzie, J. W. Reiner, and M. R. Beasley, 2003, Phys. Rev. B **67**, 020411.
Rijnders, G., D. H. A. Blank, J. Choi, and C. B. Eom, 2004, Appl. Phys. Lett. **84**, 505.
Rijnders, G. J. H. M., G. Koster, D. H. A. Blank, and H. Rogalla, 1997, Appl. Phys. Lett. **70**, 1888.
Rondinelli, J. M., N. M. Caffrey, S. Sanvito, and N. A. Spaldin, 2008, Phys. Rev. B **78**, 155107.
Rondinelli, J. M., M. Stengel, and N. A. Spaldin, 2008, Nature Nanotech. **3**, 46.
Rosch, O., O. Gunnarsson, X. J. Zhou, T. Yoshida, T. Sasagawa, A. Fujimori, Z. Hussain, Z. X. Shen, and S. Uchida, 2005, Phys. Rev. Lett. **95**, 227002.
Roussev, R., and A. J. Millis, 2000, Phys. Rev. Lett. **84**, 2279.
Ruediger, U., J. Yu, S. Zhang, A. D. Kent, and S. S. P. Parkin, 1998, Phys. Rev. Lett. **80**, 5639.
Sachdev, S., 1999, *Quantum Phase Transitions* (Cambridge University Press, Cambridge).
Sakai, J., N. Ito, S.-I. Ito, K. Takahashi, and H. Funakubo, 2006, Appl. Phys. Lett. **89**, 242115.
Sanchez, F., M. V. Garcia-Cuenca, C. Ferrater, M. Varela, G. Herranz, B. Martinez, and J. Fontcuberta, 2003, Appl. Phys. Lett. **83**, 902.
Sanchez, F., G. Herranz, C. Ferrater, M. V. Garcia-Cuenca, M. Varela, and J. Fontcuberta, 2006, Thin Solid Films **495**, 159.
Sanchez, F., G. Herranz, J. Fontcuberta, M. V. Garcia-Cuenca, C. Ferrater, and M. Varela, 2006, Phys. Rev. B **73**, 073401.
Sanchez, F., G. Herranz, I. C. Infante, C. Ferrater, M. V. Garcia-Cuenca, M. Varela, and J. Fontcuberta, 2006, Prog. Solid State Chem. **34**, 213.
Sanchez, F., G. Herranz, I. C. Infante, J. Fontcuberta, M. V. Garcia-Cuenca, C. Ferrater, and M. Varela, 2004, Appl. Phys. Lett. **85**, 1981.
Sanchez, F., U. Luders, G. Herranz, I. C. Infante, J. Fontcuberta, M. V. Garcia-Cuenca, C. Ferrater, and M. Varela, 2005, Nanotechnology **16**, S190.
Santi, G., and T. Jarlborg, 1997, J. Phys. Condens. Matter **9**, 9563.
Schmising, C., M. Bargheer, M. Kiel, N. Zhavoronkov, M. Woerner, T. Elsaesser, I. Vrejoiu, D. Hesse, and M. Alexe, 2007a, Phys. Rev. Lett. **98**, 257601.
Schmising, C. v. K., M. Bargheer, M. Kiel, N. Zhavoronkov, M. Woerner, T. Elsaesser, I. Vrejoiu, D. Hesse, and M. Alexe, 2006, Phys. Rev. B **73**, 212202.
Schmising, C. V. K., M. Bargheer, M. Kiel, N. Zhavoronkov, M. Woerner, T. Elsaesser, I. Vrejoiu, D. Hesse, and M. Alexe, 2007b, Appl. Phys. B **88**, 1.
Schmising, C. V. K., M. Bargheer, M. Kiel, N. Zhavoronkov, M. Woerner, T. Elsaesser, I. Vrejoiu, D. Hesse, and M. Alexe, 2007c, J. Phys. Conf. Ser. **92**, 012177.
Schmising, C. V. K., *et al.*, 2008, Phys. Rev. B **78**, 060404.
Schultz, M., S. Levy, J. Reiner, and L. Klein, 2009, Phys. Rev. B **79**, 125444.
Scott, J. F., and C. A. Paz de Araujo, 1989, Science **246**, 1400.
Shacklet, L. W., 1974, Phys. Rev. B **9**, 3789.
Shen, D. W., C. M. Brooks, D. E. Shai, J. W. Harter, E. J. Monkman, D. G. Schlom, and K. M. Shen, 2010 (unpublished).
Shimizu, T., and A. Kawakubo, 2001, Jpn. J. Appl. Phys. **40**, L117.
Shin, J., A. Y. Borisevich, V. Meunier, J. Zhou, E. W. Plummer, S. V. Kalinin, and A. P. Baddorf, 2010, ACS Nano **4**, 4190.
Shin, J., S. V. Kalinin, H. N. Lee, H. M. Christen, R. G. Moore, E. W. Plummer, and A. P. Baddorf, 2004, J. Mater. Res. **19**, 3447.
Shin, J., S. V. Kalinin, H. N. Lee, H. M. Christen, R. G. Moore, E. W. Plummer, and A. P. Baddorf, 2005, Surf. Sci. **581**, 118.
Shindou, R., and N. Nagaosa, 2001, Phys. Rev. Lett. **87**, 116801.
Shperber, Y., I. Genish, J. W. Reiner, and L. Klein, 2009, J. Appl. Phys. **105**, 07B106.
Siemons, W., G. Koster, A. Vailionis, H. Yamamoto, D. H. A. Blank, and M. R. Beasley, 2007, Phys. Rev. B **76**, 075126.
Simons, D. S., and M. B. Salamon, 1974, Phys. Rev. B **10**, 4680.
Singh, D. J., 1996a, J. Appl. Phys. **79**, 4818.
Singh, D. J., 1996b, J. Appl. Phys. **79**, 4818.
Singh, R. S., and K. Maiti, 2007, Phys. Rev. B **76**, 085102.
Singh, R. S., V. R. R. Medicherla, and K. Maiti, 2008, Physica B (Amsterdam) **403**, 1398.
Smit, J., 1958, Physica (Utrecht) **24**, 39.
Snyder, G. J., 1997, "Magnetism and Electron Transport in Magnetoresistive Lanthanum Calcium Manganite", Ph.D. thesis, Stanford University.
Solovyev, I. V., 1998, J. Magn. Magn. Mater. **177–181**, 811.
Stengel, M., D. Vanderbilt, and N. A. Spaldin, 2009, Nature Mater. **8**, 392.
Stoner, E. C., 1938, Proc. R. Soc. Lond. A **165**, 372.
Taguchi, Y., Y. Oohara, H. Yoshizawa, N. Nagaosa, and Y. Tokura, 2001, Science **291**, 2573.
Takahashi, K., T. Oikawa, K. Saito, S. Kaneko, H. Fujisawa, M. Shimizu, and H. Funakubo, 2002, Jpn. J. Appl. Phys. **41**, 5376.
Takahashi, K., M. Suzuki, T. Kojima, T. Watanabe, Y. Sakashita, K. Kato, O. Sakata, K. Sumitani, and H. Funakubo, 2006, Appl. Phys. Lett. **89**, 082901.
Takahashi, K. S., A. Sawa, Y. Ishii, H. Akoh, M. Kawasaki, and Y. Tokura, 2003, Phys. Rev. B **67**, 094413.
Takizawa, M., *et al.*, 2005, Phys. Rev. B **72**, 060404.
Taniguchi, S., M. Ogawara, N. Fukuoka, S. Mizusaki, Y. Nagata, Y. Noro, and H. Samata, 2009, J. Magn. Magn. Mater. **321**, 3335.
Tatara, G., H. Kohno, and J. Shibata, 2008, J. Phys. Soc. Jpn. **77**, 031003.
Terai, K., T. Ohnishi, M. Lippmaa, H. Koinuma, and M. Kawasaki, 2004, Jpn. J. Appl. Phys. **43**, L227.
Tian, W., J. H. Haeni, D. G. Schlom, E. Hutchinson, B. L. Sheu, M. M. Rosario, P. Schiffer, Y. Liu, M. A. Zurbuchen, and X. Q. Pan, 2007, Appl. Phys. Lett. **90**, 022507.
Timm, C., M. E. Raikh, and F. von Oppen, 2005, Phys. Rev. Lett. **94**, 036602.
Toyota, D., I. Ohkubo, H. Kumigashira, M. Oshima, T. Ohnishi, M. Lippmaa, M. Kawasaki, and H. Koinuma, 2006, J. Appl. Phys. **99**, 08N505.
Toyota, D., *et al.*, 2005, Appl. Phys. Lett. **87**, 162508.
Tringides, M. C., M. Jalochowski, and E. Bauer, 2007, Phys. Today **60**, 50.
Ueda, K., H. Saeki, H. Tabata, and T. Kawai, 2000, Solid State Commun. **116**, 221.
Uozu, Y., T. Nakajima, M. Nakamura, Y. Ogimoto, M. Izumi, and K. Miyano, 2004, Appl. Phys. Lett. **85**, 2875.

Vailionis, A., H. Boschker, W. Siemons, E. P. Houwman, D. H. A. Blank, G. Rijnders, and G. Koster, 2011, Phys. Rev. B **83**, 064101.
Vailionis, A., W. Siemons, and G. Koster, 2007, Appl. Phys. Lett. **91**, 071907.
Vailionis, A., W. Siemons, and G. Koster, 2008, Appl. Phys. Lett. **93**, 051909.
van der Marel, D., 1999, Phys. Rev. B **60**, R765.
van der Marel, D., H. J. A. Molegraaf, J. Zaanen, Z. Nussinov, F. Carbone, A. Damascelli, H. Eisaki, M. Greven, P. H. Kes, and M. Li, 2003, Nature (London) **425**, 271.
Vasco, E., R. Dittmann, S. Karthauser, and R. Waser, 2003, Appl. Phys. Lett. **82**, 2497.
Vasco, E., R. Dittmann, S. Karthauser, and R. Waser, 2004, Appl. Phys. A **79**, 1461.
Vasco, E., S. Karthauser, R. Dittmann, J. Q. He, C. L. Jia, K. Szot, and R. Waser, 2005, Adv. Mater. **17**, 281.
Vidya, R., P. Ravindran, A. Kjekshus, H. Flellvag, and B. C. Hauback, 2004, J. Solid State Chem. **177**, 146.
Volkensh, N. V., V. P. Dyakina, and V. E. Startsev, 1973, Phys. Status Solidi B **57**, 9.
Wang, G.-T., M.-P. Zhang, Z.-X. Yang, and Z. Fang, 2009, J. Phys. Condens. Matter **21**, 265602.
Wang, J., H. Zheng, Z. Ma, S. Prasertchoung, M. Wuttig, R. Droopad, J. Yu, K. Eisenbeiser, and R. Ramesh, 2004, Appl. Phys. Lett. **85**, 2574.
Werner, P., E. Gull, M. Troyer, and A. J. Millis, 2008, Phys. Rev. Lett. **101**, 166405.
Woerner, M., C. V. K. Schmising, M. Bargheer, N. Zhavoronkov, I. Vrejoiu, D. Hesse, M. Alexe, and T. Elsaesser, 2009, Appl. Phys. A **96**, 83.
Worledge, D. C., and T. H. Geballe, 2000, Phys. Rev. Lett. **85**, 5182.
Wu, X. D., S. R. Foltyn, R. C. Dye, Y. Coulter, and R. E. Muenchhausen, 1993, Appl. Phys. Lett. **62**, 2434.
Xia, J., P. T. Beyersdorf, M. M. Fejer, and A. Kapitulnik, 2006, Appl. Phys. Lett. **89**, 062508.
Xia, J., Y. Maeno, P. T. Beyersdorf, M. M. Fejer, and A. Kapitulnik, 2006, Phys. Rev. Lett. **97**, 167002.
Xia, J., W. Siemons, G. Koster, M. R. Beasley, and A. Kapitulnik, 2009, Phys. Rev. B **79**, 140407.
Yang, S. Y., *et al.*, 2005, Appl. Phys. Lett. **87**, 102903.
Yao, Y. G., L. Kleinman, A. H. MacDonald, J. Sinova, T. Jungwirth, D. S. Wang, E. G. Wang, and Q. Niu, 2004, Phys. Rev. Lett. **92**, 037204.
Ye, J. W., Y. B. Kim, A. J. Millis, B. I. Shraiman, P. Majumdar, and Z. Tesanovic, 1999, Phys. Rev. Lett. **83**, 3737.
Yoo, Y. Z., O. Chmaissem, S. Kolesnik, B. Dabrowski, M. Maxwell, C. W. Kimball, L. McAnelly, M. Haji-Sheikh, and A. P. Genis, 2005, J. Appl. Phys. **97**, 103525.
Yoo, Y. Z., *et al.*, 2006, Appl. Phys. Lett. **89**, 124104.
Zayak, A. T., X. Huang, J. B. Neaton, and K. M. Rabe, 2006, Phys. Rev. B **74**, 094104.
Zayak, A. T., X. Huang, J. B. Neaton, and K. M. Rabe, 2008, Phys. Rev. B **77**, 214410.
Ziese, M., I. Vrejoiu, and D. Hesse, 2010, Phys. Rev. B **81**, 184418.
Zumsteg, F. C., and R. D. Parks, 1970, Phys. Rev. Lett. **24**, 520.